



THE ASTROPHYSICAL JOURNAL

SUPPLEMENT SERIES

THE ACS NEARBY GALAXY SURVEY TREASURY

Julianne J. Dalcanton¹, Benjamin F. Williams¹, Anil C. Seth^{2,18}, Andrew Dolphin³, Jon Holtzman⁴, Keith Rosema¹, Evan D. Skillman⁵, Andrew Cole⁶, Léo Girardi⁷, Stephanie M. Gogarten¹, Igor D. Karachentsev⁸, Knut Olsen⁹, Daniel Weisz⁵, Charlotte Christensen¹, Ken Freeman¹¹, Karoline Gilbert¹, Carme Gallart¹², Jason Harris¹³, Paul Hodge¹, Roelof S. de Jong¹⁰, Valentina Karachentseva¹⁴, Mario Mateo¹⁵, Peter B. Stetson¹⁶, Maritza Tavares¹⁷, Dennis Zaritsky¹³, Fabio Governato¹, and Thomas Quinn¹

Published 2009 June 19 • © 2009. The American Astronomical Society. All rights reserved.

[The Astrophysical Journal Supplement Series, Volume 183, Number 1](#)



Article PDF

4909 Total downloads

Cited by 266 articles

[Get permission to re-use this article](#)

Share this article



[+ Article information](#)

Author e-mails

jd@astro.washington.edu
ben@astro.washington.edu
krosema@astro.washington.edu
stephanie@astro.washington.edu
christensen@astro.washington.edu
fabio@astro.washington.edu
trq@astro.washington.edu
aseth@cfa.harvard.edu
adolphin@raytheon.com
holtz@nmsu.edu
dweisz@astro.umn.edu
skillman@astro.umn.edu
andrew.cole@utas.edu.au
leo.girardi@oapd.inaf.it
ikar@luna.sao.ru
kolsen@noao.edu
dejong@stsci.edu
kcf@mso.anu.edu.au
carme@iac.es
jharris@as.arizona.edu
dennis@fishingholes.as.arizona.edu
vkarach@observ.univ.kiev.ua
mmateo@umich.edu
Peter.Stetson@nrc-cnrc.gc.ca
martavbrown@yahoo.com

Author affiliations

¹ Department of Astronomy, Box 351580, University of Washington, Seattle, WA 98195, USA

² Harvard-Smithsonian Center for Astrophysics, 60 Garden Street, Cambridge, MA 02138, USA

³ Raytheon, 1151 E. Hermans Road, Tucson, AZ 85756, USA

⁴ Department of Astronomy, New Mexico State University, Box 30001, 1320 Frenger St., Las Cruces, NM 88003, USA

- ⁵ Department of Astronomy, University of Minnesota, 116 Church St. SE, Minneapolis, MN 55455, USA
- ⁶ School of Mathematics and Physics, University of Tasmania, Hobart, Tasmania, Australia
- ⁷ Osservatorio Astronomico di Padova - INAF, Vicolo dell'Osservatorio 5, I-35122 Padova, Italy
- ⁸ Special Astrophysical Observatory, Russian Academy of Sciences, Nizhnji Arkhyz, Karachai-Circassia Republic 369167, Russia
- ⁹ NOAO, National Optical Astronomy Observatory 950 N. Cherry Ave., Tucson, AZ 85719, USA
- ¹⁰ Space Telescope Science Institute, 3700 San Martin Dr., Baltimore, MD 21218, USA
- ¹¹ Mount Stromlo Observatory, Research School of Astronomy and Astrophysics, Mount Stromlo Observatory, The Australian National University, ACT 0200, Australia
- ¹² Instituto de Astrofísica de Canarias, Vía Láctea, s/n, 38200 La Laguna, Tenerife, Spain
- ¹³ Steward Observatory, University of Arizona, 933 North Cherry Avenue, Tucson, AZ 85721, USA
- ¹⁴ Astronomical Observatory of Kiev University, Observatorna 3, 254053, Kiev, Ukraine
- ¹⁵ Department of Astronomy, University of Michigan, 830 Denninson Building, Ann Arbor, MI 48109-1090, USA
- ¹⁶ Dominion Astrophysical Observatory, Herzberg Institute of Astrophysics, National Research Council, 5071 West Saanich Road, Victoria, BC V9E 2E7, Canada
- ¹⁷ Forest Ridge School of the Sacred Heart, 4800 139th Ave SE, Bellevue, WA 98006, USA
- ¹⁸ CfA Fellow.

Dates

Received 2008 August 12

Accepted 2009 May 4

Published 2009 June 19

Citation

Julianne J. Dalcanton *et al* 2009 *ApJS* **183** 67

 [Create citation alert](#)

DOI

<https://doi.org/10.1088/0067-0049/183/1/67>

Keywords

[catalogs](#); [galaxies: formation](#); [galaxies: stellar content](#); [surveys](#)

 [Journal RSS feed](#)

 [Sign up for new issue notifications](#)

Abstract

The ACS Nearby Galaxy Survey Treasury (ANGST) is a systematic survey to establish a legacy of uniform multi-color photometry of resolved stars for a volume-limited sample of nearby galaxies ($D < 4$ Mpc). The survey volume encompasses 69 galaxies in diverse environments, including close pairs, small and large groups, filaments, and truly isolated regions. The galaxies include a nearly complete range of morphological types spanning a factor of $\sim 10^4$ in luminosity and star formation rate. The survey data consist of images taken with the Advanced Camera for Surveys (ACS) on the *Hubble Space Telescope* (HST), supplemented with archival data and new Wide Field Planetary Camera 2 (WFPC2) imaging taken after the failure of ACS. Survey images include wide field tilings covering the




full radial extent of each galaxy, and single deep pointings in uncrowded regions of the most massive galaxies in the volume. The new wide field imaging in ANGST reaches median 50% completenesses of $m_{F475W} = 28.0$ mag, $m_{F606W} = 27.3$ mag, and $m_{F814W} = 27.3$ mag, several magnitudes below the tip of the red giant branch (TRGB). The deep fields reach magnitudes sufficient to fully resolve the structure in the red clump. The resulting photometric catalogs are publicly accessible and contain over 34 million photometric measurements of >14 million stars. In this paper we present the details of the sample selection, imaging, data reduction, and the resulting photometric catalogs, along with an analysis of the photometric uncertainties (systematic and random), for both ACS and WFPC2 imaging. We also present uniformly derived relative distances measured from the apparent magnitude of the TRGB.

Export citation and abstract

[BibT eX](#)

[RIS](#)

+ Related links

- [NASA ADS Record](#) 
- [NED Objects](#) 
- [Simbad Objects](#) 
- [About Related Links](#)

1. INTRODUCTION

The study of nearby galaxies has been revolutionized by the *Hubble Space Telescope* (*HST*). The high spatial resolutions of the Wide Field Planetary Camera 2 (WFPC2) and the Advanced Camera for Surveys (ACS) reveal individual stars and parsec-scale structures, permitting studies of stellar populations, star formation histories (SFHs), and

stellar clusters for galaxies out to several megaparsecs. However, despite the large number of *HST* projects on these topics, past observations have been piecemeal and lack a unifying, coherent observational strategy in spite of the considerable overlap in the core scientific goals of many of the projects. Within a single galaxy, or from galaxy to galaxy, the locations of the *HST* exposures have been chaotic (having been chosen independently and for different purposes), and the filters and depths of the exposures have been highly variable. While past observations have provided dramatic insights into the SFHs of individual systems, the resulting archive complicates any uniform comparative study of galaxies in the local universe and dramatically reduces the scientific legacy of this data set.

The ACS Nearby Galaxy Survey Treasury (ANGST) program aims to rectify this situation by creating a uniform, multi-color archive of observations of resolved stellar populations within a volume-limited sample of nearby galaxies. The survey provides complete and unbiased sampling of the local universe, thereby maximizing the legacy impact of the resulting data set, and enabling meaningful comparisons among galaxies in the sample and with cosmological simulations. Within this volume, ANGST adds more than a hundred orbits of new high-quality observations, and provides uniform reduction and photometry of both the new and archival observations. The resulting survey now offers superb targets for future multi-wavelength surveys, including the VLA-ANGST survey (Ott et al. [2008](#)) and the *Spitzer* Local Volume Legacy Survey (LVL; Kennicutt et al. [2007](#)), by allowing one to tie the multi-wavelength observations to the local SFH revealed by ANGST.

In this paper we describe the survey design of ANGST, including the sample selection (Section [2](#)), the observing strategy for new observations (tiling patterns, filter choices, exposure times, etc.) using

both ACS (Section [3](#)) and WFPC2 (Section [4](#)), and the archival data employed by the survey (Section [5](#)). We then present photometry for the survey galaxies for both ACS (Section [6](#)) and WFPC2 (Section [7](#)), tests of the photometric reliability (Section [8](#)), astrometry (Section [9](#)), and the resulting data products included in this data release (Section [10](#)). In Section [11](#) we plot color–magnitude diagrams (CMDs) for all of the ANGST galaxies, and in Section [12](#) we measure colors and magnitudes for the tip of the red giant branch (TRGB), from which accurate relative distances are derived.

2. THE SAMPLE

2.1. Sample Selection

We drew the initial ANGST sample from the Karachentsev et al. ([2004](#)) Catalog of Neighboring Galaxies (CNG), updated with revised distances provided by Karachentsev. We restricted the catalog to galaxies beyond the zero velocity surface of the Local Group (van den Bergh [2000](#)) due to the efficacy of ground-based observations within 2 Mpc and the large number of existing *HST* observations (e.g., Holtzman et al. [2006](#)). We further restricted the sample to $|b| > 20^\circ$ to avoid sample incompleteness at low Galactic latitudes.

The choice of a maximum distance for the sample required balancing our scientific goals against constructing an observationally efficient program. At large distances, a wider variety of galaxy environments can be sampled, at the expense of larger photometric errors due to increased crowding and longer exposure times. We adopted an initial outer radius cut of 3.5 Mpc , within which deep CMDs could be derived with only modest exposure times. However, the Local Volume contains mostly field galaxies until reaching the massive M81 group at $\sim 3.6\text{ Mpc}$ and the Cen A group at $\sim 3.7\text{ Mpc}$. Scientifically, the case for including at least one of these groups is strong. Without them, the

limited range of environments sampled by a $D \lesssim 3.5 \text{ Mpc}$ sphere would preclude studies of correlations between SFH, galaxy morphology, and local environment. Of the two groups, the M81 group was judged to be the preferred target due to its high galactic latitude, low foreground extinction, and highly complete membership information. Galaxies in the M81 group were drawn from Karachentsev et al. ([2002a](#)), but do not include the newest candidate members reported in Chiboucas et al. ([2009](#)). We also included a second high-density environment centered on the NGC 253 clump ($D \approx 3.9 \text{ Mpc}$) in the Sculptor filament (Karachentsev et al. [2003](#)), further increasing the range of environments probed. The extensions into the M81 group and NGC 253 clump of the Sculptor group also improves coverage of luminous galaxies that are poorly represented in the $D < 3.5 \text{ Mpc}$ volume.

The resulting sample of 69 galaxies is given in Table [1](#), along with the distances adopted during sample selection. Notable changes from the published version of the CNG include larger distances for UGC 8638, E059-01, and KKH60, which took them out of the sample, revised closer distances for NGC 4163 and DDO 183 which brought them into the sample, and elimination of HIJASS, which has no detectable stars. Distances for NGC 247, NGC 55, DDO 187, UGC 8833, HS117, and KKH37 were also revised according to new distances in Karachentsev ([2005](#)). Other data compiled in Table [1](#) include absolute total magnitudes in B , morphological T-types, angular diameters (D_{25} for large galaxies, $D_{26.5}$ for some dwarfs), and H i line widths (W_{50}); all these quantities are listed as originally compiled in the CNG, and details can be found in Karachentsev et al. ([2004](#)). We also include apparent total K -band magnitudes from the literature when available; these are included for completeness only, and no attempt has been made to bring these to a common aperture with the B -band magnitudes from the CNG. Table [1](#) also indicates the original *planned*

observational strategy for the sample galaxies; as we discuss below, not all observations were carried out as planned due to the failure of ACS.

Table 1. ANGST Sample Galaxies and Planned Observations

Galaxy	Alt. Names	Dist. (Mpc)	R.A. (J2000)	Decl. (J2000)	Diam. ($'$)	M_r
Antlia		1.3	10:04:04.0	-27:19:55	2.0	-9.5
SexA	DDO75	1.3	10:11:00.8	-04:41:34	5.5	-13.5
N3109	DDO236	1.3	10:03:07.2	-26:09:36	17.0	-15.5
SexB	U5373	1.4	10:00:00.1	05:19:56	5.1	-13.5
KKR25		1.9	16:13:47.6	54:22:16	1.1	-9.5
KK230	KKR3	1.9	14:07:10.7	35:03:37	0.6	-8.5
E410-005		1.9	00:15:31.4	-32:10:48	1.3	-11.5
E294-010		1.9	00:26:33.3	-41:51:20	1.1	-10.5
N55		2.1	00:15:08.5	-39:13:13	32.4	-17.5
I5152		2.1	22:02:41.9	-51:17:43	5.2	-15.5
GR8	U8091	2.1	12:58:40.4	14:13:03	1.1	-12.5
N300		2.1	00:54:53.5	-37:40:57	21.9	-17.5
UA438	E407-18	2.2	23:26:27.5	-32:23:26	1.5	-12.5
DDO187	U9128	2.3	14:15:56.5	23:03:19	1.7	-12.5
KKH98		2.5	23:45:34.0	38:43:04	1.1	-10.5
DDO125	U7577	2.5	12:27:41.8	43:29:38	4.3	-14.5
U18508	U7560	2.6	12:30:44.4	54:54:36	1.7	-10.5

Galaxy	Alt. Names	Dist. (Mpc)	R.A.	Decl.	Diam.	Δ
KKH86		2.6	13:54:33.6	04:14:05	0.7'	-10
DDO99	U6817	2.6	11:50:53.0	38:52:50	4.1	-13
DDO190	U9240	2.8	14:24:43.5	44:31:33	1.8	-14
DDO113	UA276	2.9	12:14:57.9	36:13:08	1.5	-15
N4214	U7278	2.9	12:15:38.9	36:19:39	8.5	-17
DDO181	U8651	3.0	13:39:53.8	40:44:21	2.3	-12
N3741	U6572	3.0	11:36:06.4	45:17:07	2.0	-13
N4163	U7199	3.0	12:12:08.9	36:10:10	1.9	-13
N404	U718	3.1	01:09:26.9	35:43:03	2.5	-16
UA292	CVnI-dwA	3.1	12:38:40.0	32:46:00	1.0	-15
U8833		3.1	13:54:48.7	35:50:15	0.9	-12
DDO183	U8760	3.2	13:50:51.1	38:01:16	2.2	-13
N2366	U3851	3.2	07:28:52.0	69:12:19	7.3	-15
DDO44	UA133	3.2	07:34:11.3	66:53:10	3.0	-15
E321-014		3.2	12:13:49.6	-38:13:53	1.4	-12
U4483		3.2	08:37:03.0	69:46:31	1.2	-12
N2403	U3918	3.3	07:36:54.4	65:35:58	21.9	-18
DDO6	UA15	3.3	00:49:49.3	-21:00:58	1.7	-12
KKH37		3.4	06:47:45.8	80:07:26	1.2	-15
HoII	U4305	3.4	08:19:05.9	70:42:51	7.9	-16
KDG2	E540-030, KK9	3.4	00:49:21.1	-18:04:28	1.2	-15

Galaxy	Alt. Names	Dist. (Mpc)	R.A. (J2000)	Decl. (J2000)	Diam. (')	RA
MGCG 20-131			12:15:46.7	52:23:15		-14
E540-032		3.4	00:50:24.6	-19:54:25	1.3	-15
FM1	F6D1	3.4	09:45:25.6	68:45:27	0.9	-16
KK77	F12D1	3.5	09:50:10.0	67:30:24	2.4	-15
KDG63	U5428,DDO71	3.5	10:05:07.3	66:33:18	1.7	-15
N4190	U7232	3.5	12:13:44.6	36:38:00	1.7	-14
M82	N3034,U5322	3.5	09:55:53.9	69:40:57	11.2	-18
KDG52	M81-Dwarf-A	3.5	08:23:56.0	71:01:46	1.3	-15
DDO53	U4459	3.5	08:34:06.5	66:10:45	1.6	-13
N2976	U5221	3.6	09:47:15.6	67:54:49	5.9	-16
KDG61		3.6	09:57:02.7	68:35:30	2.4	-12
M81	N3031,U5318	3.6	09:55:33.5	69:04:00	26.9	-20
N247	UA11	3.6	00:47:08.3	-20:45:36	15.4	-17
HoIX	U5336,DDO66,KDG62	3.7	09:57:32.4	69:02:35	2.5	-13
KDG64	U5442	3.7	10:07:01.9	67:49:39	1.9	-12
IKN		3.7	10:08:05.9	68:23:57	2.7	-10
KDG73		3.7	10:52:55.3	69:32:45	0.6	-10
DDO78		3.7	10:26:27.9	67:39:24	2.0	-12
F8D1		3.8	09:44:47.1	67:26:19	5.5	-12
BK5N		3.8	10:04:40.3	68:15:20	0.8	-10
N3077	U5398	3.8	10:03:21.0	68:44:02	5.4	-15

Galaxy	Alt. Names	Dist.	R.A.	Decl.	Diam.	M_B
HoI	U5139,DDO63	3.8 (Mpc)	09:40:28.2 (J2000)	71:11:11 (J2000)	3.6	-14
BK6N		3.8	10:34:31.9	66:00:42	1.1	-11
A0952+69		3.9	09:57:29.0	69:16:20	1.8	-15
KKH57		3.9	10:00:16.0	63:11:06	0.6	-10
N253	UA13	3.9	00:47:34.3	-25:17:32	26.7	-20
HS117		4.0	10:21:25.2	71:06:58	1.5	-11
DDO82	U5692	4.0	10:30:35.0	70:37:10	3.4	-14
BK3N		4.0	09:53:48.5	68:58:09	0.5	-9
I2574	U5666,DDO81	4.0	10:28:22.4	68:24:58	13.2	-17
Sc22	Sc-dE1	4.2	00:23:51.7	-24:42:18	0.9	-10

Notes. Distances, M_B , W_{50} , and T-type taken from CNG; values for m_K are total K magnitudes from either the 2MASS Large Galaxy Atlas (Jarrett et al. [2003](#)) or from Vaduvescu et al. ([2005](#)) for dwarfs; Group membership from Karachentsev ([2005](#)) or Tully et al. ([2006](#)); # of ANGST Pointings includes any planned deep fields; Deep column indicates planned observations that would reach high completeness in the red clump; note that not all planned observations were executed, due to ACS failure—actual observations are given in Table [2](#); 3 filter column indicates observations made in F475W+F606W+F814W, rather than default F475W+F606W for dwarfs; Archival lists Proposal ID of archival data to be used, with entries in parentheses indicating that archival data will be supplemented with new observations; H i detection for KKR25 in the CNG was not confirmed in later GMRT observations (Begum & Chengalur [2005](#)); (a) WFPC2 Archival data.

Download table as:

Table 2. ANGST Observations

Field Name	R.A. (J2000)	Decl. (J2000)	V3 PA (deg)	Aperture	Date Range	Instr.	Filter
NGC 3109- WIDE1	10 02 41.8	-26 08 58	95.001	WFALL-FIX	2007- 11-02	WFPC2	F606W F814W
NGC 3109- WIDE2	10 02 49.9	-26 09 07	95.001	WFALL-FIX	2007- 11-08	WFPC2	F606W F814W
NGC 3109- WIDE3	10 02 57.81	-26 09 16.4	95.001	WFALL-FIX	2007- 11-06	WFPC2	F606W F814W
NGC 3109- WIDE4	10 03 05.81	-26 09 25.6	95.001	WFALL-FIX	2007- 11-10	WFPC2	F606W F814W
NGC 3109- DEEP	10 02 34.1	-26 09 23	123.658	WFALL-FIX	2007- 12-20	WFPC2	F606W F814W
SEXB- DEEP	10 00 03.9	+05 19 29	112.614	WFALL-FIX	2007- 12-12	WFPC2	F606W F814W
NGC	00 14	-39 09	101.142	WFALL	2007-	WFPC2	F606W

Field Name	R.A. (J2000)	Decl. (J2000)	V3 PA (deg)	Aperture	Date Range	Instr.	Filter
							F814W
					2008- 07-06	WFPC2	F606W
							F814W
NGC 0055- WIDE2	00 14 20.0	-39 09 56	101.141	WFALL	2008- 07-04	WFPC2	F606W
							F814W
NGC 0055- WIDE3	00 14 28.9	-39 10 18	101.142	WFALL	2007- 08-07	WFPC2	F606W
							F814W
NGC 0055- WIDE4	00 14 37.2	-39 10 42	104.002	WFALL	2007- 08-09	WFPC2	F606W
							F814W
NGC 0055- WIDE5	00 15 10.4	-39 12 58	101.142	WFALL	2007- 08-06	WFPC2	F606W
							F814W
NGC 0055- DEEP	00 13 44.4	-39 07 43	58.335	WFALL-FIX	2007- 06-02	WFPC2	F606W
							F814W
IC5152- DEEP	22 03 12.0	-51 18 33	76.003	WFALL-FIX	2007- 06-19	WFPC2	F606W

Field Name	R.A. (J2000)	Decl. (J2000)	V3 PA (deg)	Aperture	Date 2007- Range 06-20	Instr.	Filter F814W
GR8	12 58 40.94	+14 13 00.6	112.560	WFC1-FIX	2007- 01-03	ACS	F475W F814W
NGC 0300- WIDE1	00 54 21.5	-37 37 58	209.925	WFCENTER	2006- 11-10	ACS	F475W F606W F814W
NGC 0300- WIDE2	00 54 34.8	-37 39 27	209.925	WFCENTER	2006- 11-08	ACS	F475W F606W F814W
NGC 0300- WIDE3	00 54 47.8	-37 40 53	209.925	WFCENTER	2006- 11-09	ACS	F475W F606W F814W
KKH98	23 45 34.19	+38 43 10.1	230.070	WFC1-FIX	2007- 01-02	ACS	F475W F814W
UGC8508	13 30 44.95	+54 54 37.1	122.276	WFC1-FIX	2006- 12-21	ACS	F475W F814W
DDO188	11 01	+11 01	150.511	WFC1-FIX	2006-	ACS	F475W

Field DDO44 Name	R.A. 07 34 (J2000) 12.48	Decl. +66 53 (J2000) 08.4	V3 PA 112.749 (deg)	Aperture WFC-FIX	Date 2006- Range 09-21	Instr. ACS	Filter F475W
							F814W
NGC 2403- DEEP	07 38 05.5	+65 30 16.0	69.995	WFALL-FIX	2007- 11-26	WFPC2	F606W
					2007- 12-01		F814W
DDO6	00 49 49.69	-21 01 00.5	121.489	WFC1-FIX	2006- 09-19	ACS	F475W
							F814W
KKH37	06 47 47.64	+80 07 29.7	58.707	WFC1-FIX	2006- 11-10	ACS	F475W
							F814W
NGC 2976- WIDE1	09 47 17.0	+67 53 58	52.756	WFCENTER	2006- 12-30	ACS	F475W
							F606W
							F814W
NGC 2976- DEEP	09 47 36.6	+67 51 25	51.353	WFCENTER	2006- 12-27	ACS	F475W
					2007- 01-10		F606W
							F814W
M81- DEEP	09 54 34.7	+69 16 50	89.814	WFCENTER	2006- 11-16	ACS	F475W

Field Name	R.A. (J2000)	Decl. (J2000)	V3 PA (deg)	Aperture	Date Range	Instr.	Filter
							F814W
NGC 0247-WIDE1	00 47 19.06	-20 52 12.2	167.978	WFCENTER	2006-09-22	ACS	F475W
							F606W
							F814W
NGC 0247-WIDE2	00 47 12.5	-20 49 14	167.979	WFCENTER	2006-09-20	ACS	F475W
							F606W
							F814W
NGC 0247-WIDE3	00 47 10.4	-20 46 09	167.979	WFCENTER	2006-09-21	ACS	F475W
							F606W
							F814W
KDG73	10 52 58.54	+69 32 52.1	71.609	WFC1-FIX	2007-01-01	ACS	F475W
							F814W
DDO78	10 26 29.17	+67 39 12.1	130.158	WFC1-FIX	2006-10-18	ACS	F475W
							F814W
NGC 3077-WIDE1	10 03 28.4	+68 43 53	153.086	WFCENTER	2006-09-21	ACS	F475W

Field Name	R.A. (J2000)	Decl. (J2000)	V3 PA (deg)	Aperture	Date Range	Instr.	Filter
A0952+69	09 57 36.08	+69 16 59.5	148.862	WFC1-FIX	2006- 09-22	ACS	F475W F814W
NGC 0253- WIDE1	00 48 19.59	-25 08 51.2	144.990	WFCENTER	2006- 09-19	ACS	F475W F606W F814W
NGC 0253- WIDE2	00 48 08.7	-25 10 48	139.995	WFCENTER	2006- 09-08	ACS	F475W F606W F814W
NGC 0253- WIDE3	00 47 57.9	-25 12 48	159.219	WFCENTER	2006- 09-15	ACS	F475W F606W F814W
NGC 0253- WIDE4	00 47 47.2	-25 14 46	140.893	WFCENTER	2006- 09-09	ACS	F475W F606W F814W
NGC 0253-	00 47 36.4	-25 16 46	139.995	WFCENTER	2006- 09-13	ACS	F475W

Field Name	R.A. (J2000)	Decl. (J2000)	V3 PA (deg)	Aperture	Date Range	Instr.	Filter
							F606W
							F814W
DDO82	10 30 37.80	+70 37 13.0	157.574	WFC-FIX	2006- 09-22	ACS	F475W
							F606W
							F814W
BK3N	09 53 47.81	+68 58 06.7	148.844	WFC1-FIX	2006- 09-20	ACS	F475W
							F814W

Notes. All data is from GO-10915, except NGC 55 and NGC 3109 wide fields, which are from DD-11307. Entries with reduced precision in the listings for R.A. and decl. indicate a representative center for dithered observations. Multiple dates for a given field indicate the start times for the earliest and the latest observations of that field. Note that many fine guidance sensor problems occurred during observations for GO-10915, and that not all data in the archive under this PID is useable; only high quality observations are included in this table.

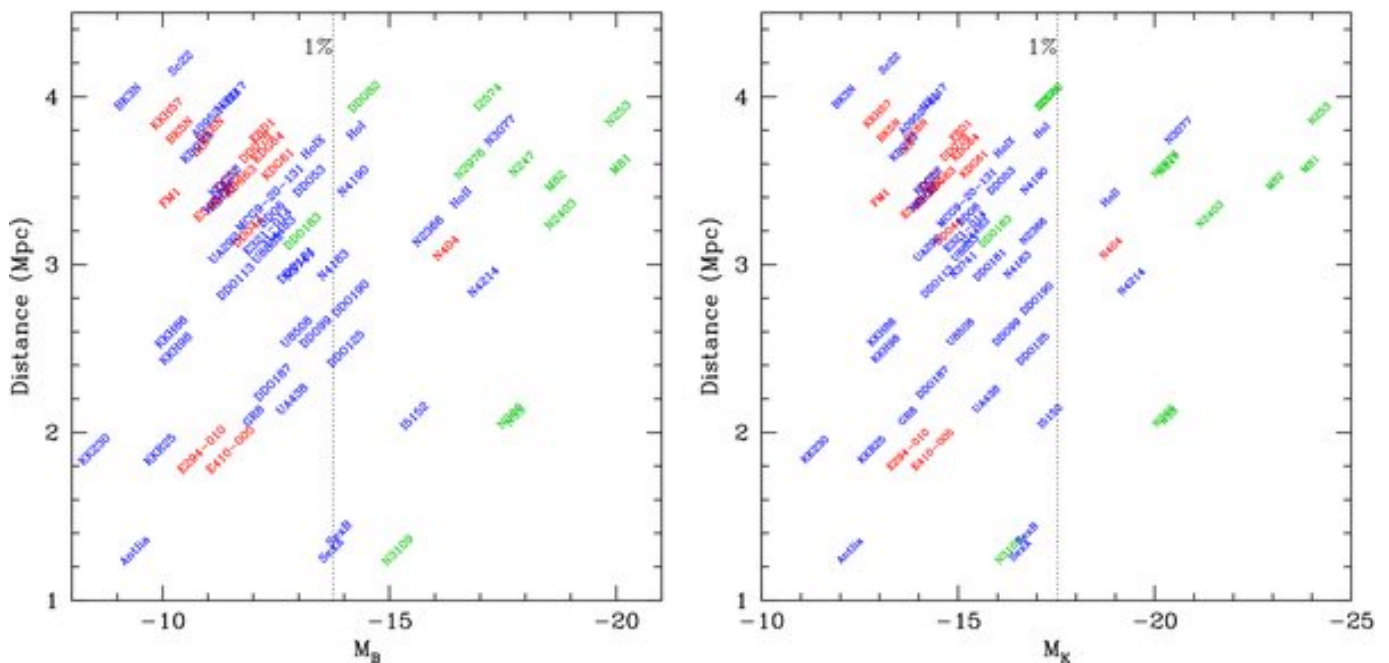
Download table as:

Typeset images:

2.2. Properties of the Final Sample

The volume-limited sample defined above contains a rich assortment of galaxies. The range of distances, luminosities (in B and K), and morphological types of the sample galaxies can be seen in Figure [1](#). Galaxy absolute magnitudes span from brighter than $M_B = -20$ (M81

and NGC 253, the dominant galaxies in the M81 group and the Sculptor filament), down to fainter than $M_B = -9$, comparable to the Carina dwarf spheroidal in the Local Group. K -band total magnitudes were adopted from Jarrett et al. ([2003](#)) or Vaduvescu et al. ([2005](#)) when available, or inferred from B -band magnitudes assuming $B - K \sim 2.86$, based on the estimates in Mannucci et al. ([2001](#)) for dwarf irregular spectral types.



🔍 Zoom In 🔍 Zoom Out

🔄 Reset image size

Figure 1. Distribution of the ANGST sample galaxies in distance and absolute magnitude (left: B band; right: K band). Points are color-coded by morphological type (red: $T=0$; green: $1 \leq T \leq 9$, blue: $T=10$). The majority of early type galaxies are dwarf ellipticals in the dense M81 group. The galaxies to the left of the vertical line contain less than 1% of the integrated B - or K -band luminosity in the survey volume. K -band absolute magnitudes have been estimated for some of the low-luminosity galaxies Mannucci et al. (2001).

Download figure:

🖼️ Standard image

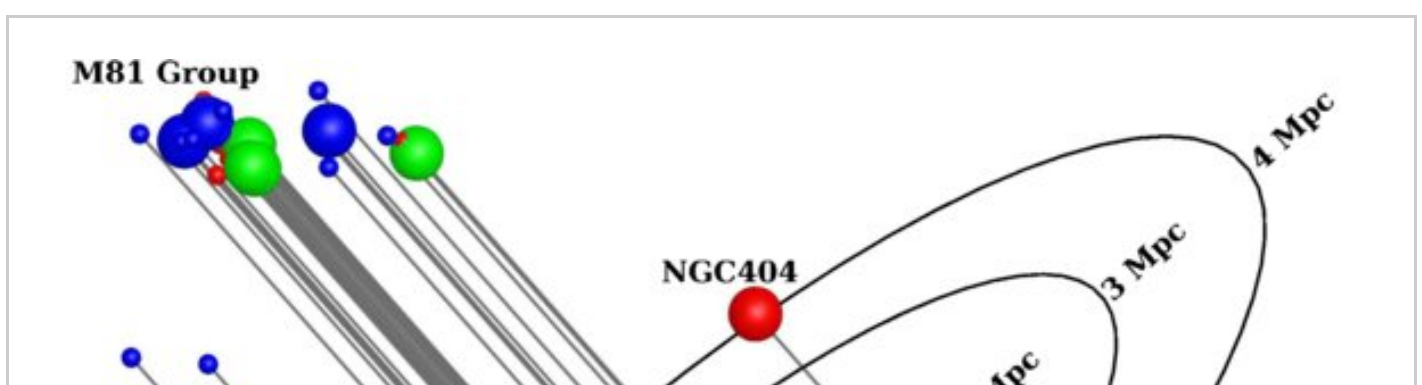
🖼️ High-resolution image

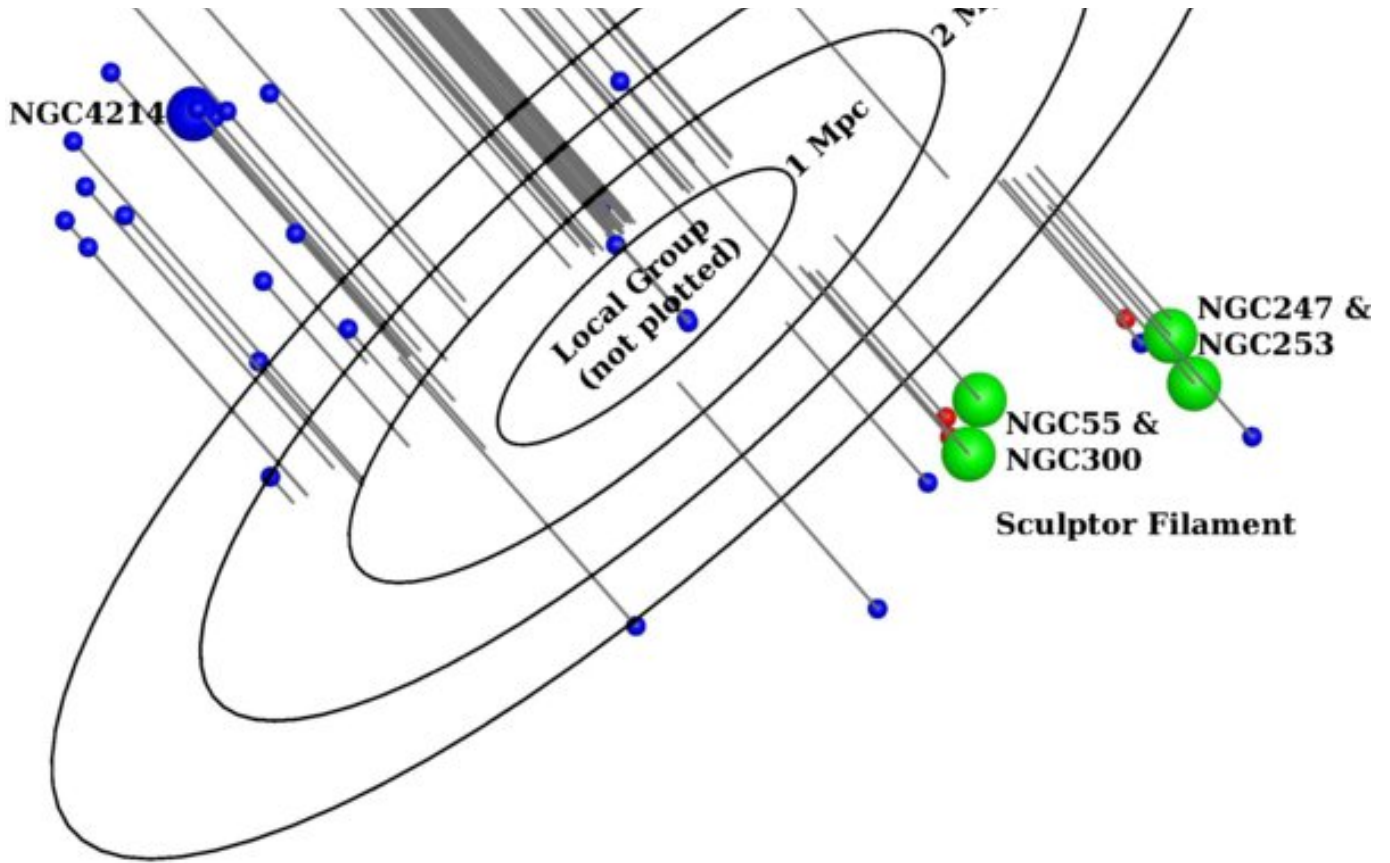
📄 Export PowerPoint slide

As for any volume-limited sample, the distribution of luminosities is strongly weighted toward dwarf systems. Roughly 90% of the galaxies in the ANGST volume are fainter than the Large Magellanic Cloud,

and 80% are fainter than the Small Magellanic Cloud. Integrating the luminosities of the galaxies, 99% of the B -band luminosity is contained in galaxies brighter than $M_B = -13.7$ (33% by number). In the K band, which presumably is a better tracer of the stellar mass, 99% of the luminosity is contained within only 17% of the galaxies ($M_K < -17.5$). The large number of low-luminosity systems is also reflected in the distribution of morphological types. Only 17% of the galaxies have morphological types characteristic of spirals ($1 \leq T \leq 9$), while 58% are classified as dwarf irregulars and 25% as dwarf ellipticals. In spite of the large population of dwarf ellipticals, there are no massive early types in the sample. NGC 404 is classified as an S0, but has relatively low luminosity and an extended gas disk (del Río et al. [2004](#)). The earliest massive spiral in the sample is M81, with a morphological type of Sab.

The sample galaxies reside in diverse environments. There are at least four distinct groups with a range of richnesses—the dwarf dominated NGC 3109 group, two clumps in the Sculptor filament (one at NGC 55/NGC 300 and one at NGC 253/NGC 247), and the rich M81 group. Several of Tully et al. ([2006](#))'s "dwarf groups" are also included in the ANGST survey volume (14+12, 14+13 14+07, 14+08; the first two are the NGC 3109 and NGC 55/NGC 300 groups mentioned above). Group membership is also included in Table [1](#). Some of these groups can be seen in Figure [2](#), where we show the three-dimensional distribution of the survey galaxies, using updated distances from Section [12](#).¹⁹





🔍 Zoom In 🔍 Zoom Out

🔄 Reset image size

Figure 2. Three-dimensional space distribution of the ANGST sample galaxies. Galaxies are color-coded by morphological type (red: $T=0$; green: $1 < T < 9$, blue: $T=10$), as in Figure 1. Larger symbols indicate galaxies brighter than $M_B = -16.0$. The large clump of galaxies in the upper left is the rich M81 group. The two clumps under the plane along the right hand axis are the closer NGC 55/NGC 300 clump and the more distant NGC 247/NGC 253 subclump along the Sculptor filament. The bright galaxy at the center of the dwarf cloud on the left is NGC 4214, and the bright isolated early-type galaxy to the right is NGC 404. The circles are drawn at intervals of 1 Mpc , along the equatorial plane. Distances are taken from Table 5. Note that not all galaxies within 4 Mpc are plotted due to ANGST's $|b| > 20^\circ$ selection criteria.

Download figure:

 Standard image

 High-resolution image

3. ACS OBSERVING STRATEGY

When designing an observing strategy for the ANGST sample, we balanced the limited number of orbits (295, down from an initial request of 555) against the goal of simultaneously recovering the SFH of the volume and establishing a general purpose imaging archive. We aimed to maximize uniformity, depth, and versatility, while making efficient use of the allocated orbits and the data already in the archive.

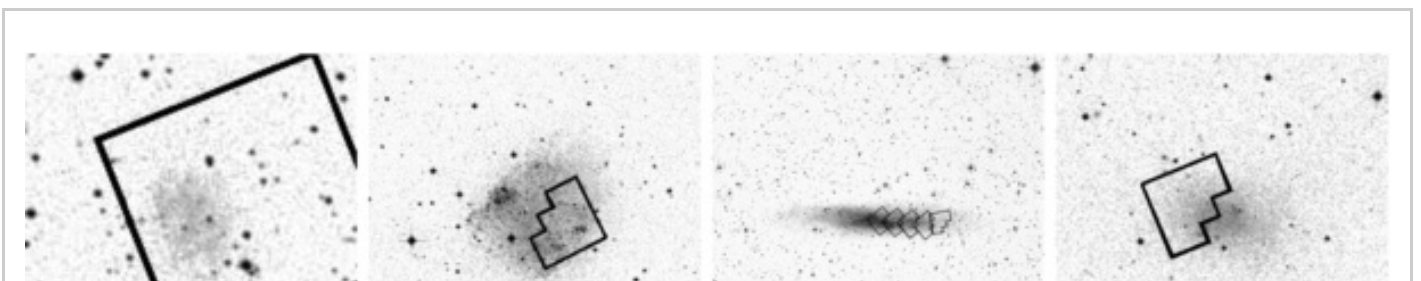
As part of this strategy, we chose to allocate a larger fraction of the orbits to the galaxies with the most stars, which contained either 99% of the stars or 99% of the recently formed stars. These galaxies fall to the right of the vertical lines in the right- and left-hand panels of Figure [1](#).

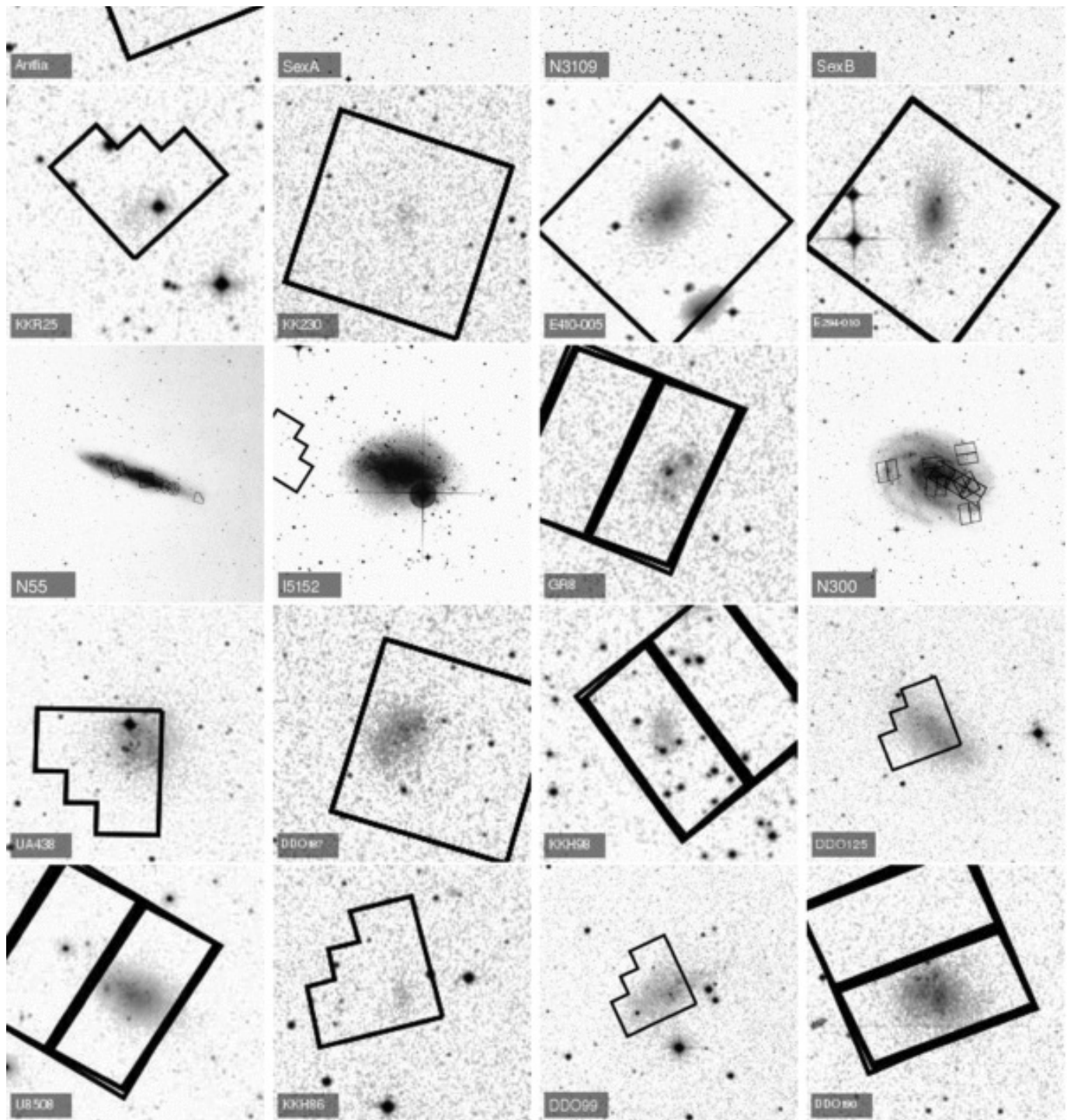
The full radial extent of all galaxies was imaged in at least two filters. For dwarfs, these wide field tiles could be acquired in a single pointing. Larger, angularly extended galaxies were each imaged with a radial strip of overlapping ACS tiles extending from the galaxy's center to its outskirts. In addition to the wide fields, deep fields with high completeness in the red clump were planned for the 12 galaxies that dominate the K -band luminosity of the ANGST volume; this depth provides strong constraints on the ancient SFH (e.g., Dolphin [2002](#)). Another 16 galaxies within $\sim 2.5 \times \text{Mpc}$ would reach a comparable depth from their wide field tilings alone. In addition to the two filters in the standard wide field tilings, the 23 galaxies that dominate the recent star formation density (as assessed in the B band) would be imaged in three filters to permit extinction corrections and multi-wavelength source identification. Finally, archival imaging of comparable depth to the new observations would be used when possible.

We now discuss the details of the wide-field tilings, the deep fields, the choice of filters, and the exposure times. In Section [4](#), we discuss how this strategy was modified after ACS failed during our program's execution.

3.1. Wide Field Tiling

The wide field tilings were designed for efficient multi-filter coverage of each galaxy's radial extent. Thanks to ACS's large field of view (FOV), dwarf galaxies could be imaged with a single pointing. For smaller dwarf galaxies, the galaxy center was aligned with the center of the WFC1 chip to avoid the chip gap's occluding the center of the galaxy. For the larger dwarf galaxies DDO 44 and DDO 82, the center was placed slightly above the chip gap. For galaxies whose radial extents were larger than could be imaged in a single pointing, we adopted a set of radial tiles extending from the center of the galaxy out to the position of the deep field, along the major axis in whichever direction required the smallest number of tiles. To allow flexible telescope scheduling, the tiles were allowed to be at any multiple of a 90° rotation from the major axis, with a $\pm 5^\circ$ leeway. Adjacent tiles were overlapped by 22" to allow complete coverage throughout the permitted range of telescope roll angles. All tiles were dithered to fill the chip gap and to remove cosmic rays and hot pixels. In the ANGST target naming scheme, tiles are numbered from the outermost tile inward. The resulting field locations are shown superimposed on images from the Digitized Sky Survey in Figures [3–6](#), for both the ANGST observations and the archival observations described below (Tables [2](#) and [3](#)).





🔍 [Zoom In](#) 🔍 [Zoom Out](#)

🔄 [Reset image size](#)

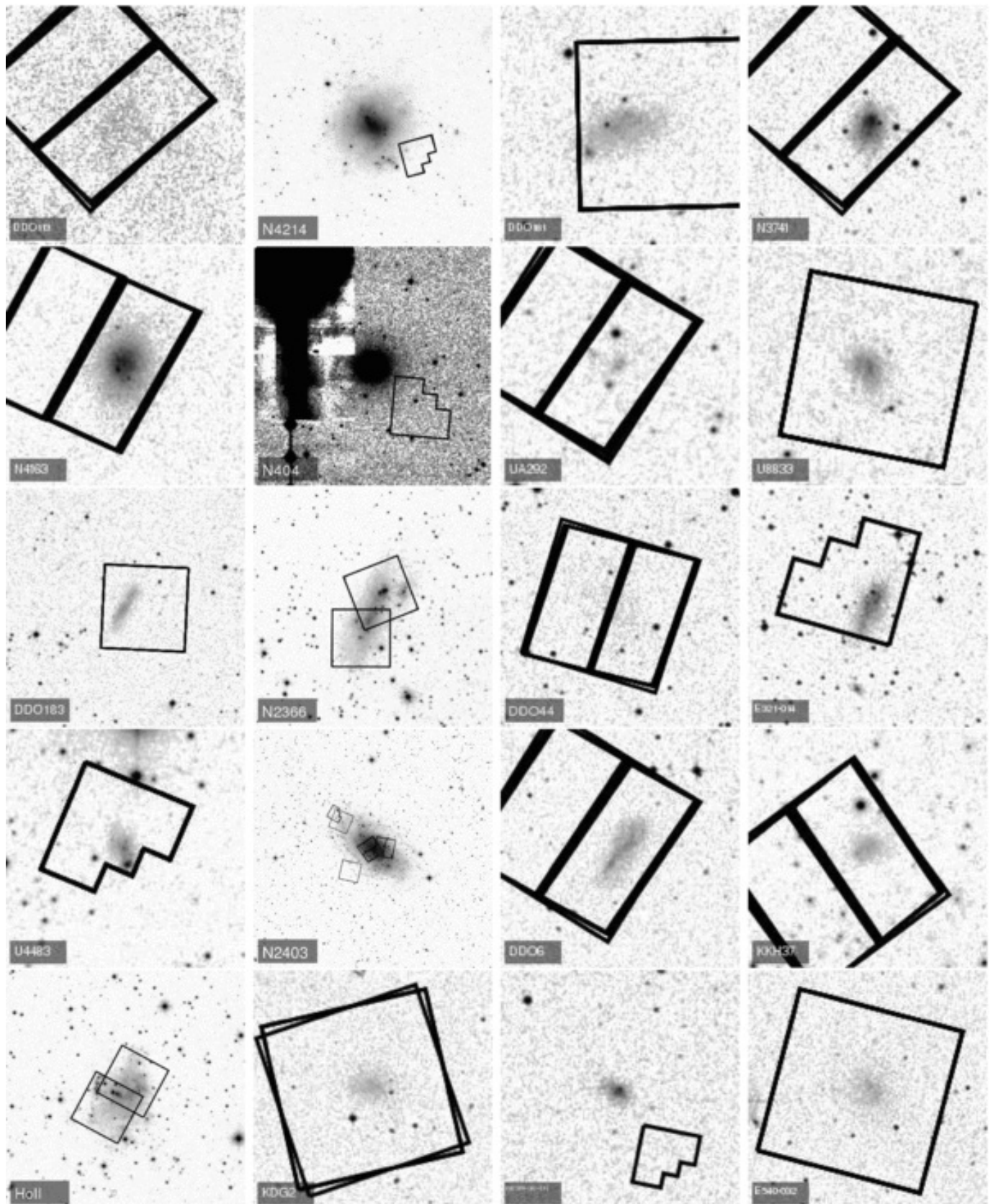
Figure 3. Field positions of images included in (Tables 2 and 3). Figures are ordered from the upper left to the bottom right. (a) Antlia; (b) SexA; (c) N3109; (d) SexB; (e) KKR25; (f) KK230; (g) E410-005; (h) E294-010; (i) N55; (j) I5152; (k) GR8; (l) N300; (m) UA438; (n) DDO187; (o) KKH98; (p) DDO125; (q) U8508; (r) KKH86; (s) DDO99; (t) DDO190.

Download figure:

 Standard image

 High-resolution image

 Export PowerPoint slide



 Zoom In  Zoom Out

 Reset image size

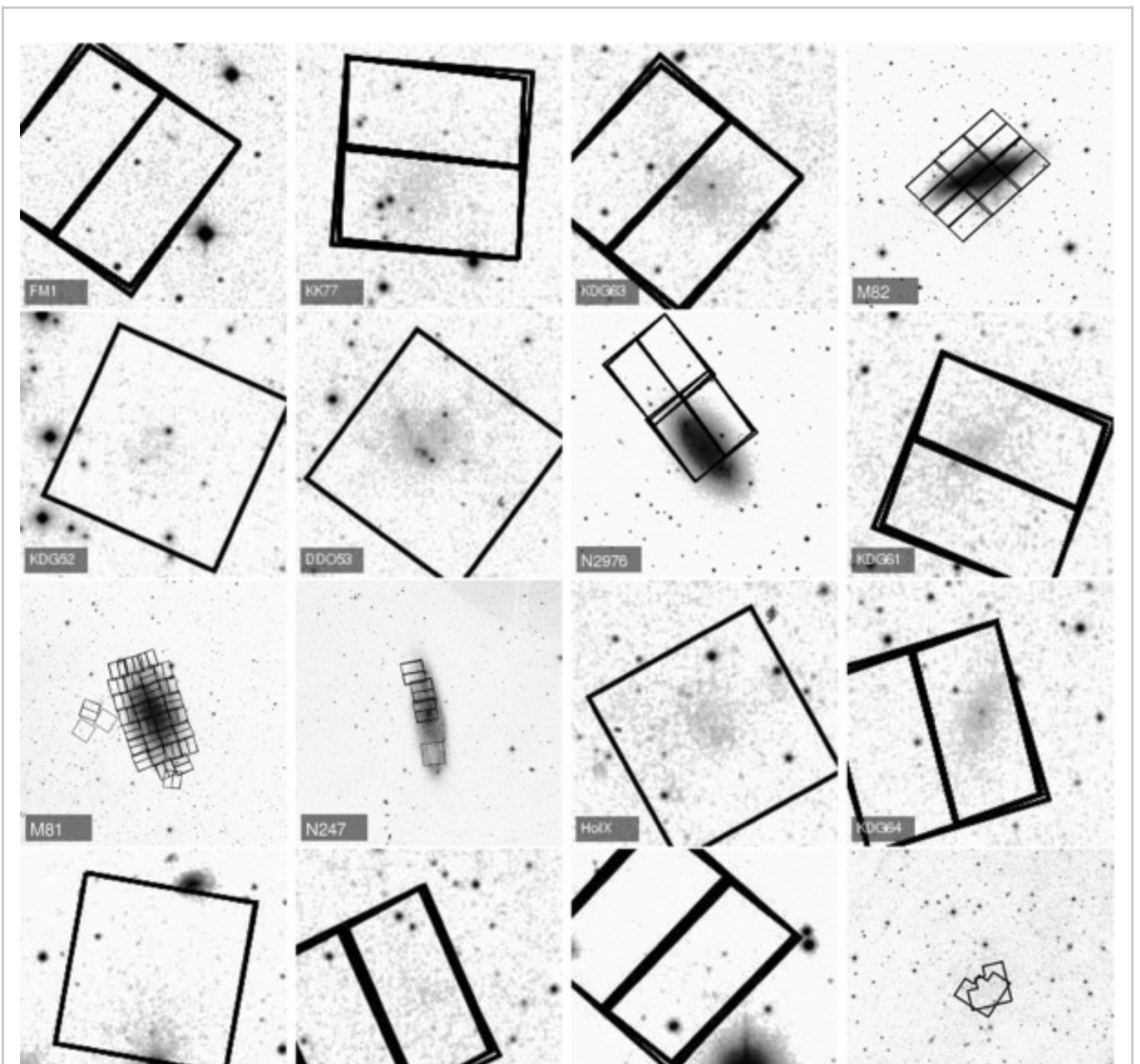
Figure 4. Field positions of images included in Tables 2 and 3, as described in Figure 3. Figures are ordered from the upper left to the bottom right. (a) DDO113; (b) N4214; (c) DDO181; (d) N3741; (e) N4163; (f) N404; (g) UA292; (h) U8833; (i) DDO183; (j) N2366; (k) DDO44; (l) E321-014; (m) U4483; (n) N2403; (o) DDO6; (p) KKH37; (q) HoII; (r) KDG2; (s) MCG9-20-131; (t) E540-032.

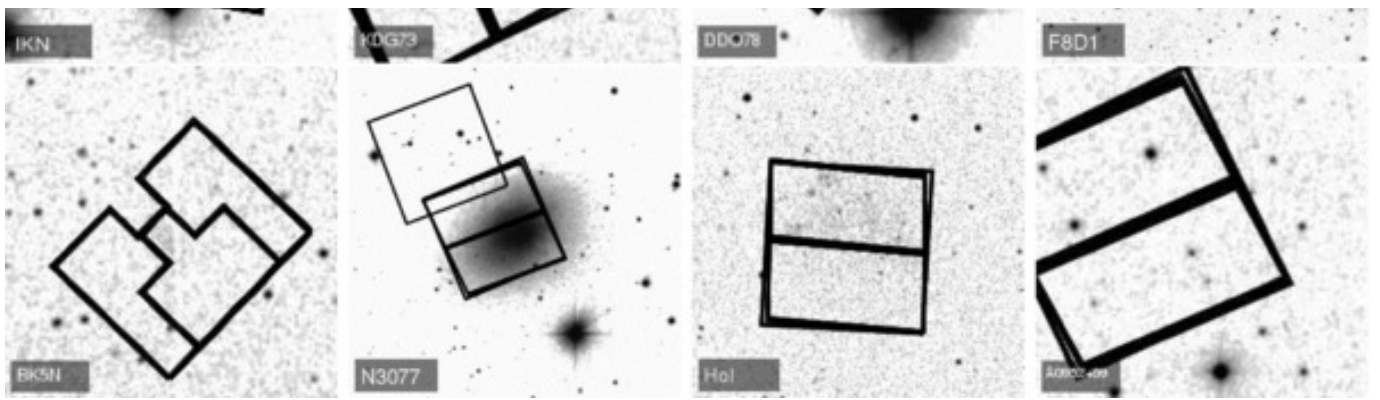
Download figure:

 [Standard image](#)

 [High-resolution image](#)

 [Export PowerPoint slide](#)





 [Zoom In](#)  [Zoom Out](#)

 [Reset image size](#)

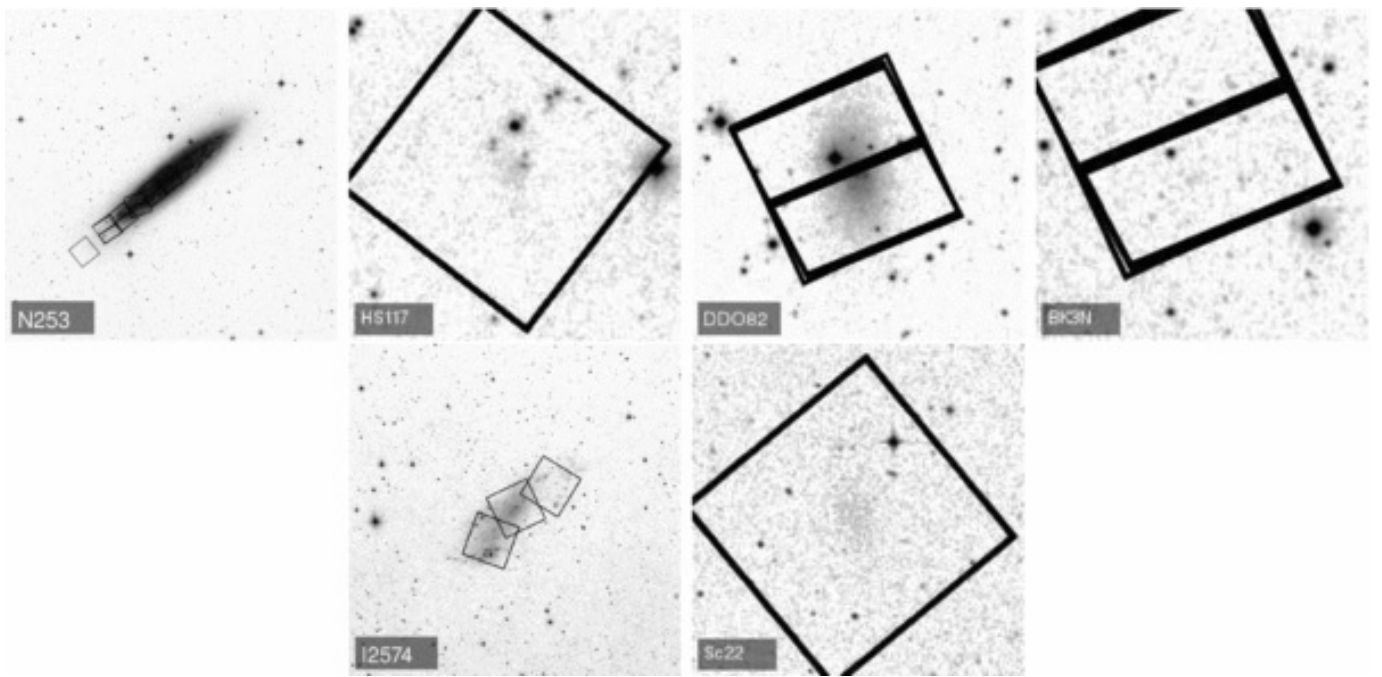
Figure 5. Field positions of images included in Tables [2](#) and [3](#), as described in Figure [3](#). Figures are ordered from the upper left to the bottom right. (a) FM1; (b) KK77; (c) KDG63; (d) M82; (e) KDG52; (f) DDO53; (g) N2976; (h) KDG61; (i) M81; (j) N247; (k) HoIX; (l) KDG64; (m) IKN; (n) KDG73; (o) DDO78; (p) F8D1; (q) BK5N; (r) N3077; (s) HoI; (t) A0952+69.

Download figure:

 [Standard image](#)

 [High-resolution image](#)

 [Export PowerPoint slide](#)



Zoom In Zoom Out

Reset image size

Figure 6. Field positions of images included in Tables 2 and 3, as described in Figure 3. Figures are ordered from the upper left to the bottom right. (a) N253; (b) HS117; (c) DDO82; (d) BK3N; (e) I2574; (f) Sc22.

Download figure:

Standard image

High-resolution image

Export PowerPoint slide

Table 3. Archival Observations

Catalog Name	Target Name	PID	R.A. (J2000)	Decl. (J2000)	Ang. Sep. (')	V3 PA (deg)	Apertu
Antlia	ANTLIA	10210	10 04 03.77	-27 19 47.2	0.14	247.479	WFC1

Catalog Name SexA	Target Name	PID	R.A. (J2000) 10 10	Decl. (J2000) -04 41	Ang. Sep. (^o)	V3 PA (deg)	Apertu WF3-FID
	DDO75	7496	56.9	30	0.983	287.891	
KKR25	KKR25	8601	16 13 47.47	+54 21 27.7	0.83	358.523	WF3-FID
KK230	KK230	9771	14 07 10.70	+35 03 37.0	0.00	18.337	WFC
E410- 005	ESO410-005	10503	00 15 31.4	-32 10 47	0.02	~44	WFC
E294- 010	ESO294-010	10503	00 26 33.4	-41 51 19	0.03	~37	WFC
N55	NGC 0055	9765	00 14 53.60	-39 11 48.0	3.21	174.052	WFCEN
N55	NGC 0055- DISK	9765	00 15 31.03	-39 14 12.0	4.47	245.349	WFCEN
N300	NGC 300-1	9492	00 55 34.12	-37 41 25.4	8.05	80.254	WFC

Catalog Name	Target Name	PID	R.A. (J2000)	Decl. (J2000)	Ang. Sep. ($^{\circ}$)	V3 PA (deg)	Apertu
N300	NGC 300-2	9492	00 54 51.93	-37 38 56.1	2.04	92.050	WFC
N300	NGC 300-3	9492	00 54 55.32	-37 41 48.9	0.94	171.953	WFC
N300	NGC 300-4	9492	00 54 23.12	-37 34 19.9	8.94	80.060	WFC
N300	NGC 300-5	9492	00 54 28.11	-37 38 56.8	5.41	240.928	WFC
N300	NGC 300-6	9492	00 54 26.95	-37 44 11.2	6.17	168.956	WFC
UA438	E407-G18	8192	23 26 30.92	-32 22 44.4	0.926	224.243	WF3-FID

DDO187 Catalog Name	UGC9128 Target Name	10210 PID	14 15 R.A. (J2000)	+33 03 Decl. (J2000)	0.09 Ang. Sep. ($^{\circ}$)	286.046 V3 PA (deg)	WFC1 Apertu
DDO125	UGC7577	8601	12 27 45.64	+43 29 17.0	0.779	293.217	WF3-FD
KKH86	KKH71	8601	13 54 36.15	+04 14 08.1	0.786	301.415	WF3-FD
DDO99	UGC6817	8601	11 50 56.60	+38 52 30.7	0.809	292.285	WF3-FD
DDO181	UGC8651	10210	13 39 53.82	+40 44 20.7	0.01	269.263	WFC1
UA292	UGCA-292	10905	12 38 40.01	+32 46 01.0	0.02	121.995	WFC1
U8833	UGC8833	10210	13 54 48.67	+35 50 14.7	0.01	279.439	WFC
DDO183	UGC8760	10210	13 50 50.98	+38 01 08.0	0.14	274.638	WFC1
N2366	NGC-2366-1	10605	07 28 43.5	+69 11 22	1.19	74.02	WFC
N2366	NGC-2366-2	10605	07 29	+69 14	1.01	95.85	WFC

Catalog Name	Target Name	PID	R.A. 00.0 (J2000)	Decl. 05.2 (J2000)	Ang. Sep. ($^{\circ}$)	V3 PA (deg)	Apertu
E321- 014	PGC39032	8601	12 13 51.38	-38 14 33.8	0.780	330.277	WF3-FD
U4483	UGC4483	8769	08 37 05.40	+69 46 13.6	0.357	164.556	PC1
N2403	SN-NGC2403- PR	10182	07 36 57.22	+65 36 21.5	0.49	140.028	WFC
N2403	NGC2403-X1	10579	07 36 25.56	+65 35 40.1	2.99	95.661	WFC1
N2403	NGC2403- HALO-1	10523	07 37 52.70	+65 31 31.0	7.854	107.68	WFC
N2403	NGC2403- HALO-6	10523	07 37 29.37	+65 40 29.1	5.78	97.839	WFC
KKH37	KKH37	9771	06 47 46.90	+80 07 26.0	0.05	319.556	WFC
HoII	UGC-4305-1	10605	08 18 59.0	+70 42 05	0.92	30.76	WFC

Catalog Name	Target Name	PID	R.A. (J2000)	Decl. (J2000)	Ang. Sep. (")	V3 PA (deg)	Aperture
HoII	UGC-4305-2	10605	08 19 20.6	+70 43 45	1.53	30.67	WFC
E540-030	ESO540-030	10503	00 49 21.2	-18 04 33	0.10	~74	WFC
MCG9-20-131	CGCG-269-049	10905	12 15 44.0	+52 23 58			WF3
E540-032	ESO540-032	10503	00 50 24.5	-19 54 23	0.04	104.385	WFC
E540-032	ESO540-032	10503	00 50 24.51	-19 54 23	0.04	69.516	WFC
FM1	M81F6D1	9884	09 45 20.55	+68 45 26.5	1.06	312.999	WFC
KK77	M81F12D1	9884	09 50 09.28	+67 29 50.1	0.57	6.202	WFC
KDG63	DDO71	9884	10 05 15.74	+66 33 16.5	0.84	316.241	WFC

Catalog Name	Target Name	ID	RA (J2000)	Dec (J2000)	Ang. Sep. ($^{\circ}$)	V3 PA (deg)	Apertu
M82	M82-POS1	10776	09 56 06.7	+69 44 17	3.50	310.02	WFCEN
M82	M82-POS2	10776	09 55 42.0	+69 41 54	1.39	310.02	WFCEN
M82	M82-POS3	10776	09 55 17.0	+69 39 32	3.48	310.02	WFCEN
M82	M82-POS4	10776	09 55 46.7	+69 37 33	3.44	310.02	WFCEN
M82	M82-POS5	10776	09 56 11.8	+69 39 55	1.84	310.02	WFCEN
M82	M82-POS6	10776	09 56	+69 42	3.89	310.02	WFCEN

Catalog Name	Target Name	PID	36.0 R.A. (J2000)	18 Decl. (J2000)	Ang. Sep. (')	V3 PA (deg)	Apertu
KDG52	MESSIER-081- DWARF-A	10605	08 23 55.8	+71 01 46	0.05	297.84	WFC
DDO53	UGC-04459	10605	08 34 07.0	+66 10 55	0.17	302.57	WFC
KDG61	M81K61	9884	09 56 58.78	+68 35 49.6	0.48	15.578	WFC
M81	NGC3031- HALO-1	10523	09 57 17.23	+69 06 29.3	9.58	117.087	WFC
M81	NGC3031- HALO-2	10523	09 58 04.50	+69 08 52.1	14.37	117.321	WFC
M81	M81-X-9	9796	09 57 54.30	+69 03 46.4	12.61	14.181	WFC1
M81	M81-X-9	9796	09 57 54.30	+69 03 46.4	12.61	323.352	WFC
M81	M81-FIELD-1	10584	09 54 16.40	+69 13 40.0	11.93	329.925	WFCEN

Catalog Name	Target Name	PID	16.49 R.A. (J2000)	42.5 Decl. (J2000)	Ang. Sep. ($^{\circ}$)	V3 PA (deg)	Apertu
M81	M81-FIELD-2	10584	09 54 52.27	+69 14 54.3	11.57	59.748	WFCEN
M81	M81-FIELD-3	10584	09 54 09.18	+69 09 49.5	9.51	64.655	WFCEN
M81	M81-FIELD-4	10584	09 54 41.78	+69 11 06.7	8.47	68.571	WFCEN
M81	M81-FIELD-5	10584	09 55 13.52	+69 12 25.1	8.60	329.926	WFCEN
M81	M81-FIELD-6	10584	09 55 46.09	+69 13 42.4	9.77	329.926	WFCEN
M81	M81-FIELD-7	10584	09 54 17.45	+69 08 27.4	8.115	64.984	WFCEN
M81	M81-FIELD-7	10584	09 54 22.89	+69 06 56.8	6.95	329.926	WFCEN
M81	M81-FIELD-8	10584	09 54	+69 08	5.43	329.926	WFCEN

Catalog Name	Target Name	PID	55.47 R.A. (J2000)	14.2 Decl. (J2000)	Ang. Sep. (^o)	V3 PA (deg)	Apertu
M81	M81-FIELD-9	10584	09 55 11.57	+69 08 49.8	5.21	329.862	WFCEN
M81	M81-FIELD-9	10584	09 55 28.04	+69 09 31.5	5.55	329.926	WFCEN
M81	M81-FIELD-10	10584	09 56 00.66	+69 10 49.0	7.23	334.924	WFCEN
M81	M81-FIELD-11	10584	09 54 32.00	+69 05 33.9	5.71	65.041	WFCEN
M81	M81-FIELD-11	10584	09 54 38.25	+69 04 02.3	4.94	67.905	WFCEN
M81	M81-FIELD-12	10584	09 55 09.99	+69 05 20.6	2.49	329.927	WFCEN
M81	M81-FIELD-13	10584	09 55 26.13	+69 05 56.4	2.05	329.919	WFCEN
M81	M81-FIELD-13	10584	09 55 43.41	+69 06 37.0	2.76	69.764	WFCEN

M81 Catalog Name	M81-FIELD-14 Target Name	10584 PID	09 56 R.A. (1500)	+69 07 Dec. (5200)	5.41 Ang. Sep. (^o)	333.980 V3-PA (deg)	WFCEN Apert
M81	M81-FIELD-15	10584	09 54 35.17	+69 00 33.4	6.25	333.265	WFCEN
M81	M81-FIELD-15	10584	09 54 52.01	+69 01 10.0	4.67	338.616	WFCEN
M81	M81-FIELD-16	10584	09 55 25.11	+69 02 22.0	1.80	159.951	WFCEN
M81	M81-FIELD-17	10584	09 55 40.69	+69 03 02.7	1.15	329.863	WFCEN
M81	M81-FIELD-17	10584	09 55 57.09	+69 03 44.5	2.12	329.927	WFCEN
M81	M81-FIELD-18	10584	09 56 30.51	+69 05 00.8	5.19	69.765	WFCEN
M81	M81-FIELD-19	10584	09 54 49.72	+68 57 40.0	7.45	333.321	WFCEN
M81	M81-FIELD-19	10584	09 55 07.30	+68 58 15.2	6.21	69.766	WFCEN

Catalog Name	Target Name	PID	R.A. (J2000)	Decl. (J2000)	Ang. SLP	V3 PA (deg)	Aperture
M81	M81-FIELD-20	10584	09 55 39.04	+69 00 33.5	4.47 (^o)	329.927	WFCEN
M81	M81-FIELD-21	10584	09 55 55.25	+69 00 09.3	4.31	329.920	WFCEN
M81	M81-FIELD-21	10584	09 56 11.62	+69 00 50.9	4.64	329.927	WFCEN
M81	M81-FIELD-22	10584	09 56 45.03	+69 02 07.3	6.66	69.765	WFCEN
M81	M81-FIELD-23	10584	09 55 21.82	+68 55 21.6	8.70	69.767	WFCEN
M81	M81-FIELD-24	10584	09 55 53.57	+68 56 40.0	7.55	329.927	WFCEN
M81	M81-FIELD-25	10584	09 56 26.98	+68 57 56.4	7.72	69.766	WFCEN
M81	M81-FIELD-26	10584	09 56 59.55	+68 59 13.8	9.06	68.603	WFCEN
M81	M81-FIELD-27	10584	09 55 59.05	+68 53 27.4	10.72	63.395	WFCEN

Catalog Name	Target Name	PID	R.A. (J2000)	Decl. (J2000)	Ang. Sep. ($^{\circ}$)	V3 PA (deg)	Apertu
M81	M81-FIELD-28	10584	09 56 29.23	+68 54 42.5	10.49	69.769	WFCEN
M81	M81-FIELD-29	10584	09 57 01.91	+68 55 56.2	11.26	69.768	WFCEN
N247	NGC247	9771	00 47 06.10	-20 39 04.0	6.55	263.664	WFC
HoIX	UGC-5336	10605	09 57 31.8	+69 02 46	0.22	325.36	WFC
KDG64	M81K64	9884	10 07 09.85	+67 49 57.9	0.81	78.806	WFC
IKN	IKN	9771	10 08 05.90	+68 23 57.0	0.00	187.352	WFC
F8D1	GAL- 094447+672619	5898	09 44 44	+67 26 41	0.5	~320	PC1

Catalog Name	Target Name	PID	R.A.	Decl.	Ang.	V3 PA	Aperture
BK5N	GAL- 100441+681522	5898	10 04 (20.4)	+68 15 (28.0)	0.544 (8.4)	355.514 (deg)	PC1
BK5N	GAL- 100441+681522	6964	10 04 35.7	+68 15 17.2	0.432	264.979	PC1
N3077	NGC3077- PHOENIX	9381	10 03 51.6	+68 41 26	3.80	335.19	WFC
HoI	UGC-5139	10605	09 40 32.1	+71 11 15	0.33	9.156	WFC
HS117	HS117	9771	10 21 25.20	+71 06 58.0	0.00	127.715	WFC
I2574	IC-2574-1- COPY	10605	10 28 22.9	+68 24 37	0.33	336.13	WFC
I2574	IC2574-SGS	9755	10 28 43.2	+68 27 06	2.84	21.49	WFC
I2574	IC-2574-2	10605	10 27 50.1	+68 22 57	3.57	32.67	WFC

Catalog Name	Target Name	PID	R.A. (J2000)	Decl. (J2000)	Ang. Sep.	V3 PA (deg)	Apertu
Sc22	SCL-DE1	10503	00 23	-24 42	0.60	50.4	WFC
			51.7	18			

Notes. Entries with reduced precision in the listings for R.A. and decl. indicate a representative center for dithered observations. Multiple dates for a given field indicate the start times for the earliest and the latest observations of that field. Angular separation refers to separation between the aperture position and the catalog coordinates in Table 1. Field names indicate the titles given in the archive. Observations lacking multiple filters at nearly the same position and alignment are not included. [a] Observations for N4190 were proprietary at the time this paper was submitted; their photometry will be added to the data release when it becomes public. References for published CMDs from the associated data are given in the last column: (1) Tully et al. [2006](#); (2) Dohm-Palmer et al. [2002](#); (3) Karachentsev et al. [2006](#); (4) Weisz et al. [2008](#); (5) Seth et al. [2005a](#); (6) Butler et al. [2004](#); (7) Rizzi et al. [2006](#); (8) Caldwell et al. [1998](#); (9) Karachentsev et al. [2001](#); (10) Karachentsev et al. [2002c](#); (11) Karachentsev et al. [2002b](#); (12) Dolphin et al. [2001](#); (13) Izotov & Thuan [2002](#).

Download table as:

Typeset images:

Among the galaxies eligible for a full radial strip, we did not image M81 or M82. The former had complete tiling through programs GO-10250 (F814W only) and GO-10584 (F435W, F606W, and some F814W in outer fields). M82 was tiled by STScI through program DD-10776 (Mutchler et al. [2007](#)). Only the M81 photometry from GO-10584 is

presented here; the F814W tiling in GO-10250 was not aligned in either pointing or rotation with the bluer observations in GO-10584, and thus requires capabilities not included in the current data processing pipeline.

3.2. Deep Field Pointing

A single deep pointing was originally planned for each of the 12 galaxies which dominate the K -band luminosity (and presumably the stellar mass) of the local universe. The deep field exposure times were chosen to provide high completeness in the red clump region of the CMD, as described below. However, deep exposures are subject to significant stellar crowding due to the increasing number of stars at fainter magnitudes in the CMD. When stellar fields become too crowded, longer exposure times no longer decrease the photometric errors or increase the number of detected stars. Instead, the photometric uncertainties are dominated by systematic errors produced by crowded, blended point-spread functions (PSFs). To avoid this situation, the deep fields needed to be placed in regions of the galaxies where photometric errors would not be dominated by crowding.

When placing the deep fields, we used the simulations of Olsen et al. ([2003](#)) to calculate the surface brightness below which photometric errors would be less than 0.1 mag in the red clump. This limiting surface brightness depends on distance, the underlying stellar population, and the pixel scale and PSF of the camera. We found typical ACS limiting surface brightness of $\mu_V \sim 22.2\text{--}24.6 \text{ mag arcsec}^{-2}$ for galaxies at $D = 1.3\text{--}4 \text{ Mpc}$. These limits yielded of order 100K stars per ACS FOV at our typical exposure time, which was consistent with our previous experience with an ACS snapshot survey (Seth et al. [2005b](#)). The resulting limiting surface brightnesses were used to identify appropriate field locations for each of the target galaxies,

using a combination of Two Micron All Sky Survey (2MASS), Sloan Digital Sky Survey (SDSS), and deep Malin (<http://www.aao.gov.au/images/>) images to estimate the local surface brightness along each galaxy's major axis. The fields were allowed to have any orientation, and were contiguous with the outermost wide field tile.

3.3. Filter Choice

Imaging was carried out in three filters for the galaxies that dominate the recent star formation in the local volume (i.e., to the right of the line in the left panel of Figure 1), and two filters for all others. For the galaxies with three-filter coverage, we used F475W+F606W+F814W, which maximized the combination of wavelength coverage and throughput. The three filters are useful for identifying X-ray counterparts, H α region nebulosity, and extinction (when combined with future UV or NIR imaging). Although the F435W filter allows for a larger wavelength baseline and disjoint wavelength coverage with F606W, its throughput is much less than that of F475W.

For the dwarf galaxies with two-filter coverage, we used a F475W+F814W filter combination, instead of the more commonly used F606W+F814W. Although F475W does not reach as far down the CMD as F606W for a given exposure time, it provides greater temperature sensitivity due to the longer wavelength baseline of the F475W-F814W color combination. For regions above the red clump, more scientific information can be extracted from better temperature sensitivity than from the slight gain in depth possible with F606W+F814W. This choice allowed us to better separate main-sequence stars from the blue helium burning sequence, and to derive stronger constraints on the metallicity distribution of red giant branch (RGB) stars. This effect can be seen in Figures 9–22, when comparing CMDs in F475W+F814W and F606W+F814W for galaxies with three-

filter observations (such as DDO 190). Given the very low extinctions expected in low-metallicity systems, a third filter was not deemed necessary for the faintest dwarf galaxies. For many of these, some F606W imaging is already available in the archive, largely from the SNAP-9771 and SNAP-10210 programs.

For the deep fields, the scientific demand of constraining ancient star formation requires the highest possible completeness in the red clump. Thus, the majority of time invested in deep fields was in the more traditional F606W+F814W color combination, which maximizes the depth along the RGB at the expense of lower color sensitivity. A single orbit of F475W was also included for continuity with the wide-field observing strategy, and to allow the possibility for extinction mapping in the future.

3.4. Exposure Times

Exposure times were chosen to achieve two separate goals. For the wide fields, the goal was efficient, multi-color imaging of the upper regions of the CMD, allowing good constraints on the occupation of the main sequence, the luminosity function of the blue and red helium burning sequences, the color distribution of the RGB, and the population of asymptotic giant branch (AGB) stars. For the deep field, the goal was high completeness and photometric accuracy in the red clump. We discuss the details of the wide field and deep field observations in Sections [3.4.1](#) and [3.4.2](#). A listing of the new observations taken for this program can be found in Table [2](#).

3.4.1. Wide Fields

The wide field observing strategy was shaped by the need to get up to three filters at each tile position. In each filter we need at least a two- or three-point dither pattern to reject cosmic rays and to cover the chip gap. Due to data volume constraints, two orbits are required to get at

least two images in each of the three filters. For crowded areas, we used the minimum two orbits for the wide-field tilings, while in the outermost wide fields, where crowding was not a limiting factor on the photometry, we used three orbits, one orbit per filter. For dwarf galaxies, we devoted one orbit to each of the two filters. Total exposure times can be found in Table 2. The typical photometric depths ($S/N=5$) were 28.4 in F475W and F606W, and 27.5 in F814W for a single orbit.

3.4.2. Deep Fields

The goal of the ANGST deep fields is to obtain an accurate census on the number, magnitude, and color of stars in the red clump. These stars place a strong constraint on the ancient SFH enabling the possibility of breaking the age–metallicity degeneracy present along the upper RGB. We requested deep fields for 12 galaxies in the ANGST volume with $M_K < -17.5$. These 12 galaxies contain 99% of the K-band luminosity within our survey volume, and thus have dominated the past total SFH. The significant time investment required to obtain CMDs reaching below the red clump meant that these exposures were limited to a single field in each galaxy.

Exposure times were chosen to obtain $S/N \gtrsim 10$ in both F606W and F814W for stars in the red clump. In practice, we achieved this by using the ACS Imaging Exposure Time Calculator to estimate the time necessary to reach $S/N=3.5$ for a G0III star normalized to $M_V = +1.5$ (for F606W) and $M_I = +0.7$ (for F814W), a magnitude below the theoretical red clump for a $[Fe/H] = -1.3$, 10 Gyr population in the Padova isochrones (<http://pleiadi.pd.astro.it/>). To calculate the appropriate red clump magnitude for each galaxy, reddenings and extinctions were adopted from Schlegel et al. (1998), and distance moduli were chosen by carefully evaluating data from the literature (Karachentsev et al. 2002a, 2003; Rekola et al. 2005; Mouhcine et al. 2005; Sakai & Madore 2001; Karachentsev et al. 2006; Freedman et al.

[1994](#); Sakai & Madore [1999](#); Tikhonov et al. [2003](#); Maíz-Apellániz et al. [2002](#); Drozdovsky et al. [2002](#); Gieren et al. [2004](#), [2005](#); Rizzi et al. [2006](#); Minniti et al. [1999](#); Méndez et al. [2002](#); Aparicio & Tikhonov [2000](#)) and from our own TRGB measurements using archival data. Exposure times were turned into orbit estimates using the appropriate overheads and available visibility times depending on the declination of the source. For the two deep exposures of M81 and NGC 2976 that were obtained with ACS before its failure, a single long exposure (~ 2700 s) was taken in each orbit. Each visit contained an orbit in each filter both to maximize our baseline for variable stars and to minimize the risk of obtaining incomplete filter coverage in the event of spacecraft failure. A short 100 s exposure was taken to permit photometry of the brighter stars saturated in the full orbit exposures, and a full orbit of F475W data was included for consistency with the wide fields and to enable the possibility of internal reddening estimations.

3.5. Parallels

WFPC2 observations were taken in parallel with the ACS observations in Table [2](#). These observations were divided evenly between F606W and F814W, and are 6' away from the center of the ACS FOV. Photometry of these fields will be reduced with the WFPC2 pipeline described below in Section [7](#), but is not included in this initial data release.

4. WFPC2 OBSERVING STRATEGY

ACS observations for our program began in early 2006 September. Unfortunately, the wide field camera on ACS failed in late 2007 January, ~ 5 months into the execution of our program. As a result, we lost 147 orbits on the massive galaxies with deep fields ($M_K < -17.5$; 71% lost), and lost 44 orbits on the fainter galaxies (50% lost), for a total of 191 orbits lost from the original allocation of 295 orbits. Of the 195 orbits that were to be devoted to the deep fields, we received 41

orbits (79% lost), primarily for NGC 2976 and M81. Given the uncertainties in the upcoming HST servicing mission, we decided to continue the program with WFPC2.

Following an appeal, the Telescope Time Review Board restored 116 of the 191 lost orbits to execute deep single-pointing observations for the nearest luminous galaxies and the very closest dwarfs (NGC 55, NGC 4214, NGC 404, NGC 2403, NGC 3109, Sex B, and IC 5152). Time for wide field observations was not granted. For the majority of these galaxies, sufficient data exist in the archive for tying the large radius deep fields to the SFH of the galaxy as a whole, although with a lack of complete radial coverage and uniformity. However, NGC 55 and NGC 3109 did not have adequate radial coverage due to their large angular extents. Through a Director's Discretionary request (DD-11307), we were awarded an additional 25 orbits to execute radial tilings for these two remaining galaxies (five pointings per galaxy, with two orbits per tile for NGC 3109 and three orbits per tile for NGC 55).

4.1. WFPC2 Deep Fields

Transferring the ANGST deep field observing strategy to WFPC2 required a number of modifications. The first significant change was in field placement. The wide-field chips of WFPC2 are undersampled compared to ACS, leading to larger photometric errors due to crowding at comparable surface brightnesses and exposure times. We therefore had to move the deep fields to even lower surface brightnesses (and thus larger radii) than the original ACS deep field locations. Using the Olsen et al. ([2003](#)) simulations, we recalculated the surface brightness limit at which our observations would become crowding limited. These revised limits were ~ 1.5 mag fainter than for ACS. These changes required shifting the fields typically another ~ 1.4 disk scale lengths further out, increasing the risk that the WFPC2 FOV would fall beyond any significant disk truncation, if present. This

appears to have happened for IC 5152, but did not affect any of the other observations.

The second adaptation was to accept slightly less photometric depth. WFPC2's throughput is substantially worse than ACS's, and thus matching the depth of the ACS deep fields would require a prohibitive number of orbits. However, our experience with the ACS deep fields for M81 and NGC 2976 suggested that we could reach our scientific goals with slightly shallower data, and thus we revised our target depth to a signal-to-noise ratio of 3 at 1.5 mag below the middle of the red clump. The final change to the program was to eliminate the F475W observations, where WFPC2's sensitivity is particularly poor.

When allocating orbits, we maximized the photometric accuracy in the red clump (where $F606W - F814W \approx 0.75$) by allocating twice as many orbits to F814W than to F606W. A random-walk dither pattern was adopted and full-orbit exposures were used; the number (>5) of exposures made cosmic-ray rejection straightforward without the need to CR-split the exposures during the orbit, allowing us to obtain the maximum depth possible with each orbit.

The resulting images typically had between 5000 and 15000 stars per WFPC2 chip. We checked our photometry on a chip-by-chip basis to identify potential problems or offsets due to the well-known WF4 bias anomaly. Images of WF4 showed no obvious problems with the bias, nor was the photometry noticeably worse, suggesting that the anomaly had been properly addressed by STScI's WFPC2 data reduction pipeline and/or that the chip was performing well at the time the observations were performed. We therefore are including WF4 data in the released photometric catalogs. These catalogs include a flag identifying the chip that a star fell on in the reference image, allowing the user to filter out WF4 data, if needed.

4.2. WFPC2 Wide Field Tilings

For the WFPC2 wide field tilings of NGC 55 and NGC 3109, we aimed to match the depth (in absolute magnitude) of the wide radial tiles in the more distant systems of the ANGST survey, assuring that the WFPC2 tiles were at least as deep as the shallowest wide field tiles in the survey. This depth corresponds to a signal-to-noise of 5 and 50% completeness at $M_{F814W} = -0.5$ for the colors of the RGB. At the distances of NGC 3109 (1.3 Mpc; $m_{lim, F814W} = 25.1$) and NGC 55 (2.1 Mpc; $m_{lim, F814W} = 25.8$), we could reach this depth and completeness in two orbits for NGC 3109 and three orbits for NGC 55, including overheads for CR-SPLITs and guide-star acquisition, based on comparable two-orbit observations for Sextans A (Dohm-Palmer et al. [1997](#)) and WFPC2 parallel data from the main ANGST ACS observations.

To produce a radial strip, we adopted a "Groth strip" tiling strategy of interleaved chips, with an orientation set to maximize schedulability for each target. Unlike the original ANGST ACS program, we did not tile all the way out to the deep fields, which had to be moved even further out to cope with WFPC2's lower resolution. We instead stopped the radial tiling where we are sure that we have imaged most of the recent star formation. To conserve orbits, tiles were placed on whichever side of the galaxy presented the smallest distance to the edge of the star-forming disk.

5. ARCHIVAL DATA

The original ANGST survey strategy was designed to take advantage of archival data whenever it matched or surpassed the quality of the proposed observations, in comparable filters. The failure of ACS during execution of the ANGST program further increased our reliance on archival data. In [Table 3](#) we summarize the archival data sets that are incorporated into the ANGST data release, along with

papers that have published CMDs from these data independently. We have excluded data sets that have only one filter at a single position, or that have severe offsets or misalignments among multiple filters. Photometry in the latter cases is significantly compromised by the distortion of the ACS WFC, and cannot be readily produced by the ANGST pipeline. In future data releases, we will incorporate such data as needed, most notably for the F814W tilings of M81 by GO-10250.

6. ACS PHOTOMETRY

Photometry was carried out on bias subtracted, flat-fielded *_flt images (or *_crj images when available) produced by the STScI ACS pipeline OPUS versions 2006_5 through 2008_1, which used CALACS version 4.6.1. through 4.6.4. For *_crj images, the value of the readnoise reported in the CALACS header did not reflect that the final image contains two co-added readouts. In these cases, we multiplied the read noise listed in the header by $\sqrt{2}$, so that it properly accounted for the combined read noise of the co-added CR-SPLIT observations. Failure to make this correction would have produced systematic errors in the reported photometric errors.

To measure stellar photometry, we used the software package DOLPHOT²⁰ (Dolphin et al. [2002](#)) including the ACS module. This package is optimized for measuring photometry of stars on dithered ACS images, where the position angle of the multiple exposures are the same, and the shifts between exposures are small ($\lesssim 30''$). To align images, DOLPHOT makes a fast initial pass through the data to find bright stars common to all of the frames, using approximate shifts supplied by the user. The final shifts between the images are then determined based on these stars. By this method, our exposures were able to be aligned to ~ 0.01 precision. The precision is slightly worse (~ 0.015) for fields with small numbers of stars, and slightly better (~ 0

#005) for more crowded fields. When aligning images, we currently do not incorporate time-dependent corrections to the geometric distortion. While improved distortion corrections would help improve the astrometric solution for the frames, it has only a second-order effect on our photometry, since the photometric accuracy depends primarily on multiple images being aligned correctly relative to each other, rather than relative to an undistorted frame. As we currently are only analyzing stacks of images with small positional shifts, taken close together in time, temporal drifts in the geometric distortion are not a limiting factor in our photometry. They will, however, be considered in future releases.

Although DOLPHOT operates on non-drizzled images, we also combined all images into a single drizzled image using the `multidrizzle` task within PyRAF (Koekemoer et al. [2002](#)), which allowed us to flag the cosmic rays in the individual images. Once the cosmic rays were identified, the photometry was measured for all of the objects using the individual, uncombined frames.

To calculate the flux of each star, DOLPHOT initially adopts the PSF calculated by Tiny Tim (Krist [1995](#)), and scales the PSF in flux to minimize residuals throughout the image stack. The shape and width of the Tiny Tim PSF has been shown to match to the shape of the true PSF well throughout both ACS chips, based on the extensive analysis presented by Jee et al. ([2007](#)). There are slight deviations close to the bottom of Chip 1, but our tests in Section [8](#) find that these do not lead to noticeable systematics in the magnitude errors. DOLPHOT makes additional minor adjustments to the Tiny Tim PSF by using the brightest and most isolated stars to correct for PSF changes due to temperature variations of the telescope during orbit. These adjustments typically affect the photometry at the 0.01 mag level.

DOLPHOT also uses the most isolated stars in the field to determine

aperture corrections to the PSF magnitudes, which accounts for any systematic differences between the model and true PSF. These corrections were generally $\lesssim 0.05$ mag for a given exposure. DOLPHOT then applies the aperture corrections for each exposure, corrects for the charge transfer efficiency of the ACS detector using the coefficients given in the ACS-ISR 2004-006,²¹ combines the results from the individual exposures, and converts the measured count rates to the VEGAMAG system (a system where Vega is defined to have mag=0 in all filters) using the Sirianni et al. (2005) zero points for each filter. Note that the Sirianni et al. (2005) zero points have since been updated in ACS-ISR 2007-02 to reflect the change in sensitivity due to the increase in ACS's operating temperature in 2006 July after the switch to Side 2 electronics; these changes are of order ~ 0.015 mag, and have been propagated into the relevant photometric catalogs covered in this release. The resulting zero points match those in Table 5 of ACS-ISR 2007-02. We have not yet propagated zero point changes due to improvements in the calibration of the system throughput (ACS-ISR 2007-06); these changes seem to be of the order of less than 0.01 in the filters covered in this data release, but still have significant unresolved uncertainties in the red wavelength regimes that dominate much of the ANGST catalogs.

DOLPHOT makes use of all exposures of a field when measuring stellar properties. This technique results in a single raw photometry output file for each field that contains measured properties of all objects detected in the field, including the position, object type (point source, extended, elongated, or indeterminate), combined magnitude, magnitude error, signal-to-noise, sharpness, roundness, χ^2 fit to the PSF, crowding, and error flag (chip edge or saturated) in all filters. The output catalog contains these measurements for each star in each individual exposure as well, providing the opportunity for variability studies.

We spent significant time investigating optimal values for the dozens of parameters that can be adjusted in DOLPHOT to maximize the quality of the photometry measured from the data. Three of the parameters which had the strongest influence on our resulting photometry were the `Force1` parameter, the aperture radius (`RAper`), and the sky fitting parameter (`FitSky`).

The `Force1` parameter forces all sources detected to be fitted as stars, assuming that separate culling will be performed on the output file to discard non-point sources. For our crowded fields, this option was optimal, but required that special care be taken in fitting the sky. We found that with `FitSky` set to 1 (fit the sky in an annulus around each star), our photometry was much more heavily affected by crowding, resulting in large crowding errors for nearly all of the stars in our wide field data. With `FitSky` =2 (fit the sky inside the PSF radius but outside the photometry aperture), we needed a small aperture radius (4 pixels), and found systematic errors (~ 0.02 mag) in the recovered magnitudes of artificial stars added to the data, using bright stars whose random photometric uncertainties did not overwhelm the systematic error. We found that setting `FitSky` =3 (fit the sky within the photometry aperture as a two-parameter PSF fit) allowed a larger photometry radius (10 pixels) with smaller aperture correction, and provided photometry with the smallest crowding errors and no significant systematic errors. Note that in all these methods DOLPHOT subtracts the flux of neighboring stars before measuring the sky and stellar flux; differences in the operation of `FitSky` therefore change the way residuals propagate, but not the total flux of nearby stars.

We provide full photometry output for each field along with culled catalogs containing the highest quality photometry. We culled the raw DOLPHOT output in two ways, releasing both a complete and a conservative (but very high quality) catalog for each field. The

complete catalog contains all sources that were not flagged by DOLPHOT as extended, elongated, extremely sharp, highly saturated, significantly cut off by the edge of the chip, or not detected at high signal-to-noise (4.0 or higher in at least two filters).

In addition to the complete catalog, we also provide a more conservative catalog of stellar photometry which has been culled to remove highly uncertain photometry. These catalogs have been filtered to only allow objects with low sharpness ($(\mathbf{sharp}_1 + \mathbf{sharp}_2)^2 \leq 0.075$) and crowding ($(\mathbf{crowd}_1 + \mathbf{crowd}_2) \leq 0.1$) in both filters. The sharpness parameter cut removes extended objects such as background galaxies missed by the earlier cuts. The crowding parameter gives the difference between the magnitude of a star measured before and after subtracting the neighboring stars in the image. When this value is large, it suggests that the star's photometry was significantly affected by crowding effects, and we therefore exclude it from our most conservative catalogs. Quality cuts based on the χ^2 values were also considered, but they were rejected when a correlation was found between χ^2 and the local background.

We found that these final cuts produce CMDs with well-defined features in the uncrowded field, while retaining most of the stars in high surface brightness regions. However, the cuts in the more conservative catalog may remove stars from certain interesting regions, like stellar clusters. We advise anyone interested in studying clusters or identifying stellar counterparts for specific sources to check the effects of the different parameter cuts. In Gogarten et al. ([2009](#)), we found that relaxing the crowding parameter cuts to $\mathbf{crowd}_1 + \mathbf{crowd}_2 \leq 0.6$ recovered a number of stars in clusters without dramatically compromising the quality of the photometry.

Our final catalogs include stars that may contain some saturated

pixels, as long as the saturation was not so bad that the PSF could not be reliably fitted. Saturation limits our wide field photometry to magnitudes fainter than ~ 18 and our deep field photometry to magnitudes fainter than ~ 20 . In Table 4 we give the level of 50% photometric completeness for each observation, as determined from initial artificial star tests. These completeness limits are for the field as a whole, but can be expected to vary spatially within a field due to spatial variations in the degree of crowding.

Table 4. Photometry

Catalog Name	Proposal ID	Target Name	Instrument	Filter	Exposure Time (s)
Antlia/P29194	10210	ANTLIA	ACS	F606W	985
Antlia/P29194	10210	ANTLIA	ACS	F814W	1174
SexA/DDO75	7496	DDO75	WFPC2	F555W	19200
SexA/DDO75	7496	DDO75	WFPC2	F814W	38400
N3109	10915	NGC3109-DEEP	WFPC2	F606W	2700
N3109	10915	NGC3109-DEEP	WFPC2	F814W	3900
N3109	11307	NGC3109-WIDE1	WFPC2	F606W	2700
N3109	11307	NGC3109-WIDE1	WFPC2	F814W	3900
N3109	11307	NGC3109-WIDE2	WFPC2	F606W	2700
N3109	11307	NGC3109-	WFPC2	F814W	3900

Catalog Name	Proposal ID	Target Name	Instrument	Filter	Exposure Time (s)
N3109	11307	NGC3109- WIDE3	WFPC2	F606W	2400 (s)
N3109	11307	NGC3109- WIDE3	WFPC2	F814W	2400
N3109	11307	NGC3109- WIDE4	WFPC2	F606W	2400
N3109	11307	NGC3109- WIDE4	WFPC2	F814W	2400
SexB/DDO70	10915	SEXB-DEEP	WFPC2	F606W	2700
SexB/DDO70	10915	SEXB-DEEP	WFPC2	F814W	3900
KKR25	8601	KKR25	WFPC2	F606W	600
KKR25	8601	KKR25	WFPC2	F814W	600
KK230	9771	KK230	ACS	F606W	1200
KK230	9771	KK230	ACS	F814W	900
E410-005/KK3	10503	ESO410-005	ACS	F606W	8960
E410-005/KK3	10503	ESO410-005	ACS	F814W	22400
E294-010	10503	ESO294-010	ACS	F606W	13920
E294-010	10503	ESO294-010	ACS	F814W	27840
N55	9765	NGC0055	ACS	F606W	400
N55	9765	NGC0055	ACS	F814W	676
N55	9765	NGC0055- DISK	ACS	F606W	676
N55	9765	NGC0055- DISK	ACS	F814W	700

N55 Catalog Name	10915 Proposal ID	NGC0055- Target Name DEEP	WFPC2 Instrument	F606W Filter	6000 Exposure Time (s)
N55	10915	NGC0055- DEEP	WFPC2	F814W	10800 ^(s)
N55	11307	NGC0055- WIDE1	WFPC2	F606W	2000
N55	11307	NGC0055- WIDE1	WFPC2	F814W	3700
N55	11307	NGC0055- WIDE2	WFPC2	F606W	1800
N55	11307	NGC0055- WIDE2	WFPC2	F814W	2600
N55	11307	NGC0055- WIDE3	WFPC2	F606W	2700
N55	11307	NGC0055- WIDE3	WFPC2	F814W	3900
N55	11307	NGC0055- WIDE4	WFPC2	F606W	2700
N55	11307	NGC0055- WIDE4	WFPC2	F814W	3900
N55	11307	NGC0055- WIDE5	WFPC2	F606W	2700
N55	11307	NGC0055- WIDE5	WFPC2	F814W	3900
I5152/E237-27	10915	IC5152-DEEP	WFPC2	F606W	4800
I5152/E237-27	10915	IC5152-DEEP	WFPC2	F814W	9600
GR8/DDO155	10915	GR8	ACS	F475W	2244
GR8/DDO155	10915	GR8	ACS	F814W	2259

Catalog Name	Proposal	Target Name	Instrument	Filter	Exposure Time (s)
N300	10915	NGC0300- WIDE1	ACS	F475W	1488 (s)
N300	10915	NGC0300- WIDE1	ACS	F606W	1515
N300	10915	NGC0300- WIDE1	ACS	F814W	1542
N300	10915	NGC0300- WIDE2	ACS	F475W	1488
N300	10915	NGC0300- WIDE2	ACS	F606W	1515
N300	10915	NGC0300- WIDE2	ACS	F814W	1542
N300	10915	NGC0300- WIDE3	ACS	F475W	1488
N300	10915	NGC0300- WIDE3	ACS	F606W	1515
N300	10915	NGC0300- WIDE3	ACS	F814W	1542
N300	9492	NGC300-1	ACS	F435W	1080
N300	9492	NGC300-1	ACS	F555W	1080
N300	9492	NGC300-1	ACS	F814W	1440
N300	9492	NGC300-2	ACS	F435W	1080
N300	9492	NGC300-2	ACS	F555W	1080
N300	9492	NGC300-2	ACS	F814W	1440
N300	9492	NGC300-3	ACS	F435W	1080
N300	9492	NGC300-3	ACS	F555W	1080

Catalog Name	Proposal ID	Target Name	Instrument	Filter	Exposure Time (s)
N300	9492	NGC300-3	ACS	F814W	1440
N300	9492	NGC300-4	ACS	F435W	1080
N300	9492	NGC300-4	ACS	F555W	1080
N300	9492	NGC300-4	ACS	F814W	1440
N300	9492	NGC300-5	ACS	F435W	1080
N300	9492	NGC300-5	ACS	F555W	1080
N300	9492	NGC300-5	ACS	F814W	1440
N300	9492	NGC300-6	ACS	F435W	1080
N300	9492	NGC300-6	ACS	F555W	1080
N300	9492	NGC300-6	ACS	F814W	1440
UA438	8192	E407-G18	WFPC2	F606W	600
UA438	8192	E407-G18	WFPC2	F814W	600
DDO187	10210	UGC9128	ACS	F606W	985
DDO187	10210	UGC9128	ACS	F814W	1174
KKH98	10915	KKH98	ACS	F475W	2265
KKH98	10915	KKH98	ACS	F814W	2280
DDO125/U7577	8601	UGC7577	WFPC2	F606W	600
DDO125/U7577	8601	UGC7577	WFPC2	F814W	600
U8508	10915	UGC8508	ACS	F475W	2280
U8508	10915	UGC8508	ACS	F814W	2349
KKH86	8601	KKH71	WFPC2	F606W	600
KKH86	8601	KKH71	WFPC2	F814W	600
DDO99/U6817	8601	UGC6817	WFPC2	F606W	600

Catalog Name DDO99/U6817	Proposal 8601 ID	Target Name UGC6817	Instrument WFPC2	Filter F814W	Exposure 600 Time (s)
DDO190/U9240	10915	DDO190	ACS	F475W	2274(s)
DDO190/U9240	10915	DDO190	ACS	F606W	2301
DDO190/U9240	10915	DDO190	ACS	F814W	2265
DDO113/KDG90	10915	DDO113	ACS	F475W	2265
DDO113/KDG90	10915	DDO113	ACS	F814W	2280
N4214	10915	NGC4214- DEEP	WFPC2	F606W	15600
N4214	10915	NGC4214- DEEP	WFPC2	F814W	31200
DDO181/U8651	10210	UGC8651	ACS	F606W	1016
DDO181/U8651	10210	UGC8651	ACS	F814W	1209
N3741	10915	NGC3741	ACS	F475W	2262
N3741	10915	NGC3741	ACS	F814W	2331
N4163	10915	NGC4163	ACS	F475W	2265
N4163	10915	NGC4163	ACS	F606W	2292
N4163	10915	NGC4163	ACS	F814W	2250
N4163	9771	NGC4163	ACS	F606W	1200
N4163	9771	NGC4163	ACS	F814W	900
N404	10915	NGC0404- DEEP	WFPC2	F606W	39000
N404	10915	NGC0404- DEEP	WFPC2	F814W	75400
UA292	10915	UGCA292	ACS	F475W	2250

UCAS Catalog Name	Proposal ID	UCAS Target Name	Instrument	Filter	Exposure Time (s)
UA292	10915	UGCA292	ACS	F814W	2274 (s)
U8833	10210	UGC8833	ACS	F606W	998
U8833	10210	UGC8833	ACS	F814W	1189
DDO183/U8760	10210	UGC8760	ACS	F606W	998
DDO183/U8760	10210	UGC8760	ACS	F814W	1189
N2366	10605	NGC-2366-1	ACS	F555W	4780
N2366	10605	NGC-2366-1	ACS	F814W	4780
N2366	10605	NGC-2366-2	ACS	F555W	4780
N2366	10605	NGC-2366-2	ACS	F814W	4780
DDO44/KK61	10915	DDO44	ACS	F475W	2361
DDO44/KK61	10915	DDO44	ACS	F814W	2430
DDO44/KK61	8137	DDO44	WFPC2	F555W	12800
DDO44/KK61	8137	DDO44	WFPC2	F814W	11900
DDO44/KK61	8192	KK061	WFPC2	F606W	600
DDO44/KK61	8192	KK061	WFPC2	F814W	600
E321-014	8601	PGC39032	WFPC2	F606W	600
E321-014	8601	PGC39032	WFPC2	F814W	600
U4483	8769	UGC4483	WFPC2	F555W	9500
U4483	8769	UGC4483	WFPC2	F814W	6900
N2403	10182	SN-NGC2403-PR	ACS	F475W	1200
N2403	10182	SN-NGC2403-PR	ACS	F606W	700

Catalog Name	Proposal ID	Target Name	Instrument	Filter	Exposure Time (s)
N2403	10182	SN-NGC2403-PR	ACS	F814W	700
N2403	10579	NGC2403-X1	ACS	F435W	1248
N2403	10579	NGC2403-X1	ACS	F606W	1248
N2403	10523	NGC2403-HALO-1	ACS	F606W	710
N2403	10523	NGC2403-HALO-1	ACS	F814W	710
N2403	10523	NGC2403-HALO-6	ACS	F606W	720
N2403	10523	NGC2403-HALO-6	ACS	F814W	720
N2403	10915	NGC2403-DEEP	WFPC2	F606W	32400
N2403	10915	NGC2403-DEEP	WFPC2	F814W	62100
DDO6	10915	DDO6	ACS	F475W	2250
DDO6	10915	DDO6	ACS	F814W	2268
HoIX/DDO66	10605	UGC-5336	ACS	F555W	4768
HoIX/DDO66	10605	UGC-5336	ACS	F814W	4768
HoI/DDO63	10605	UGC-5139	ACS	F555W	4446
HoI/DDO63	10605	UGC-5139	ACS	F814W	5936
KKH37/Mail6	10915	KKH37	ACS	F475W	2469
KKH37/Mail6	10915	KKH37	ACS	F814W	2541
KKH37/Mail6	9771	KKH37	ACS	F606W	1200

KKH37/Mail6 Catalog Name	9771 Proposal ID	KKH37 Target Name	ACS Instrument	F814W Filter	900 Exposure Time (s)
HoII/DDO50	10605	UGC-4305-1	ACS	F555W	4660
HoII/DDO50	10605	UGC-4305-1	ACS	F814W	4660
HoII/DDO50	10605	UGC-4305-2	ACS	F555W	4660
HoII/DDO50	10605	UGC-4305-2	ACS	F814W	4660
KDG2/E540-030	10503	ESO540-030	ACS	F606W	6720
KDG2/E540-030	10503	ESO540-030	ACS	F814W	6720
MCG9-20-131	10905	CGCG-269-049	WFPC2	F606W	2200
MCG9-20-131	10905	CGCG-269-049	WFPC2	F814W	2400
E540-032/FG24	10503	ESO540-032	ACS	F606W	8960
E540-032/FG24	10503	ESO540-032	ACS	F814W	4480
FM1	9884	M81F6D1	ACS	F606W	17200
FM1	9884	M81F6D1	ACS	F814W	9000
KK77	9884	M81F12D1	ACS	F606W	17200
KK77	9884	M81F12D1	ACS	F814W	9000
KDG63/KK83	9884	DDO71	ACS	F606W	17200
KDG63/KK83	9884	DDO71	ACS	F814W	9000
M82	10776	M82-POS1	ACS	F435W	1800
M82	10776	M82-POS1	ACS	F555W	1360
M82	10776	M82-POS1	ACS	F814W	700
M82	10776	M82-POS2	ACS	F435W	1800
M82	10776	M82-POS2	ACS	F555W	1360
M82	10776	M82-POS2	ACS	F814W	700

Catalog Name	Proposal ID	Target Name	Instrument	Filter	Exposure Time (s)
M82	10776	M82-POS3	ACS	F555W	1800
M82	10776	M82-POS3	ACS	F814W	700
M82	10776	M82-POS4	ACS	F435W	1800
M82	10776	M82-POS4	ACS	F555W	1360
M82	10776	M82-POS4	ACS	F814W	700
M82	10776	M82-POS5	ACS	F435W	1800
M82	10776	M82-POS5	ACS	F555W	1360
M82	10776	M82-POS5	ACS	F814W	700
M82	10776	M82-POS6	ACS	F435W	1800
M82	10776	M82-POS6	ACS	F555W	1360
M82	10776	M82-POS6	ACS	F814W	700
KDG52	10605	MESSIER-081-DWARF-A	ACS	F555W	5914
KDG52	10605	MESSIER-081-DWARF-A	ACS	F814W	5936
DDO53	10605	UGC-04459	ACS	F555W	4768
DDO53	10605	UGC-04459	ACS	F814W	4768
N2976	10915	NGC2976-DEEP	ACS	F475W	2418
N2976	10915	NGC2976-DEEP	ACS	F606W	18716
N2976	10915	NGC2976-DEEP	ACS	F814W	27091
N2976	10915	NGC2976-	ACS	F475W	1570

Catalog Name	Proposal ID	WIDE1 Target Name	Instrument	Filter	Exposure Time (s)
N2976	10915	NGC2976-WIDE1	ACS	F606W	1598 (s)
N2976	10915	NGC2976-WIDE1	ACS	F814W	1622
KDG61/KK81	9884	M81K61	ACS	F606W	17200
KDG61/KK81	9884	M81K61	ACS	F814W	9000
M81	10523	NGC3031-HALO-1	ACS	F606W	710
M81	10523	NGC3031-HALO-1	ACS	F814W	710
M81	10523	NGC3031-HALO-2	ACS	F606W	735
M81	10523	NGC3031-HALO-2	ACS	F814W	735
M81	9796	M81-X-9	ACS	F435W	2520
M81	9796	M81-X-9	ACS	F555W	1160
M81	9796	M81-X-9	ACS	F814W	1160
M81	10584	M81-FIELD-1	ACS	F435W	1565
M81	10584	M81-FIELD-1	ACS	F606W	1580
M81	10584	M81-FIELD-1	ACS	F814W	1595
M81	10584	M81-FIELD-2	ACS	F435W	1565
M81	10584	M81-FIELD-2	ACS	F606W	1580
M81	10584	M81-FIELD-2	ACS	F814W	1595
M81	10584	M81-FIELD-3	ACS	F435W	1200
M81	10584	M81-FIELD-3	ACS	F606W	1200

M81 Catalog Name	10584 Proposal	M81-FIELD-3 Target Name	ACS Instrument	F606W Filter	1200 Exposure Time (s)
M81	10584	M81-FIELD-4	ACS	F435W	1200
M81	10584	M81-FIELD-4	ACS	F606W	1200 ^(s)
M81	10584	M81-FIELD-5	ACS	F435W	1200
M81	10584	M81-FIELD-5	ACS	F606W	1200
M81	10584	M81-FIELD-6	ACS	F435W	1200
M81	10584	M81-FIELD-6	ACS	F606W	1200
M81	10584	M81-FIELD-7	ACS	F435W	1200
M81	10584	M81-FIELD-7	ACS	F606W	1200
M81	10584	M81-FIELD-8	ACS	F435W	1200
M81	10584	M81-FIELD-8	ACS	F606W	1200
M81	10584	M81-FIELD-9	ACS	F435W	1200
M81	10584	M81-FIELD-9	ACS	F606W	1200
M81	10584	M81-FIELD-10	ACS	F435W	1200
M81	10584	M81-FIELD-10	ACS	F606W	1200
M81	10584	M81-FIELD-11	ACS	F435W	1200
M81	10584	M81-FIELD-11	ACS	F606W	1200
M81	10584	M81-FIELD-12	ACS	F435W	1200
M81	10584	M81-FIELD-12	ACS	F606W	1200
M81	10584	M81-FIELD-13	ACS	F435W	1200
M81	10584	M81-FIELD-13	ACS	F606W	1200
M81	10584	M81-FIELD-14	ACS	F435W	1200
M81	10584	M81-FIELD-14	ACS	F606W	1200

M81 Catalog Name	10584 Proposal ID	M81-FIELD-15 Target Name	ACS Instrument	F435W Filter	1200 Exposure Time (s)
M81	10584	M81-FIELD-15	ACS	F606W	1200
M81	10584	M81-FIELD-16	ACS	F435W	1200
M81	10584	M81-FIELD-16	ACS	F606W	1200
M81	10584	M81-FIELD-17	ACS	F435W	1200
M81	10584	M81-FIELD-17	ACS	F606W	1200
M81	10584	M81-FIELD-18	ACS	F435W	1200
M81	10584	M81-FIELD-18	ACS	F606W	1200
M81	10584	M81-FIELD-19	ACS	F435W	1200
M81	10584	M81-FIELD-19	ACS	F606W	1200
M81	10584	M81-FIELD-20	ACS	F435W	1200
M81	10584	M81-FIELD-20	ACS	F606W	1200
M81	10584	M81-FIELD-21	ACS	F435W	1200
M81	10584	M81-FIELD-21	ACS	F606W	1200
M81	10584	M81-FIELD-22	ACS	F435W	1200
M81	10584	M81-FIELD-22	ACS	F606W	1200
M81	10584	M81-FIELD-23	ACS	F435W	1200
M81	10584	M81-FIELD-23	ACS	F606W	1200
M81	10584	M81-FIELD-24	ACS	F435W	1200
M81	10584	M81-FIELD-24	ACS	F606W	1200
M81	10584	M81-FIELD-25	ACS	F435W	1200
M81	10584	M81-FIELD-25	ACS	F606W	1200
M81	10584	M81-FIELD-26	ACS	F435W	1200

M81 Catalog Name	10584 Proposal ID	M81-FIELD-26 Target Name	ACS Instrument	F606W Filter	1200 Exposure Time (s)
M81	10584	M81-FIELD-27	ACS	F435W	1565
M81	10584	M81-FIELD-27	ACS	F606W	1580
M81	10584	M81-FIELD-27	ACS	F814W	1595
M81	10584	M81-FIELD-28	ACS	F435W	1565
M81	10584	M81-FIELD-28	ACS	F606W	1580
M81	10584	M81-FIELD-28	ACS	F814W	1595
M81	10584	M81-FIELD-29	ACS	F435W	1565
M81	10584	M81-FIELD-29	ACS	F606W	1580
M81	10584	M81-FIELD-29	ACS	F814W	1595
M81	10915	M81-DEEP	ACS	F475W	2418
M81	10915	M81-DEEP	ACS	F606W	24132
M81	10915	M81-DEEP	ACS	F814W	29853
N247	10915	NGC0247- WIDE1	ACS	F475W	2253
N247	10915	NGC0247- WIDE1	ACS	F606W	2280
N247	10915	NGC0247- WIDE1	ACS	F814W	2250
N247	10915	NGC0247- WIDE2	ACS	F475W	1480
N247	10915	NGC0247- WIDE2	ACS	F606W	1507
N247	10915	NGC0247- WIDE2	ACS	F814W	1534
N247	10915	NGC0247- WIDE2	ACS	F475W	1480

N247 Catalog Name	10915 Proposal ID	NGC0247- Target Name WIDE3	ACS Instrument	F475W Filter	1480 Exposure Time (s)
N247	10915	NGC0247- WIDE3	ACS	F606W	150(s)
N247	10915	NGC0247- WIDE3	ACS	F814W	1534
HoIX/DDO66	10605	UGC-5336	ACS	F555W	4768
HoIX/DDO66	10605	UGC-5336	ACS	F814W	4768
KDG64/KK85	9884	M81K64	ACS	F606W	17200
KDG64/KK85	9884	M81K64	ACS	F814W	9000
IKN	9771	IKN	ACS	F606W	1200
IKN	9771	IKN	ACS	F814W	900
KDG73	10915	KDG73	ACS	F475W	2250
KDG73	10915	KDG73	ACS	F814W	2274
DDO78/KK89	10915	DDO78	ACS	F475W	2274
DDO78/KK89	10915	DDO78	ACS	F814W	2292
F8D1	5898	GAL- 094447+672619	WFPC2	F555W	9000
F8D1	5898	GAL- 094447+672619	WFPC2	F814W	15200
F8D1	5898	GAL- 094447+672619	WFPC2	F555W	9000
F8D1	5898	GAL- 094447+672619	WFPC2	F814W	11400
BK5N	5898	GAL- 100441+681522	WFPC2	F555W	5400

BK5N Catalog Name	5898 Proposal ID	GAL- Target Name 100441+681522	WFPC2 Instrument	F814W Filter	11400 Exposure Time (s)
BK5N	6964	GAL- 100441+681522	WFPC2	F555W	15600 ^(s)
BK5N	6964	GAL- 100441+681522	WFPC2	F814W	21340
N3077	9381	NGC3077- PHOENIX	ACS	F435W	6000
N3077	9381	NGC3077- PHOENIX	ACS	F555W	9600
N3077	9381	NGC3077- PHOENIX	ACS	F814W	19200
N3077	10915	NGC3077- WIDE1	ACS	F475W	1570
N3077	10915	NGC3077- WIDE1	ACS	F606W	1596
N3077	10915	NGC3077- WIDE1	ACS	F814W	1622
HoII/DDO50	10605	UGC-4305-1	ACS	F555W	4660
HoII/DDO50	10605	UGC-4305-1	ACS	F814W	4660
HoII/DDO50	10605	UGC-4305-2	ACS	F555W	4660
HoII/DDO50	10605	UGC-4305-2	ACS	F814W	4660
HoIX/DDO66	10605	UGC-5336	ACS	F555W	4768
HoIX/DDO66	10605	UGC-5336	ACS	F814W	4768
HoI/DDO63	10605	UGC-5139	ACS	F555W	4446
HoI/DDO63	10605	UGC-5139	ACS	F814W	5936
Δ0052+60	10915	Δ0052+60	ACS	F475W	2250

Catalog Name	Proposal	Target Name	Instrument	Filter	Exposure Time (s)
A0952+69	10915	A0952+69	ACS	F814W	2265
N253	10915	NGC0253- WIDE1	ACS	F475W	2256 ^(s)
N253	10915	NGC0253- WIDE1	ACS	F606W	2283
N253	10915	NGC0253- WIDE1	ACS	F814W	2253
N253	10915	NGC0253- WIDE2	ACS	F475W	1482
N253	10915	NGC0253- WIDE2	ACS	F606W	1508
N253	10915	NGC0253- WIDE2	ACS	F814W	1534
N253	10915	NGC0253- WIDE3	ACS	F475W	1482
N253	10915	NGC0253- WIDE3	ACS	F606W	1508
N253	10915	NGC0253- WIDE3	ACS	F814W	1534
N253	10915	NGC0253- WIDE4	ACS	F475W	1482
N253	10915	NGC0253- WIDE4	ACS	F606W	1508
N253	10915	NGC0253- WIDE4	ACS	F814W	1534
N253	10915	NGC0253- WIDE5	ACS	F475W	1482

Catalog Name	Proposal ID	Target Name	Instrument	Filter	Exposure Time (s)
N253	10915	NGC0253- WIDE5	ACS	F814W	1534 ^(s)
N253	10523	NGC0253- HALO-11	ACS	F606W	680
N253	10523	NGC0253- HALO-11	ACS	F814W	680
HS117	9771	HS117	ACS	F606W	1200
HS117	9771	HS117	ACS	F814W	900
DDO82	10915	DDO82	ACS	F475W	2400
DDO82	10915	DDO82	ACS	F606W	2454
DDO82	10915	DDO82	ACS	F814W	2442
BK3N	10915	BK3N	ACS	F475W	2250
BK3N	10915	BK3N	ACS	F814W	2265
I2574	10605	IC-2574-1- COPY	ACS	F555W	4784
I2574	10605	IC-2574-1- COPY	ACS	F814W	4784
I2574	10605	IC-2574-2	ACS	F555W	4784
I2574	10605	IC-2574-2	ACS	F814W	4784
I2574	9755	IC2574-SGS	ACS	F435W	6000
I2574	9755	IC2574-SGS	ACS	F555W	6400
I2574	9755	IC2574-SGS	ACS	F814W	6400
Sc22	10503	SCL-DE1	ACS	F606W	17920

Sc22 Catalog Name	10503 Proposal	SCL-DE1 Target Name	ACS Instrument	F814W Filter	17920 Exposure
ID					Time (s)
<p>Notes. Exposure times may differ from those in Table 3 when individual fields were unusable.</p>					
Download table as:					
<input type="button" value="ASCII"/> Typeset images: <input type="button" value="1"/> <input type="button" value="2"/> <input type="button" value="3"/> <input type="button" value="4"/> <input type="button" value="5"/> <input type="button" value="6"/>					

While these cuts do an excellent job of restricting the catalogs to stellar sources, we have noted occasional limits to star-galaxy separation near the photometric limits of the data, and spurious "stellar" sources in the diffraction spikes of extremely bright stars. If these issues are of critical importance for a particular scientific project, we recommend additional culling using information from galaxy-specific photometry packages such as SExtractor (Bertin & Arnouts [1996](#)) to mask out possible sources of contamination.

We also note that star-galaxy separation is frequently impossible for sources near the photometric limit, even in high-resolution *HST* data. Some fraction of the faintest sources in the photometric catalogs are therefore likely to be unresolved background galaxies. We do not think that these sources are a significant issue for most analyses, however, since they represent a negligible fraction of the sources in the main body of most galaxies. To quantify this, we can use the WFPC2 field for IC5152. This field has a completeness limit of 26.45 mag in F814W and contains 325 objects in the cleaned *.gst catalog (described below), over an area of 5.65 arcmin². The field unfortunately fell beyond the radius where IC5152's disk truncates, and thus the majority of the 325 objects are likely to be either foreground MW stars or unresolved background galaxies. We can then take 57.5 stars per

square arcminute to be the upper limit for the contamination in observations of this depth.

We can scale the IC5152 data to other completeness limits, using the observed galaxy number counts given in Figure 3(b) of Windhorst et al. (2008). Over the range of depths for the ANGST data, the slope in the galaxy number counts scales as $\log_{10}(N_1/N_2) \approx 0.32(m_{lim,1} - m_{lim,2})$. We have applied this scaling relation to the data in Table 4 to calculate the upper limit on the fraction of sources that could potentially be contaminants in each field. After IC5152 itself (which has 100% contamination by definition), the next highest contamination fraction is 35% for an outer halo field of M81 (NGC3031-HALO-2), which lies well beyond the main body of the galaxy. All other contamination fractions are less than 23%, and 90% have maximum contamination fractions of less than 10%. Given that most ANGST targets take up less than one third of the total chip area, the contribution of unresolved galaxies to the CMD is likely to be less than 3% within the galaxy radius in almost all cases.

7. WFPC2 PHOTOMETRY

After the failure of ACS and the transfer of our program to WFPC2, we adopted the WFPC2 pipeline previously used by Holtzman et al. (2006) for their archival study of Local Group dwarfs. We briefly summarize the key features of the pipeline here, but refer the interested reader to the more extensive documentation in Holtzman et al. (2006).

The Holtzman et al. (2006) pipeline operates on images processed with the standard STScI baseline processing. Photometry is performed using HSTphot (Dolphin 2000), a predecessor of DOLPHOT that is optimized for WFPC2 images. HSTphot shares DOLPHOT's basic strategy of using Tiny Tim PSFs supplemented with image-based aperture corrections to derive photometry from unstacked images that

have not been distortion corrected or drizzled. HSTphot adopts the photometric calibration given in Holtzman et al. (1995), updated with improved calibrations from http://purcell.as.arizona.edu/wfpc2_calib/. Note that the WFPC2 photometric system is defined such that Vega has a magnitude in each WFPC2 filter corresponding to Vega's magnitude in the nearest UBVRI filter; the different definition of the zero points in the WFPC2 and ACS photometric systems leads to offsets of 0.02–0.04 mag between the calibrated magnitudes of the two instruments (see Section 8.2).

The only significant difference from the Holtzman et al. (2006) pipeline is that the current version of HSTphot uses the latest (2008 July) CTE corrections derived by A. Dolphin (http://purcell.as.arizona.edu/wfpc2_calib/). Compared to the Dolphin et al. (2002) prescription, the new CTE calibration no longer assumes that background and stellar brightness factors are independent, leading to somewhat fainter WFPC2 magnitudes than previous calibrations, and many fewer systemic offsets in the residuals. Using a typical ANGST wide field observation as a baseline, the switch to the new CTE correction changes the CTE correction for a $V=22$ mag star from 0.052 mag to 0.115 mag in F606W and from 0.067 mag to 0.123 mag in F814W, for a background sky level of ~ 100 counts pixel⁻¹ in both filters. For a fainter $V=28$ mag star, the CTE changes from 0.328 mag to 0.214 mag in F606W and from 0.438 mag to 0.238 mag in F814W. The much lower level of residuals in the new CTE calibration suggests accuracy in the bright end of 0.01–0.02 mag. At the fainter end, it is much more difficult to assess any systematic offsets, as they are much smaller than the photometric uncertainties.

After processing by the Holtzman et al. (2006) pipeline, we integrate the photometry into the database shared by the main ACS pipeline. Slight differences in the WFPC2 and ACS keywords used the released

data tables are described below in Section [10](#).

8. PHOTOMETRIC TESTS

The photometric pipeline produces catalogs of multi-filter photometry and estimates of the photometric uncertainty for each measurement. These uncertainties include Poisson flux errors, uncertainties in the sky determination, and uncertainties in the subtraction of neighboring objects. They do not include systematic errors due to spatial and temporal variation of the PSF (i.e., Jee et al. [2007](#); Rhodes et al. [2006](#); ACS ISR 07-12, ACS-ISR 06-01), in the absolute calibration of the photometric system, and in the accuracy of the adopted CTE corrections (which were in flux at the time that this data was released). To assess the degree of systematic errors, and the accuracy of the reported uncertainties, we have performed a series of consistency checks to measure shifts in the photometry of individual stars measured multiple times, in different portions of the FOV, and for different instruments. All tests use the conservative photometric catalogs, to allow the greatest sensitivity to systematic errors.

8.1. Repeated ACS Measurements

We first analyze the magnitude difference between stars measured in two individual single-orbit F814W ACS exposures from the M81 deep field. The exposures were taken during a single visit, which minimizes any temporal changes in the PSF. The exposures also had only modest ($0\farcs1-0\farcs2$) dithers between them, allowing us to minimize systematic errors in modeling the spatial variations in the PSF. Crowding errors should likewise be minimal, given the low stellar density within the field. This test case therefore offers the "best case scenario" for agreement between repeated measurements, and sets a lower bound to our expected error distribution in less than optimal cases.

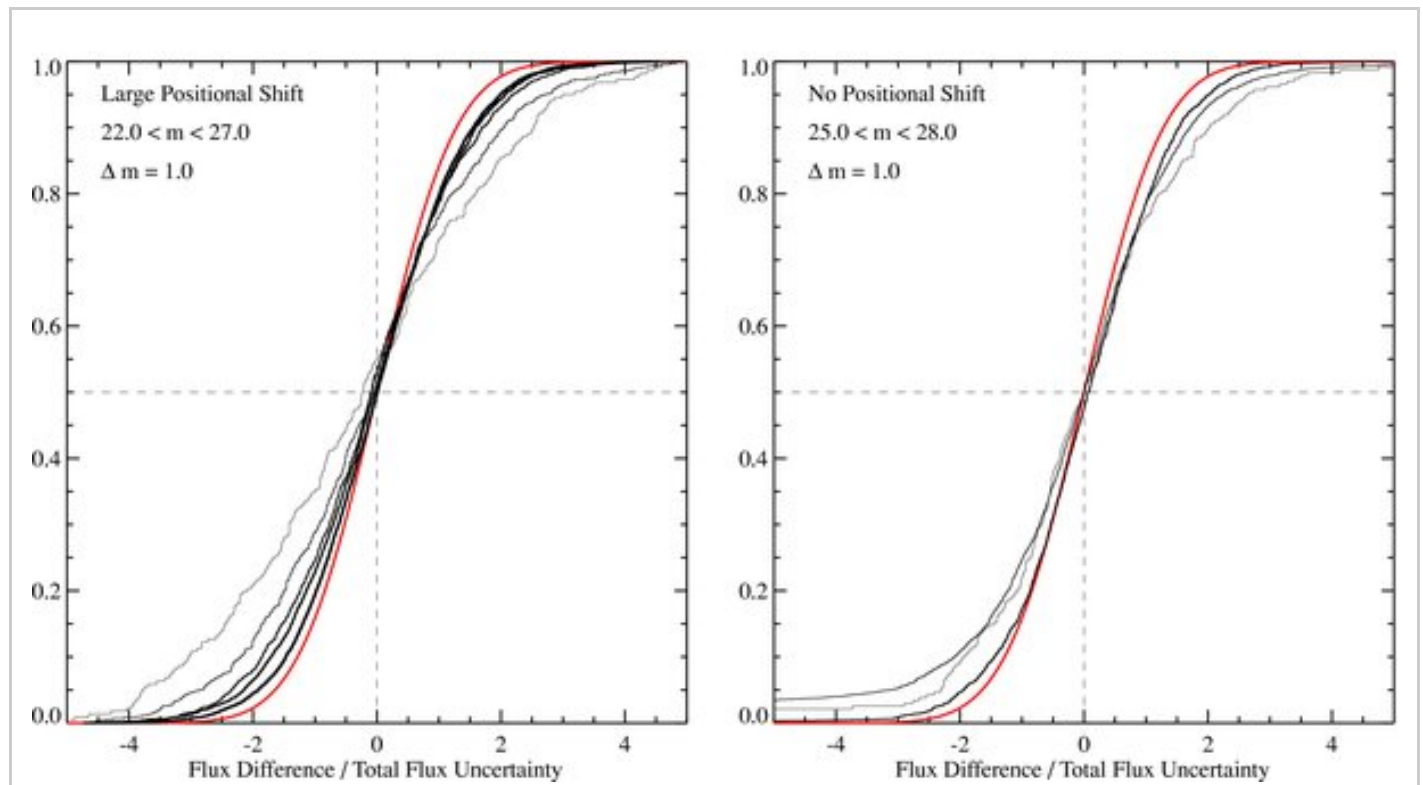
To measure magnitude differences closer to the "worst-case scenario"

for ACS, we also analyze repeated measurements of stars that fall in the overlap region in the wide field tiling of NGC 300, between WIDE1 and WIDE2. These stars lie in the most highly distorted regions of the ACS chip, and have close to the maximum possible offset in their locations on the chips between the two images, making them a highly sensitive test of the uncertainties produced by errors in the PSF that DOLPHOT adopts from Tiny Tim. The images were also taken two days apart in separate visits, making them somewhat sensitive to temporal changes in the PSF as well. However, as there was little change in the Y-position of the stars, this comparison has no sensitivity to systematic errors produced by CTE.

Finally, we measure the magnitude differences between the measured and the "true" magnitudes of artificial stars, added to the same overlap region analyzed above for NGC 300. In this case, the stars are recovered with a PSF that is identical to that used for generating the artificial stars. This case therefore minimizes effects due to PSF uncertainty. However, it remains sensitive to errors due to Poisson variations in the flux and the sky background, and due to contamination from nearby stars. Note that the error distributions are expected to be different from the previous two tests, which probed magnitude differences between repeated measurements of stars with identical crowding and sky backgrounds, not the magnitude differences from truth.

In Figure 7, we plot the cumulative distribution of magnitude differences between repeated measurements of individual stars, scaled by the quadrature sum of the uncertainties reported in the individual measurements (i.e., $\Delta m / \Delta m$ where $\Delta m = m_1 - m_2$ and $\Delta m^2 = \Delta m_1^2 + \Delta m_2^2$ and m_1 and m_2 refer to the measurements of a single star in two different images). The distributions are generated for all stars in a limited magnitude range, in steps of 1 mag, with fainter bins plotted with darker lines. The distributions for brighter stars have insufficient

numbers of stars to be reliable, and are not plotted. In red, we plot the distribution of scaled magnitude differences that would be expected if the magnitude differences were distributed as a Gaussian with width σ_m . The left panel contains only stars in the overlap region (~600 pixels wide), and the right panel contains stars for the whole frame.



[Zoom In](#) [Zoom Out](#)

[Reset image size](#)

Figure 7. Cumulative distribution of F814W magnitude differences between stars measured in two widely separated but overlapping ACS exposures between NGC 300's WIDE1 and WIDE2 (left), and between stars measured in successive one-orbit ACS exposures at the same pointing in M81's deep field (right).

Magnitude differences are scaled by the reported magnitude error for each star, added in quadrature for the case of repeat measurements. The distributions are calculated in bins of 1 mag, with the heaviest line indicating the faintest bin. The red curve indicates the expectation for a perfect Gaussian error distribution. In both cases, the distribution of errors is only slightly broader than a Gaussian, and systematic errors are covered by photometric

Gaussian, and systematic errors are swamped by photometric uncertainties.

Download figure:

 [Standard image](#)

 [High-resolution image](#)

 [Export PowerPoint slide](#)

The distributions of magnitude differences between repeated measurements show a number of features. First, even in the worst case scenario of large positional shifts, the magnitude differences are essentially unbiased. The median magnitude difference is less than 5% of the reported uncertainty in all cases, such that repeated measurements of given isochrone features will converge on the same magnitude, even when observed with different parts of chip, or with multiple exposures. There is a slight tendency, however, for the bias to be somewhat larger when large positional shifts are present, particularly for the brighter stars. This indicates that there are indeed small systematic errors in the assumed PSF that are more noticeable when the wings of the PSF are well exposed. However, these biases will be swamped by the intrinsic random and crowding errors, as well as Poisson uncertainties, and thus can safely be neglected in almost all practical applications.

The second feature of the distributions is their tendency to be wider than a Gaussian whose width is set by the reported uncertainties. The true distributions are broader and more flat-topped than expected. This leads to larger numbers of stars at a given magnitude difference than one would predict for a perfect Gaussian error distribution. This difference is most pronounced for the brightest stars. However, even the largest shifts do not produce measurable tails beyond $5\sigma_{mb}$, so while the shape of the error distribution differs from a Gaussian, we do not

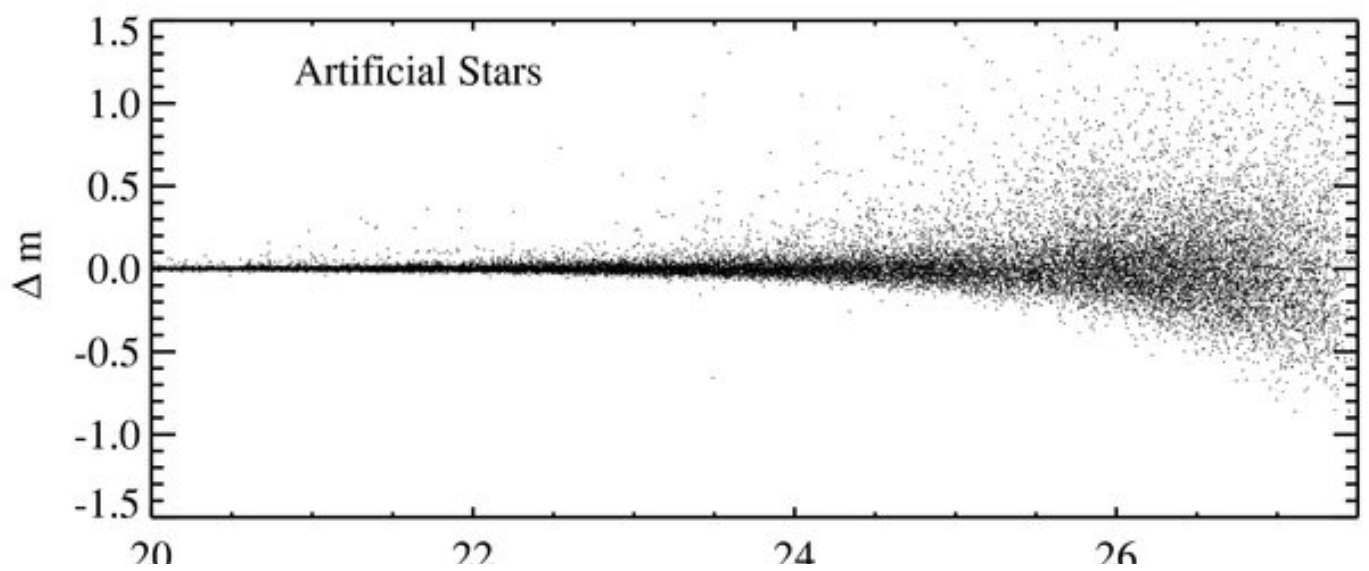
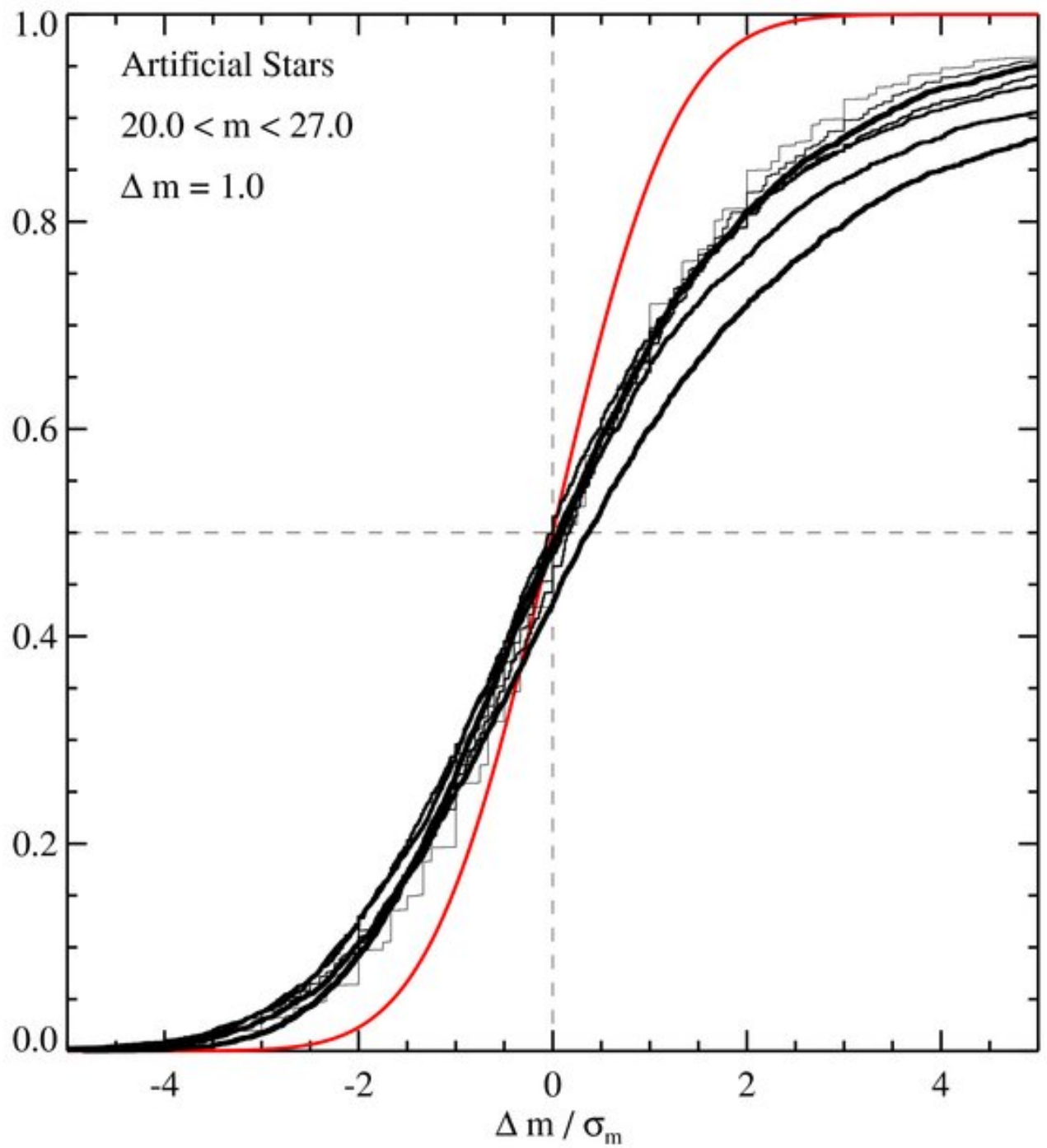
detect more than 1–2 stars with $\Delta m > 5 \Delta m$ in our analysis regions.

We can get clues to the origin of the increased width by noting that the discrepancy from a Gaussian is larger for brighter stars, for which the distribution becomes closer to a uniform "top hat." We believe that a significant fraction of this broadening is actually due to the limited precision of the errors and magnitudes reported by DOLPHOT.

Catalog values of Δm and Δm are quantized at the 0.001 mag level, rather than being true continuous variables. This quantization has the largest impact on the distribution of $\Delta m / \Delta m$ when errors and magnitude differences are close to the level of quantization, as they are for the brightest stars. Not until the faintest magnitude bins do the errors approach the distribution expected for a continuous variable.

In Figure 8 we show the distribution of magnitude differences between the true and the measured magnitudes ($\Delta m = m_{\text{true}} - m_{\text{measured}}$, and $\Delta m / \Delta m_{\text{measured}}$) of artificial stars added to and recovered from the images, for a series of magnitude bins. These distributions are quite different than the distributions for repeated measurements, as would be expected. First, the distributions are highly skewed, producing a large tail toward measured magnitudes that are brighter than the true magnitude. This skewing results when artificial stars land on or near a star that would otherwise be undetected. The flux from the previously undetected star adds to the artificial star, biasing the measured flux upward. Such a bias would not be apparent in a repeated measurement, as both measurements would share the same bias. The skewing is most severe for the faintest stars, where the additional flux from undetected stars produces the largest fractional change in the detected flux. Moreover, the sample of faint recovered stars will be biased toward stars with heavily contaminated fluxes, given that such stars are preferentially detected; this effect is reduced for brighter stars, which are detectable whether or not an undetected companion falls

within the PSF.



 [Zoom In](#)  [Zoom Out](#)

 [Reset image size](#)

Figure 8. Cumulative distribution of F814W magnitude differences between the true and recovered magnitudes in artificial stars from the same overlap region from NGC 300's WIDE1. The top panel shows the cumulative distribution of magnitude differences, scaled by the reported magnitude error for each star, added in quadrature for the case of repeat measurements. The distributions are calculated in bins of 1 mag wide, with the heaviest line indicating the faintest bin. The red curve indicates the expectation for a perfect Gaussian error distribution. The bottom panel shows the measured magnitude differences as a function of magnitude. Recovered magnitudes tend to be somewhat brighter than true magnitudes due to blending with fainter unresolved sources.

Download figure:

 [Standard image](#)

 [High-resolution image](#)

 [Export PowerPoint slide](#)

The second feature apparent in the comparison between true and measured magnitudes is that the distributions are systematically broader than a Gaussian with a standard deviation equal to the magnitude uncertainty reported for the measured star. This deviation is not surprising, given that the uncertainties are not due solely to Poisson counting statistics, and are thus unlikely to have distributions that approach a perfect Gaussian.

8.2. WFPC2-ACS Comparison

Due to the failure of ACS, we are releasing photometry both from WFPC2 and ACS. Differences between these two photometric systems are expected due to different instrumental responses, CTE corrections, and absolute photometric calibrations between the two photometric systems. We have made an initial assessment of the degree of possible systematic offsets using observations of the dwarf elliptical DDO 44, which was observed with WFPC2 (GO-8137) in January of 2001, and with ACS as part of ANGST in September of 2006. Both data sets were processed with the respective WFPC2 and ACS pipelines described above. Stars were automatically matched between the two catalogs using the closest positional match in right ascension and declination, after solving for shifts and rotation between the two fields. We consider only pairs of stars that agreed in magnitude to within $10\sigma_m$, where σ_m is the magnitude error from the quadrature sum of the error in each pair of stars; this procedure produced good matches for $\approx 90\%$ of the overlapping stars, though there are clearly occasional spurious matches as well. The resulting matched catalog was restricted further to include only stars above the approximate completeness limit of each data set (m_{F814W} brighter than 26.0 and 26.1 for the WFPC2 and ACS data sets, respectively). Comparisons were made in the F814W filter, which is the only overlapping filter between the two sets of observations.

Before comparing $m_{F814W,WFPC2}$ to $m_{F814W,ACS}$, we need to account for the different zero-point definitions in the ACS and WFPC2 photometric systems. Both systems are relative to Vega, but the ACS system defines Vega to have 0 mag in all ACS filters, while the WFPC2 system defines Vega to have a magnitude corresponding to Vega's magnitude in the nearest UBVRI filter. For F814W, Vega has $m_{F814W,WFPC2} = 0.035$. As a result, 0.035 mag must be added to the ACS F814W photometry to compare the results on the same system.²² The systems will also differ for stars of a different color than Vega to the

extent that the system response of the ACS F814W filter+camera+detector system differs from that of WFPC2.

We examined the resulting magnitude differences as a function of magnitude, color, and Y-position on the chip. At almost all magnitude levels, the systematic errors are dominated by the random errors in the photometry (which themselves are dominated by Poisson counting variations and residual flux from crowding). However, we do detect residual systematic errors at the few percent level, which vary steadily with Y on either instrument, indicating low level problems with the adopted CTE corrections in both WFPC2 and ACS. Updated CTE corrections for ACS are in progress at STScI, but these corrections were not ready in time for reducing the data for this release. Given that these corrections are typically swamped by random errors and are smaller than current uncertainties in the stellar isochrones that are used to interpret the CMDs, we decided to release the data as is. Subsequent releases will include the new CTE corrections as they become available. We also detected possible signs of a color-dependence in the magnitude differences between the WFPC2 and ACS F814W VEGAMAGS, which appear to be larger than expected based on synthetic filter curves. A definitive diagnosis of this dependence must wait until the improved CTE corrections for ACS are implemented, but should the effect persist, then there may be an additional few percent uncertainty in the instrumental response of either WFPC2 or ACS or both.

9. ASTROMETRY

Astrometry for the photometric catalogs was initially taken from the FITS headers of the original HST images, which have astrometry that is accurate to 1 – 2". Recently, the Hubble Legacy Archive (HLA) improved on the default astrometry using the Guide Star Catalog (GSC), the SDSS, and the 2MASS. The revised astrometric solutions have a typical

rms of $0.1 - 0.3$ in most cases. There are many cases in our data set where the rms is much larger, due to using faint (or non-existent) sources in the GSC, or cosmic rays in the image during matching. In these cases, new astrometric positions will have to be derived by hand. Because this process is almost always limited by the lack of astrometric standards within nearby galaxies, in many cases $1'' - 2''$ uncertainties remain, and will have to be dealt with in future releases by using a system of secondary astrometric standards defined in wide-field ground-based imaging.

Relative photometry within a given field is usually accurate to a fraction of a pixel, and the absolute position is good to a few pixels in most cases. However, in applications requiring subarcsecond accuracy of the absolute astrometric position (e.g., such as slit masks or comparisons with multi-wavelength data), users should consider making an independent astrometric solution. We will continue to release improved astrometric solutions as they become available, including time-dependent geometric distortion corrections as well.

10. DATA PRODUCTS

Binary FITS tables of photometry for the ANGST sample have been released through the Multimission Archive at STScI (MAST: <http://archive.stsci.edu/prepds/angst/>), and can also be accessed interactively through the project Web site (<http://www.nearbygalaxies.org>). File names and field names were taken from the image headers and are of the format PROPOSID-TARGNAME, where PROPOSID is the value of the header keyword "PROPOSID" and TARGNAME is the value of the header keyword "TARGNAME." The naming conventions and column names for the files are summarized below, and are contained in the headers of the fits files themselves.

*.param: DOLPHOT parameter files: These files provide the parameters used by DOLPHOT when measuring the photometry, and are useful for interpreting the columns in the raw photometry files. These files are currently only available on the project Web site.

*.phot: Raw photometry files: These large ASCII files contain the raw output from DOLPHOT. Descriptions of the columns can be found in the DOLPHOT manual (<http://purcell.as.arizona.edu/dolphot/>). The listing of individual columns can be found on the project Web site.

*.st.fits: Star files: these files contain the photometry of all objects classified as stars (object type ≤ 2) with $S/N > 4$ and data flag < 8 . Compared to the *.gst files described below, these files will contain more objects and have higher completeness in crowded regions, at the expense of producing less well defined CMDs with more potential contamination from background galaxies. Columns are X, Y, RA, DEC, MAG1_ACS (or MAG1_WFPC2 in WFPC2 files), MAG1_STD, MAG1_ERR, CHI1, SHARP1, CROWD1, SNR1, FLAG1 (or CHIP in WFPC2 files), MAG2_ACS (or MAG2_WFPC2 in WFPC2 files), MAG2_STD, MAG2_ERR, CHI2, SHARP2, CROWD2, SNR2, FLAG2 (or FLAG in WFPC2 files). These values are defined as follows. X and Y positions are relative to positions on the drizzled reference image. The MAG1 and MAG2 values refer to the filters given in the file name and in the FITS header. ACS magnitudes are VEGAMAGs, which are calibrated by setting the zero point of each filter so that the magnitude of Vega is 0.0 (Sirianni et al. [2005](#)). WFPC2 magnitudes are VEGAMAGs, which are calibrated by setting the zero point of each filter so that the magnitude of Vega is 0.035 in most ANGST filters (Holtzman et al. [1995](#)). STD magnitudes have been converted from VEGAMAGs to standard Johnson–Cousins magnitudes for the nearest Johnson–Cousins filter (B , V , or I) using the transformation equations of Sirianni et al. ([2005](#); ACS) and Holtzman et al. ([1995](#); WFPC2). The DOLPHOT CHI value indicates the goodness of the PSF fit, with values

of <1.5 - 2.5 being reasonable for uncrowded well-exposed stars, and values of up to 4 - 5 being expected for either blended but unresolved stars, or for stars in crowded regions. The SHARP parameter indicates the deviation from a perfect PSF profile, with positive values indicating profiles that are too sharp (such as cosmic rays), and negative values indicating profiles that are too broad (such as unresolved blends, clusters, or background galaxies). The SNR value gives the signal-to-noise with which the star was detected. The CROWD parameter is in magnitudes, and indicates how much brighter the star would have been if flux from nearby stars had not been subtracted. FLAG1 and FLAG2 are the DOLPHOT quality flags for each filter as described in the manual. FLAG is the Holtzman et al. ([2006](#)) quality flag used in the Local Group Stellar Populations Archive. Further details can be found in the DOLPHOT manual.

*.gst.fits: "Good" star files: These files contain the stars that pass the conservative ANGST quality cuts for sharpness and crowding ($\text{sharp}_1 + \text{sharp}_2 \geq 0.075$ and $\text{crowd}_1 + \text{crowd}_2 \geq 0.1$), in addition to the S/N and flag criteria. Columns and header information are the same as for the *.st.fits files.

The field names, number of stars, and 50% completeness limits can be found in Table [4](#).

The MAST archive for ANGST also includes copies of the reference images to which all X - Y positions are tied. For ACS, the reference image is a single dithered image in the deepest filter. For WFPC2, there are four reference images, one for each chip on the camera.

11. COLOR-MAGNITUDE DIAGRAMS

In Figures [9](#)-[22](#) we present CMDs for all of the fields listed in Tables [2](#) and [3](#). The plotted photometry is drawn from the high-quality (*.gst.fits)

catalogs. As described above, these quality cuts produce the most well-defined features in the CMD, at the expense of completeness in high-crowding regions (such as the densest stellar clusters). In regions of high stellar density on the CMD, data are plotted as contoured Hess diagrams, with contours drawn at levels of 1, 1.5, 2, 2.5, 3, 4, 6, 8, 12, 16, 20×10^4 stars mag^{-2} . Characteristic photometric uncertainties are shown with error bars on the left side of the CMDs in Figures 9–22.

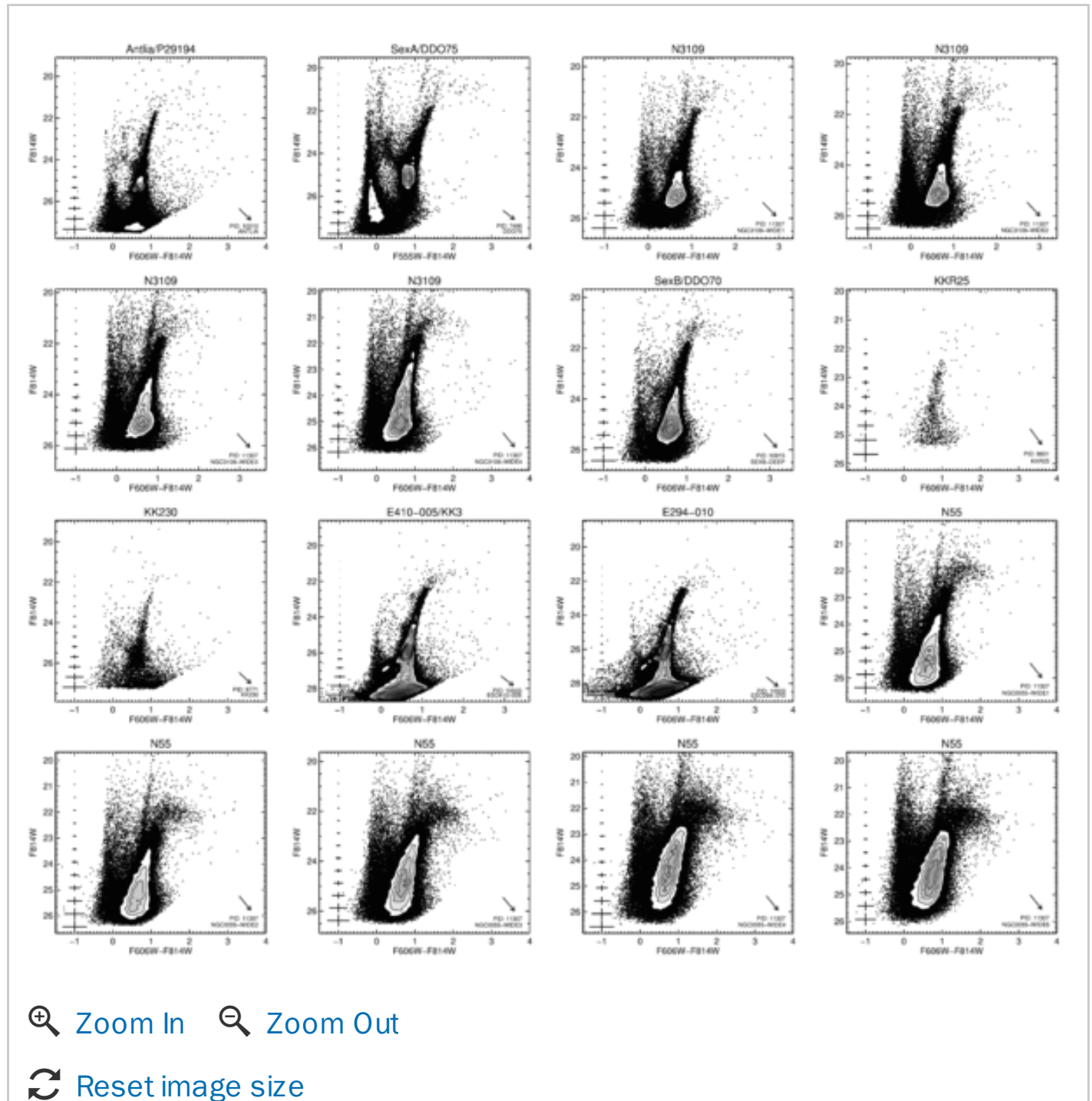


Figure 9. CMDs of galaxies in the ANGST data release (Tables 2 and 3), using photometry from the conservative *_gst catalogs. Stars are plotted as individual points in regions of the CMD with few stars

are plotted as individual points in regions of the CMD with few stars, and are plotted as a Hess diagram otherwise. The lower right of each plot shows the HST proposal ID and target name, and an arrow indicating the direction of the reddening vector. The ANGST/CNG Catalog name is given at the top of each plot. Error bars on the left indicate typical photometric errors in each magnitude bin, but do not include systematic errors derived from artificial star tests.

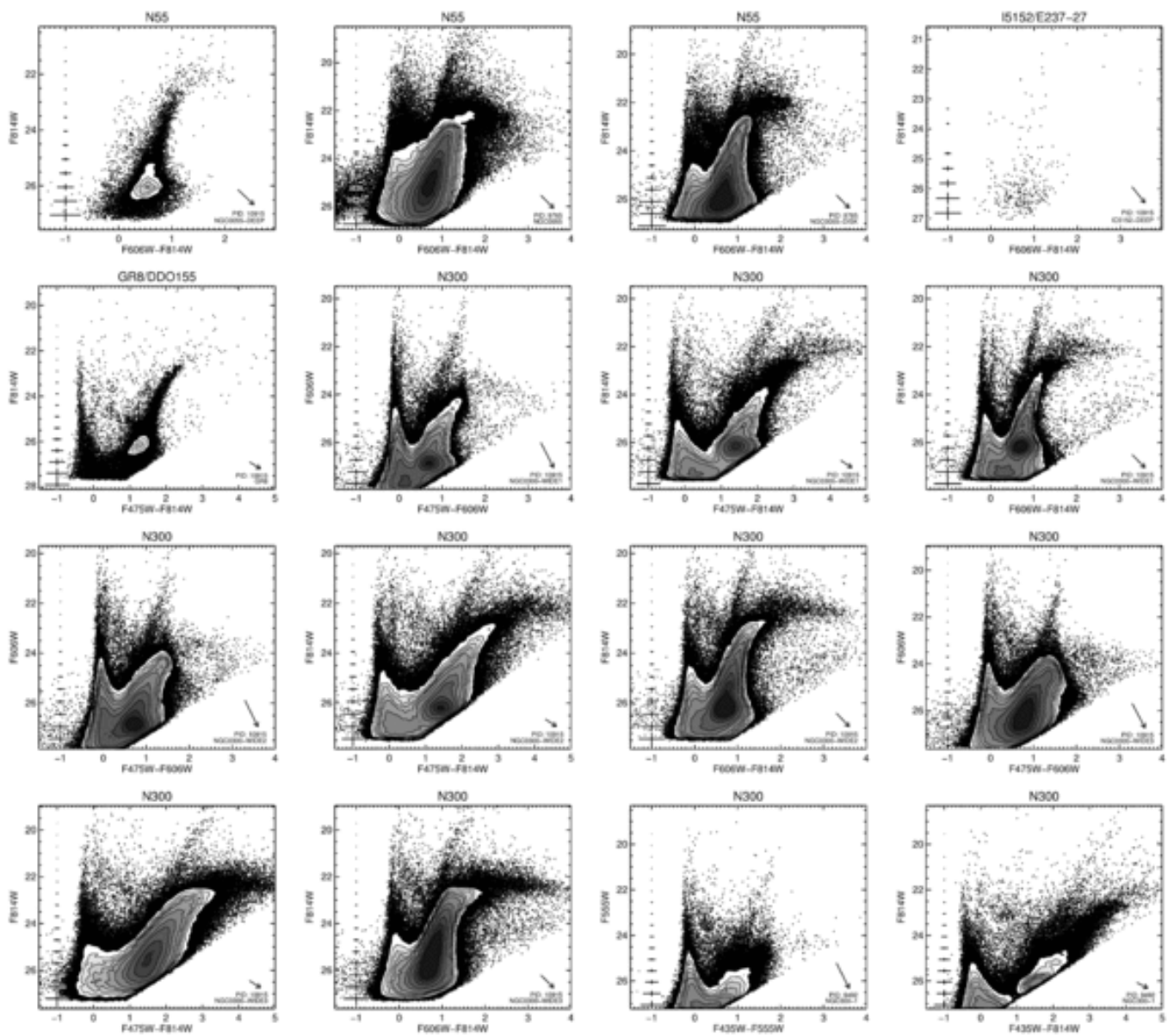
Galaxies are ordered as in Table [1](#). Some fields have multiple CMDs, showing all possible filter combinations on the color axis (e.g., F475W – F606W, F475W – F814W, F606W – F814W). Figures are ordered from the upper left to the bottom right. (a) Antlia; (b) SexA; (c) N3109; (d) N3109; (e) N3109; (f) N3109; (g) SexB; (h) KKR25; (i) KK230; (j) E410-005; (k) E294-010; (l) N55; (m) N55; (n) N55; (o) N55; (p) N55.

Download figure:

 [Standard image](#)

 [High-resolution image](#)

 [Export PowerPoint slide](#)



[🔍 Zoom In](#) [🔍 Zoom Out](#)

[🔄 Reset image size](#)

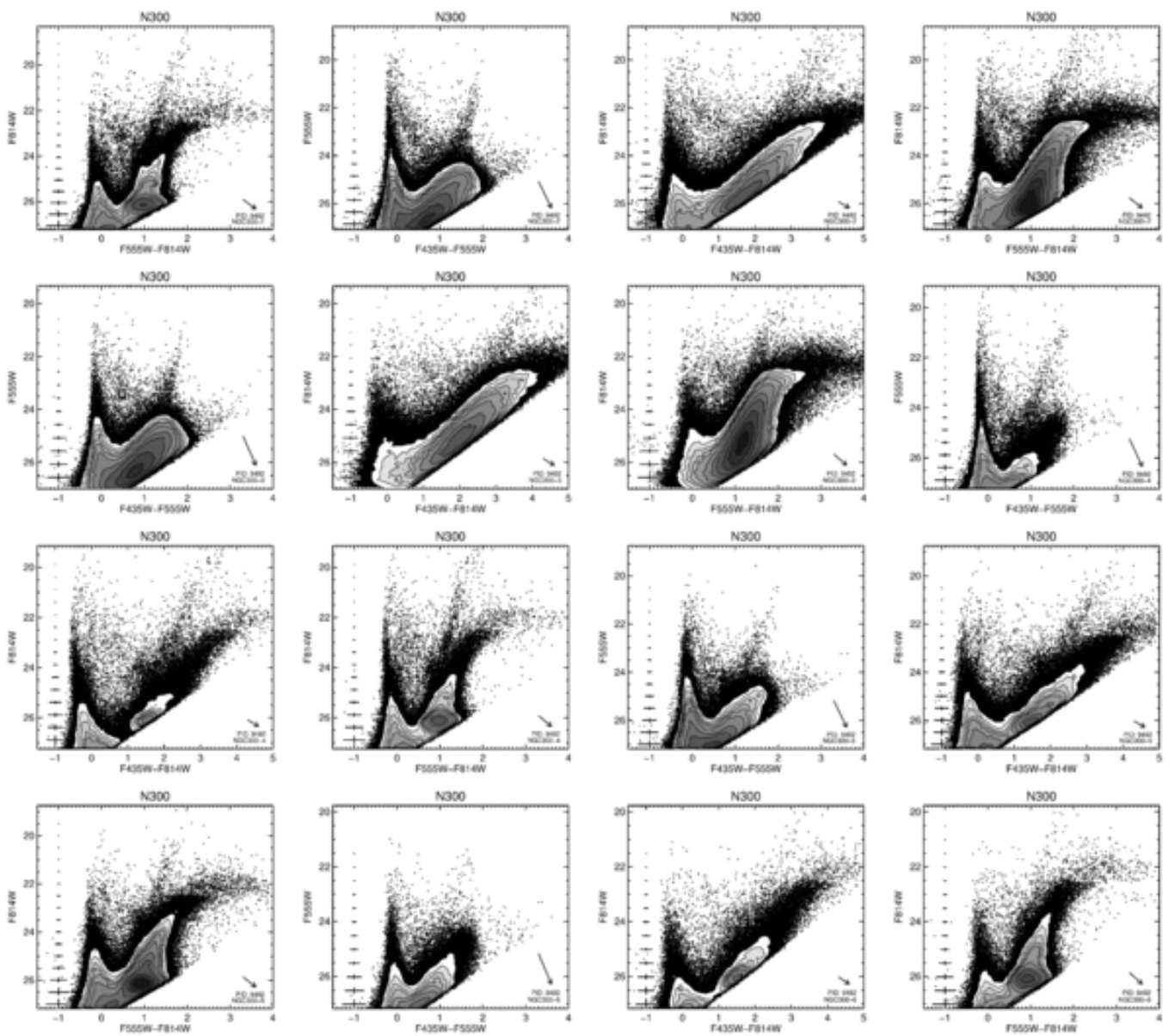
Figure 10. CMDs of galaxies in the ANGST data release, as described in Figure 9. Figures are ordered from the upper left to the bottom right. (a) N55; (b) N55; (c) N55; (d) I5152; (e) GR8; (f) N300; (g) N300; (h) N300; (i) N300; (j) N300; (k) N300; (l) N300; (m) N300; (n) N300; (o) N300; (p) N300.

Download figure:

[🖼️ Standard image](#)

[🖼️ High-resolution image](#)

[📄 Export PowerPoint slide](#)



[Zoom In](#) [Zoom Out](#)

[Reset image size](#)

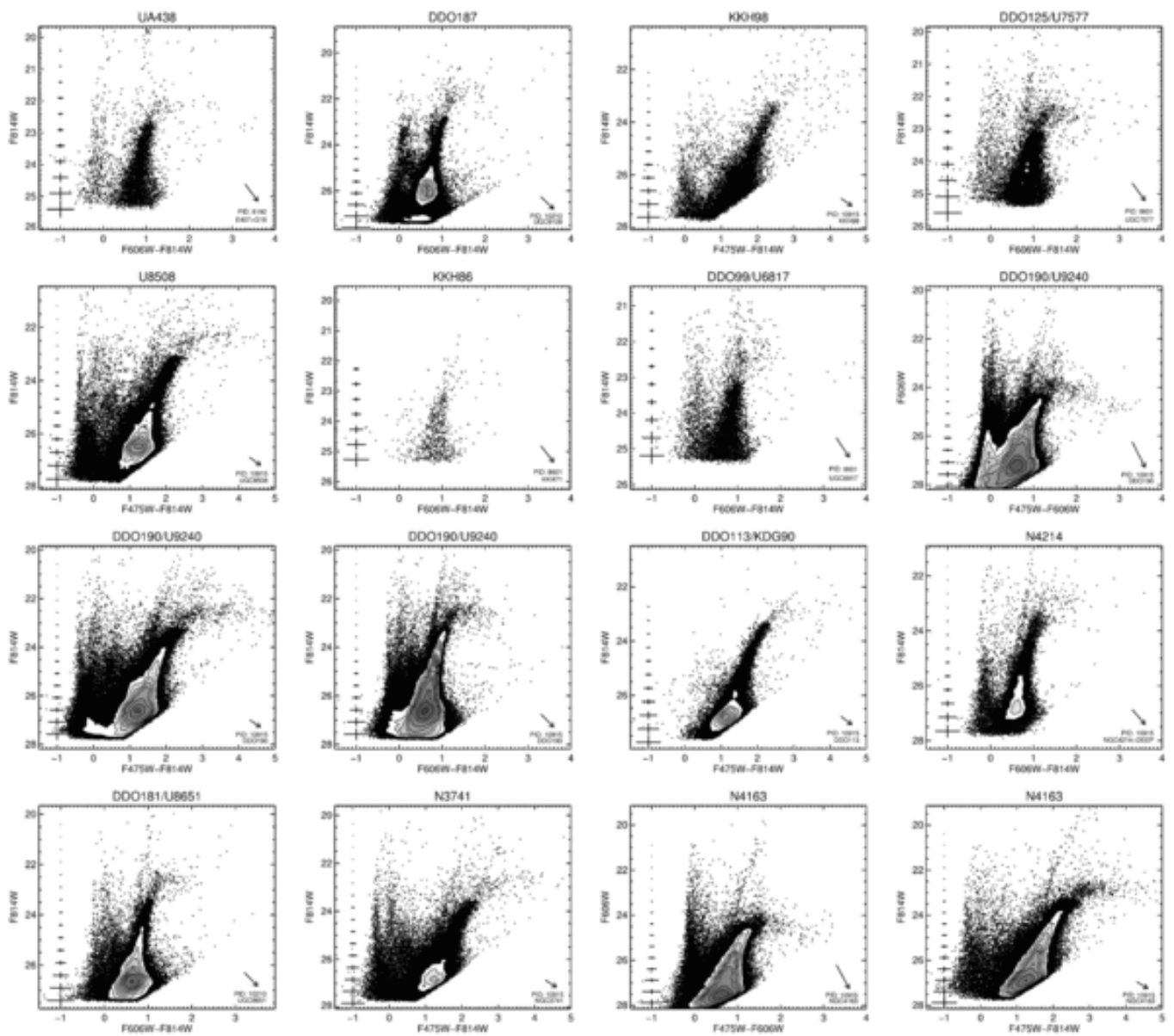
Figure 11. CMDs of galaxies in the ANGST data release, as described in Figure 9. Figures are ordered from the upper left to the bottom right. (a) N300; (b) N300; (c) N300; (d) N300; (e) N300; (f) N300; (g) N300; (h) N300; (i) N300; (j) N300; (k) N300; (l) N300; (m) N300; (n) N300; (o) N300; (p) N300.

Download figure:

[Standard image](#)

[High-resolution image](#)

[Export PowerPoint slide](#)



[🔍 Zoom In](#) [🔍 Zoom Out](#)

[🔄 Reset image size](#)

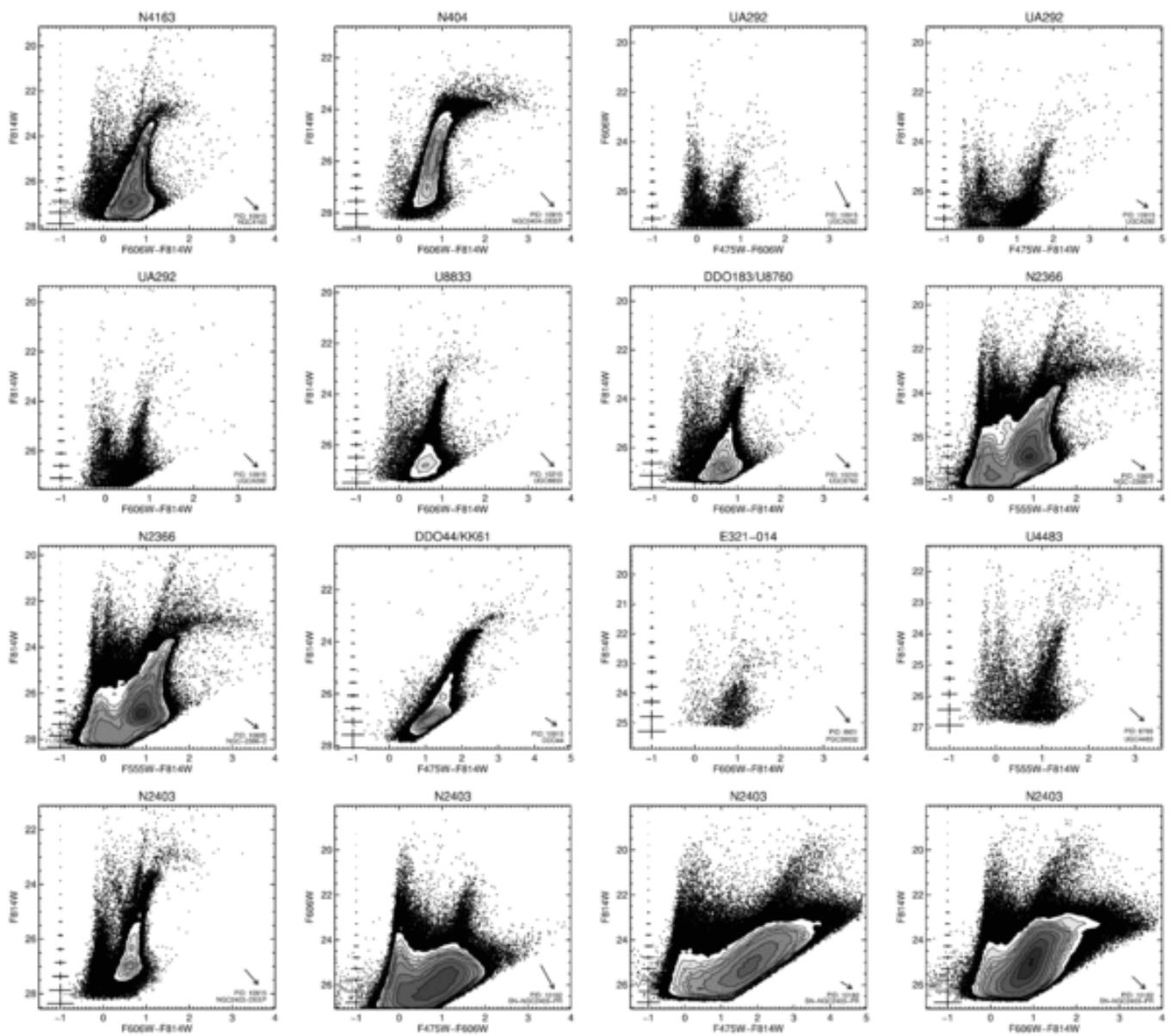
Figure 12. CMDs of galaxies in the ANGST data release, as described in Figure 9. Figures are ordered from the upper left to the bottom right. (a) UA438; (b) DDO187; (c) KKH98; (d) DDO125; (e) U8508; (f) KKH86; (g) DDO99; (h) DDO190; (i) DDO190; (j) DDO190; (k) DDO113; (l) N4214; (m) DDO181; (n) N3741; (o) N4163; (p) N4163.

Download figure:

[🖼️ Standard image](#)

[🖼️ High-resolution image](#)

[📄 Export PowerPoint slide](#)



[🔍 Zoom In](#) [🔍 Zoom Out](#)

[🔄 Reset image size](#)

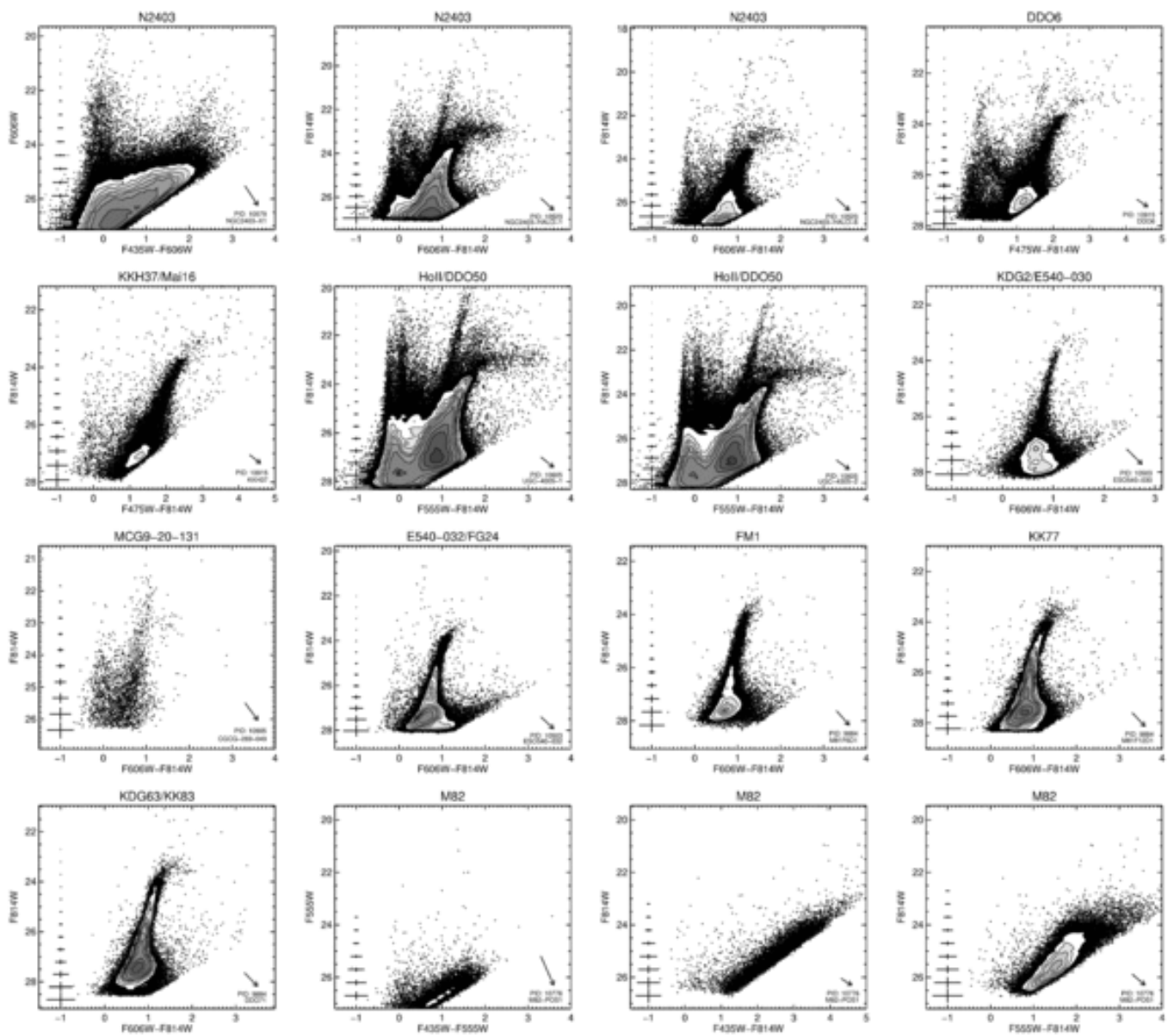
Figure 13. CMDs of galaxies in the ANGST data release, as described in Figure 9. Figures are ordered from the upper left to the bottom right. (a) N4163; (b) N404; (c) UA292; (d) UA292; (e) UA292; (f) U8833; (g) DDO183; (h) N2366; (i) N2366; (j) DDO44; (k) E321-014; (l) U4483; (m) N2403; (n) N2403; (o) N2403; (p) N2403.

Download figure:

[🖼️ Standard image](#)

[🖼️ High-resolution image](#)

[📄 Export PowerPoint slide](#)



[Zoom In](#) [Zoom Out](#)

[Reset image size](#)

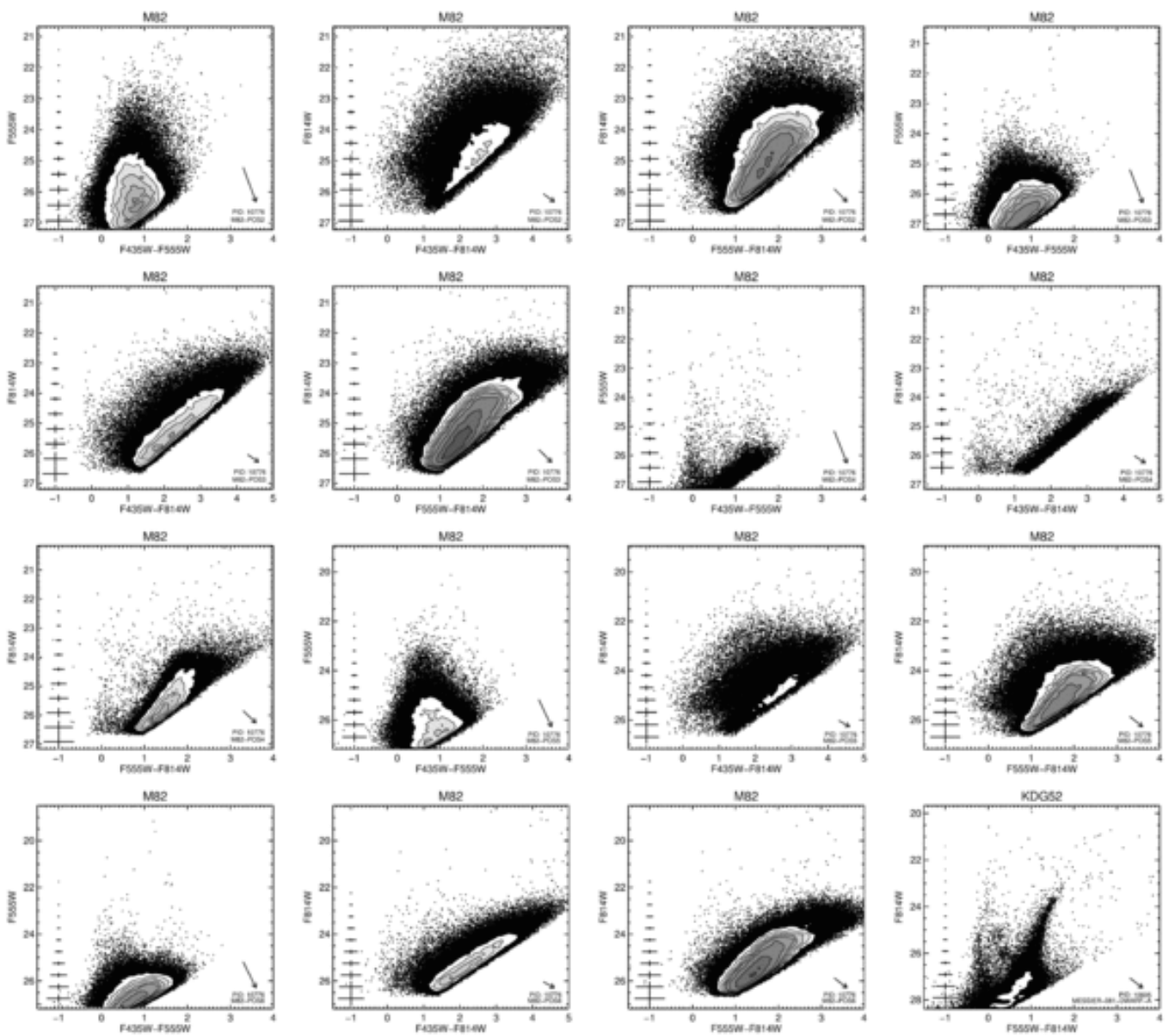
Figure 14. CMDs of galaxies in the ANGST data release, as described in Figure 9. Figures are ordered from the upper left to the bottom right. (a) N2403; (b) N2403; (c) N2403; (d) DDO6; (e) KKH37; (f) HoII; (g) HoII; (h) KDG2; (i) MCG9-20-131; (j) E540-032; (k) FM1; (l) KK77; (m) KDG63; (n) M82; (o) M82; (p) M82.

Download figure:

[Standard image](#)

[High-resolution image](#)

[Export PowerPoint slide](#)



[Zoom In](#) [Zoom Out](#)

[Reset image size](#)

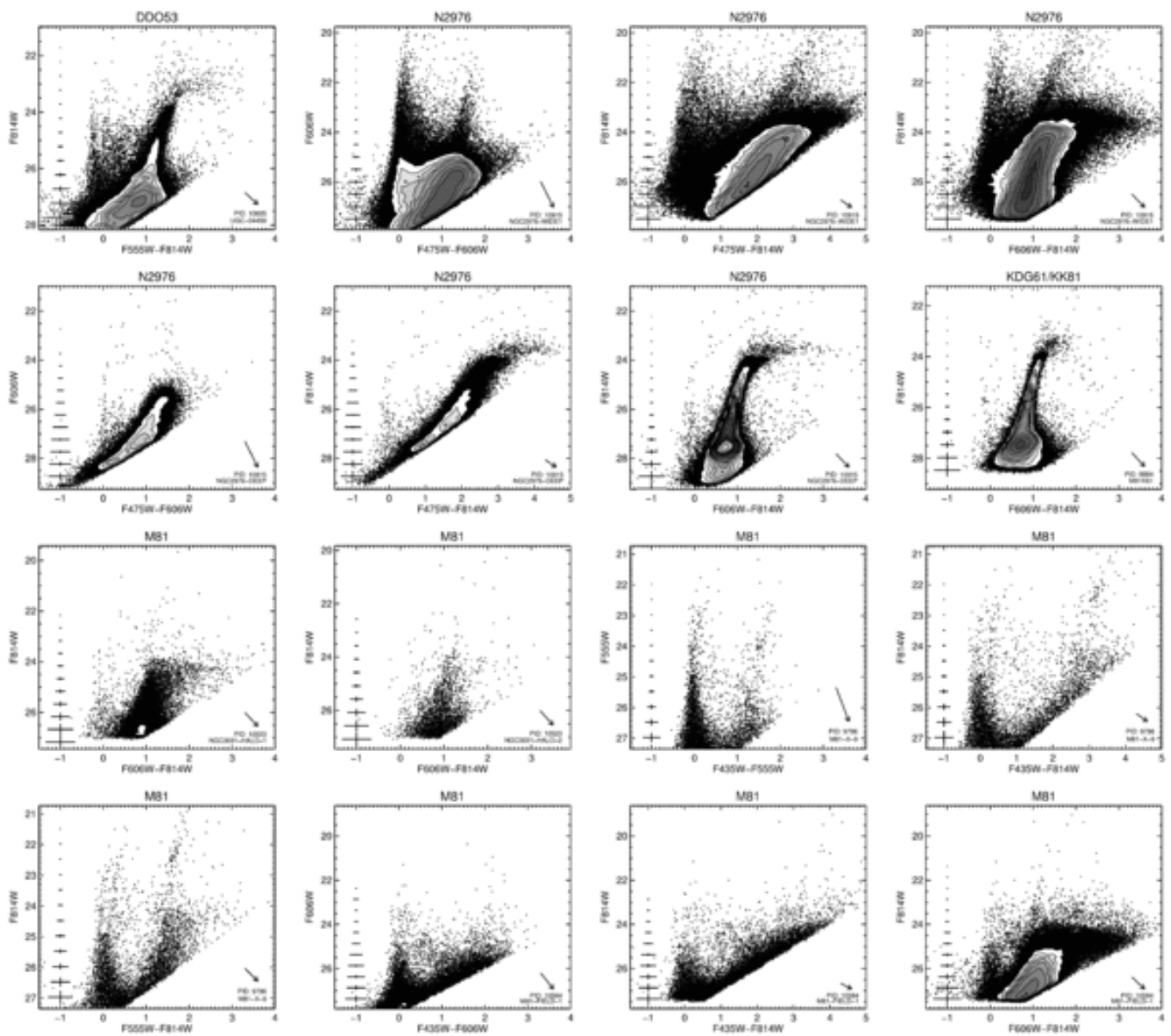
Figure 15. CMDs of galaxies in the ANGST data release, as described in Figure 9. Figures are ordered from the upper left to the bottom right. (a) M82; (b) M82; (c) M82; (d) M82; (e) M82; (f) M82; (g) M82; (h) M82; (i) M82; (j) M82; (k) M82; (l) M82; (m) M82; (n) M82; (o) M82; (p) KDG52.

Download figure:

[Standard image](#)

[High-resolution image](#)

[Export PowerPoint slide](#)



[Zoom In](#) [Zoom Out](#)

[Reset image size](#)

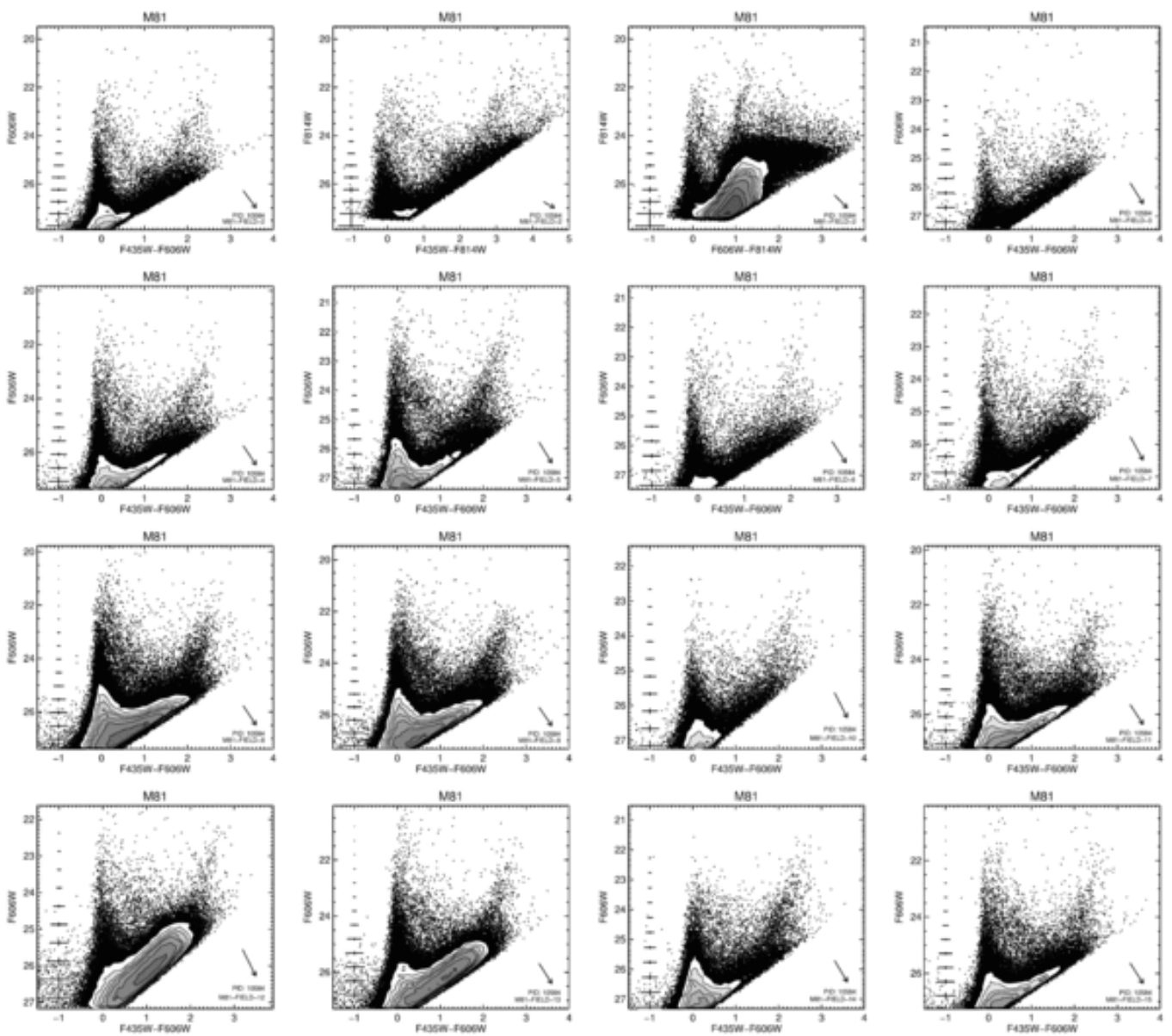
Figure 16. CMDs of galaxies in the ANGST data release, as described in Figure 9. Figures are ordered from the upper left to the bottom right. (a) DDO53; (b) N2976; (c) N2976; (d) N2976; (e) N2976; (f) N2976; (g) N2976; (h) KDG61; (i) M81; (j) M81; (k) M81; (l) M81; (m) M81; (n) M81; (o) M81; (p) M81.

Download figure:

[Standard image](#)

[High-resolution image](#)

[Export PowerPoint slide](#)



 [Zoom In](#)  [Zoom Out](#)

 [Reset image size](#)

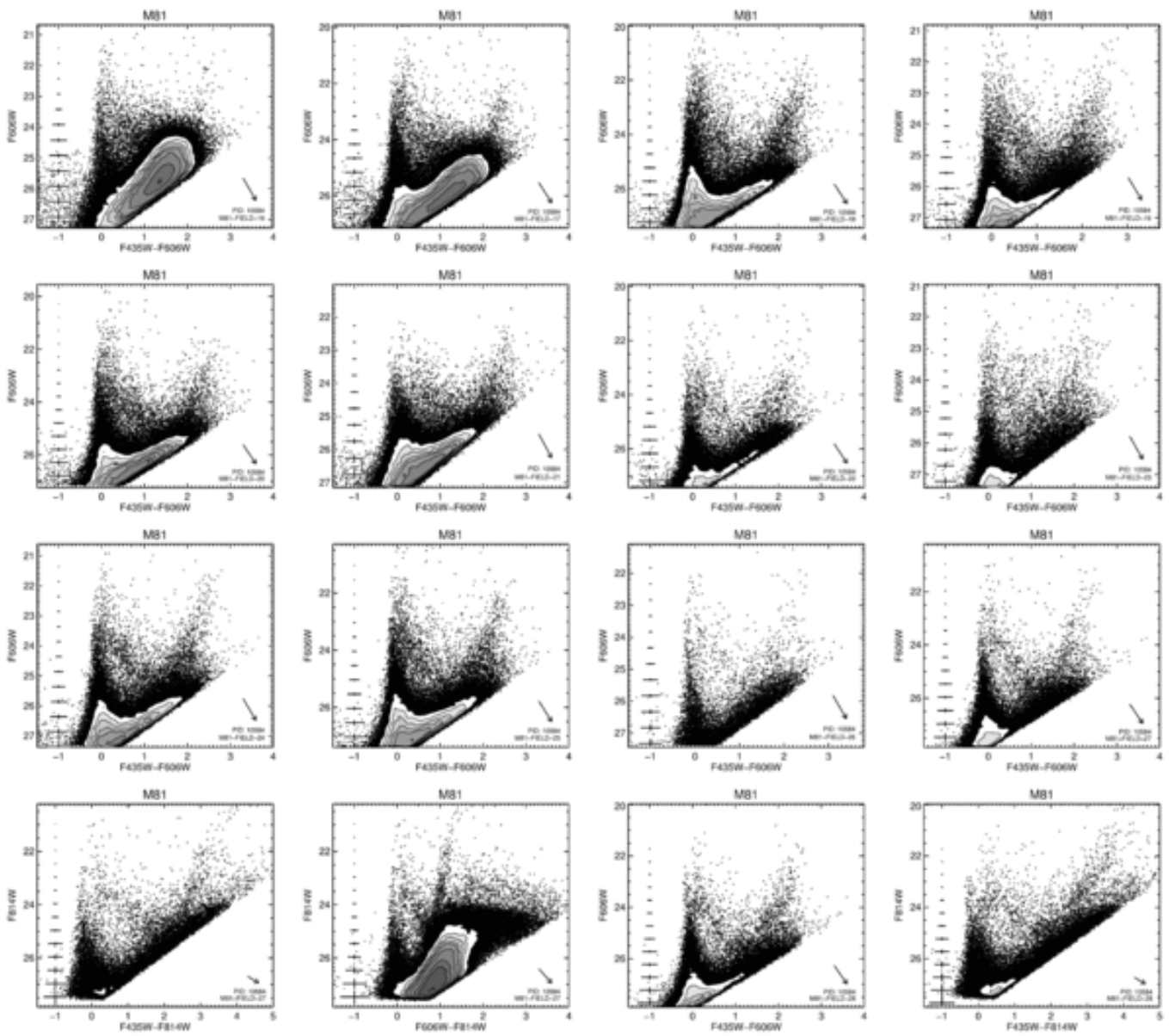
Figure 17. CMDs of galaxies in the ANGST data release, as described in Figure 9. Figures are ordered from the upper left to the bottom right. (a) M81; (b) M81; (c) M81; (d) M81; (e) M81; (f) M81; (g) M81; (h) M81; (i) M81; (j) M81; (k) M81; (l) M81; (m) M81; (n) M81; (o) M81; (p) M81.

Download figure:

 [Standard image](#)

 [High-resolution image](#)

 [Export PowerPoint slide](#)



[Zoom In](#) [Zoom Out](#)

[Reset image size](#)

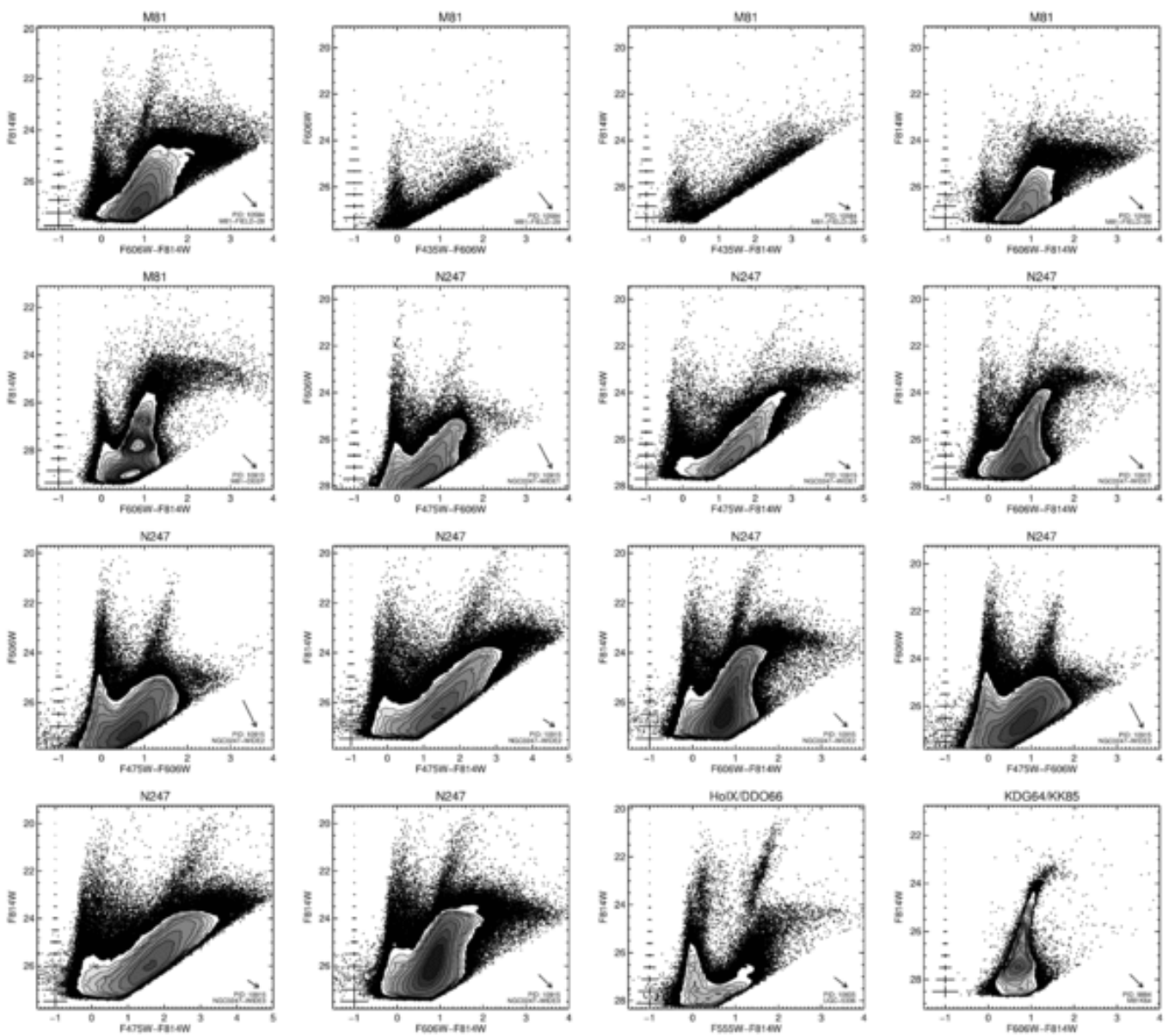
Figure 18. CMDs of galaxies in the ANGST data release, as described in Figure 9. Figures are ordered from the upper left to the bottom right. (a) M81; (b) M81; (c) M81; (d) M81; (e) M81; (f) M81; (g) M81; (h) M81; (i) M81; (j) M81; (k) M81; (l) M81; (m) M81; (n) M81; (o) M81; (p) M81.

Download figure:

[Standard image](#)

[High-resolution image](#)

[Export PowerPoint slide](#)



[🔍 Zoom In](#) [🔍 Zoom Out](#)

[🔄 Reset image size](#)

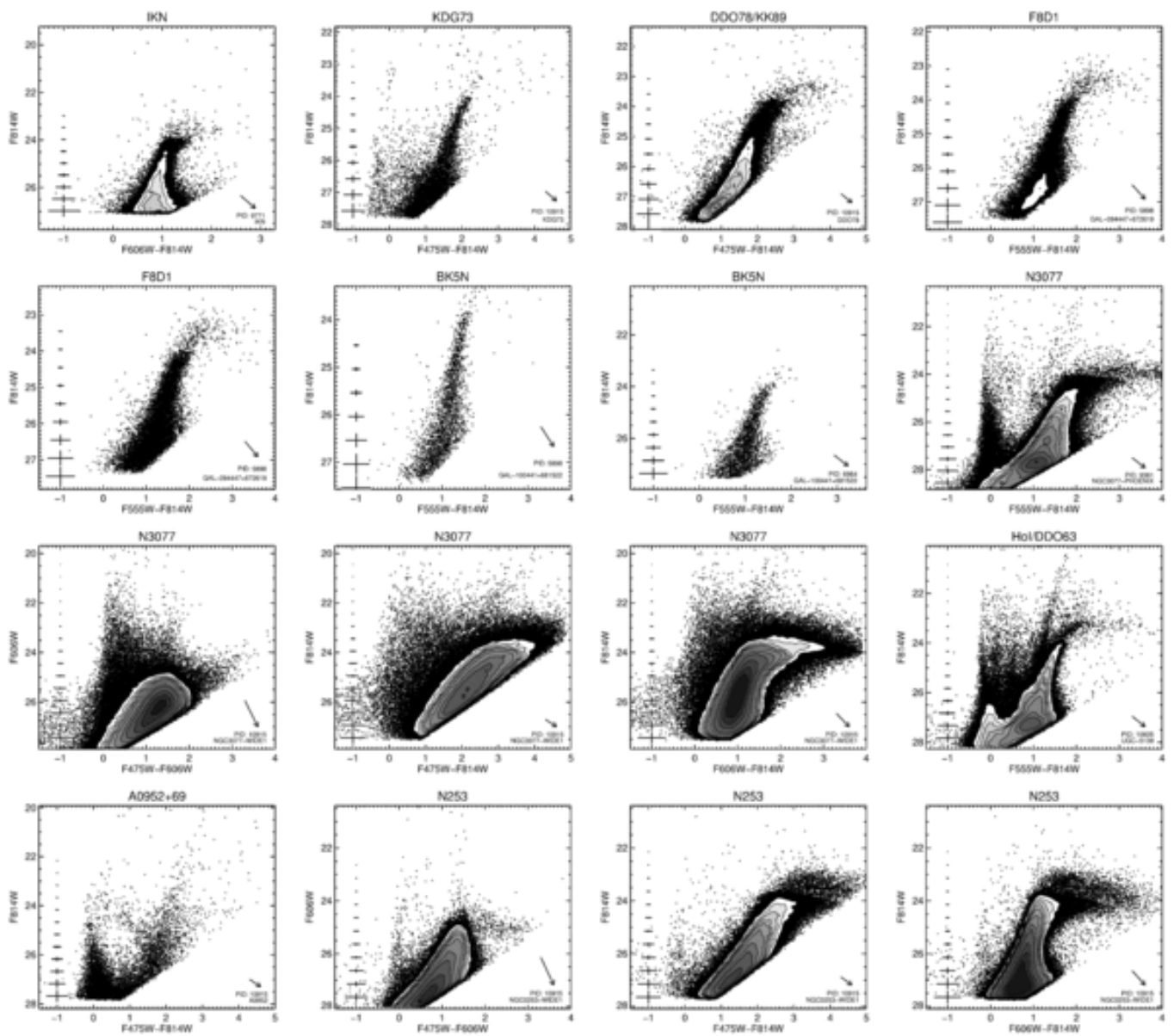
Figure 19. CMDs of galaxies in the ANGST data release, as described in Figure 9. Figures are ordered from the upper left to the bottom right. (a) M81; (b) M81; (c) M81; (d) M81; (e) M81; (f) N247; (g) N247; (h) N247; (i) N247; (j) N247; (k) N247; (l) N247; (m) N247; (n) N247; (o) HoIX; (p) KDG64.

Download figure:

[🖼️ Standard image](#)

[🖼️ High-resolution image](#)

[📄 Export PowerPoint slide](#)



 [Zoom In](#)  [Zoom Out](#)

 [Reset image size](#)

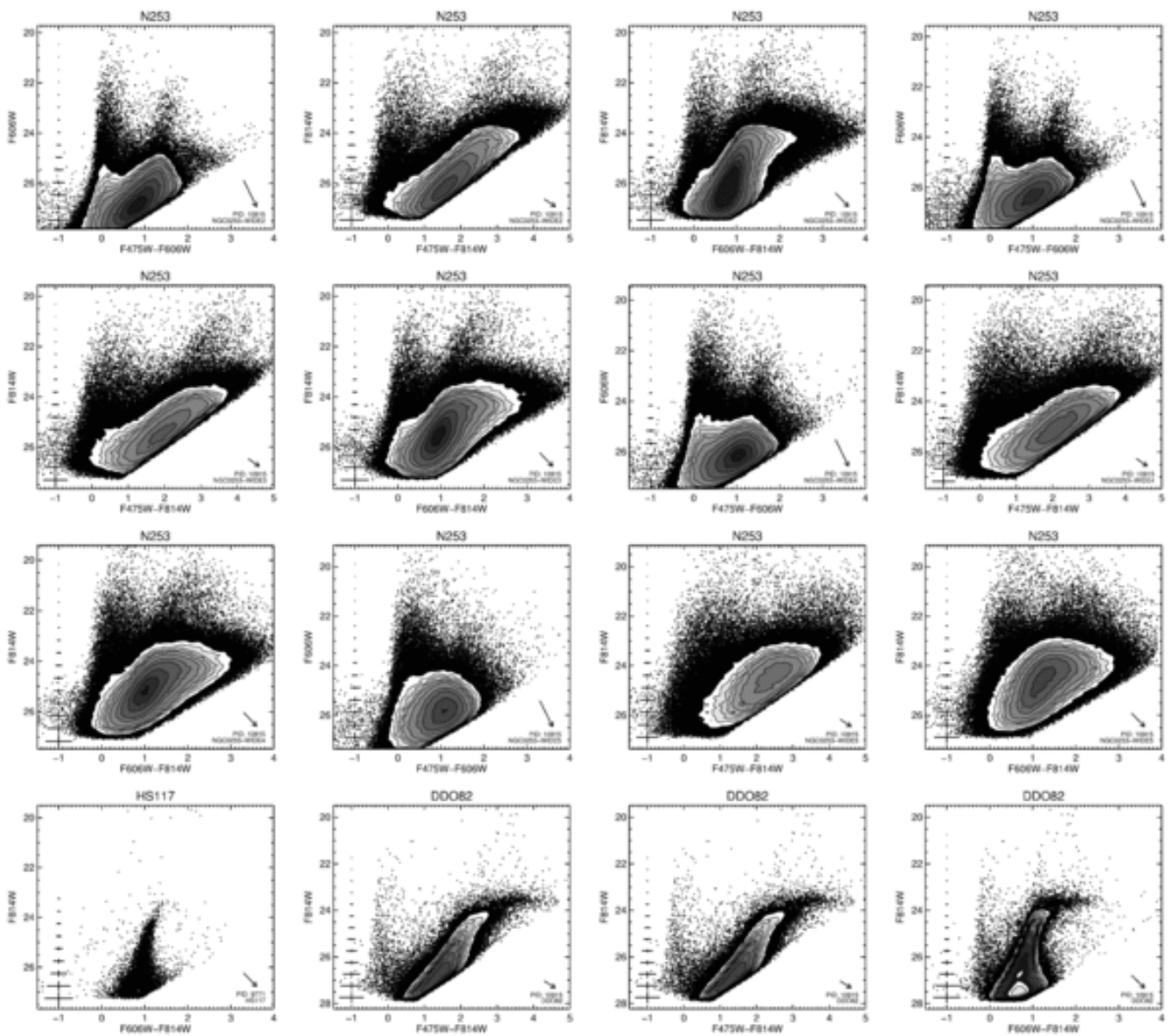
Figure 20. CMDs of galaxies in the ANGST data release, as described in Figure 9. Figures are ordered from the upper left to the bottom right. (a) IKN; (b) KDG73; (c) DDO78; (d) F8D1; (e) F8D1; (f) BK5N; (g) BK5N; (h) N3077; (i) N3077; (j) N3077; (k) N3077; (l) HoI; (m) A0952+69; (n) N253; (o) N253; (p) N253.

Download figure:

 [Standard image](#)

 [High-resolution image](#)

 [Export PowerPoint slide](#)



[Zoom In](#) [Zoom Out](#)

[Reset image size](#)

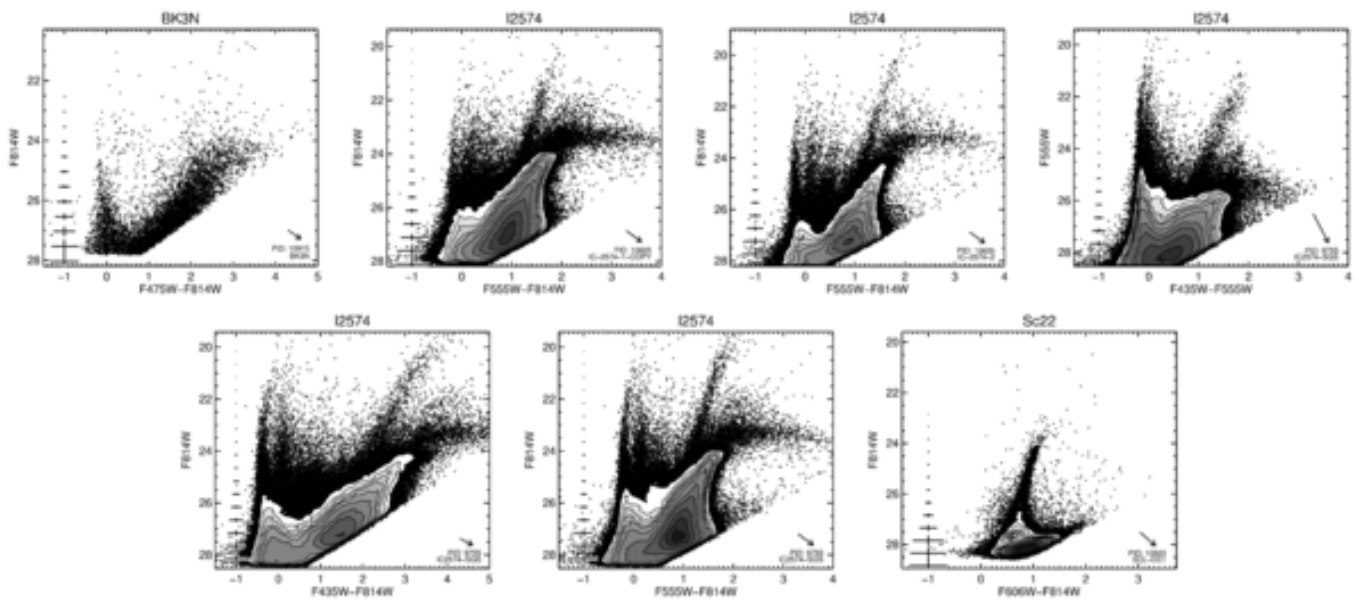
Figure 21. CMDs of galaxies in the ANGST data release, as described in Figure 9. Figures are ordered from the upper left to the bottom right. (a) N253; (b) N253; (c) N253; (d) N253; (e) N253; (f) N253; (g) N253; (h) N253; (i) N253; (j) N253; (k) N253; (l) N253; (m) HS117; (n) DDO82; (o) DDO82; (p) DDO82.

Download figure:

[Standard image](#)

[High-resolution image](#)

[Export PowerPoint slide](#)



[🔍 Zoom In](#)
[🔍 Zoom Out](#)

[🔄 Reset image size](#)

Figure 22. CMDs of galaxies in the ANGST data release, as described in Figure 9. Figures are ordered from the upper left to the bottom right. (a) BK3N; (b) I2574; (c) I2574; (d) I2574; (e) I2574; (f) I2574; (g) Sc22.

Download figure:

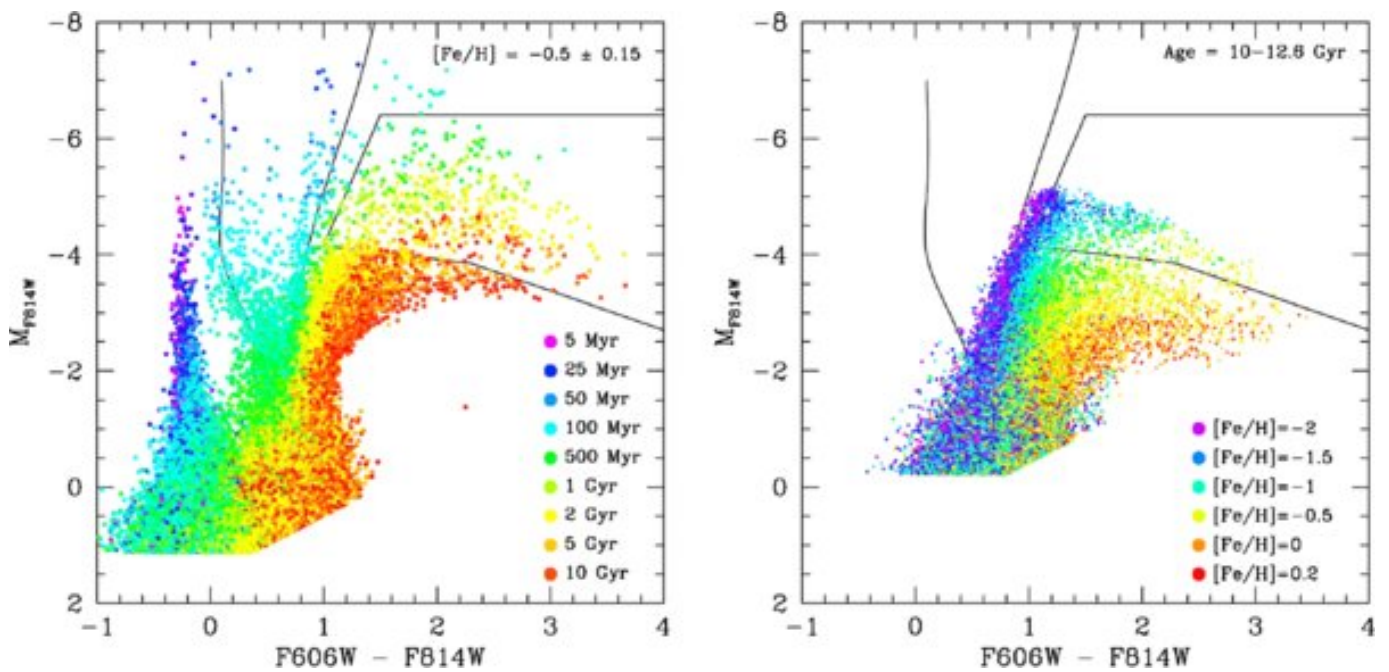
[🖼️ Standard image](#)

[🖼️ High-resolution image](#)

[📄 Export PowerPoint slide](#)

The ANGST CMDs show a richness of detail, thanks to their depth, high photometric accuracy, and large number of stars. As a guide to interpreting the many features visible in these CMDs, in Figure 23 we plot simulated CMDs that show the locations of different stellar populations, as a function of age (right) and metallicity (left). The plots show the CMDs expected for a constant star formation rate color-coded by age (left) and for an early burst of star formation color-coded by metallicity (right), assuming photometric uncertainties

typical for our data at the inner (left panel) and the outer (right) distances of the ANGST target galaxies.



🔍 Zoom In 🔍 Zoom Out

🔄 Reset image size

Figure 23. Simulated CMDs for a constant star formation rate color-coded by age (left) and for a uniform old age color-coded by metallicity (right). The panels adopt the photometric errors and biases for the NGC 0300-WIDE1 (left) and NGC 0253-WIDE1 (right) targets. The three (largely vertical) solid lines indicate several prominent sequences identified with young stellar populations: the main sequence (leftmost line), the blue core helium burning sequence (middle line), and the red core helium burning sequence (rightmost line). The enclosed polygon in the upper right indicates the region typically occupied by AGB stars. The simulated CMDs assume the most recent Girardi et al. (2008) isochrone set.

Download figure:

 Standard image

 High-resolution image

 Export PowerPoint slide

As has been discussed extensively elsewhere (e.g., Gallart et al. 2005,

and references therein), the simulated CMDs show how young stellar populations are found primarily in the upper left of the CMD, older stellar populations are found at lower luminosities and redder colors along the RGB and AGB, and metal rich stars are found at redder colors for older stellar populations. We do not plot the metallicity dependence of younger stars, since the color of the main sequence has essentially no metal dependence for the filters used in this data release.

Also overlaid on Figure [23](#) are tracks indicating the typical locations of young main-sequence stars, of blue and red core helium burning stars (BHeB and RHeB), and AGB stars. Among these features, the blue and red core helium burning sequences are the least widely known, since they are only visible when the CMD is well populated. We note that the HeB sequences can produce potentially confusing features in the CMD. In particular, the upper end of the blue core helium burning sequence can be easily mistaken for a "double" main sequence. Additional vertical sequences sometimes appear where BHeB stars pass through the instability strip, leading to a nearly vertical spread in magnitude for variable stars observed only at a single epoch.

12. MAGNITUDE OF THE TIP OF THE RED GIANT BRANCH

In Table [5](#) we list the F814W magnitude of the TRGB for each galaxy. TRGB magnitudes were determined using the edge-detection filter described in Méndez et al. ([2002](#)) applied to a Gaussian-smoothed luminosity function as in Sakai et al. ([1996](#)) and Seth et al. ([2005b](#)). Although more sophisticated techniques exist (e.g., Makarov et al. [2006](#); Frayn & Gilmore [2003](#)), the TRGB in our sample is typically well-populated and falls well above the photometric limit of the data, making our use of the widely used and calibrated edge-detection technique adequate for an initial distance measurement.

Table 5. TRGB Measurements

Catalog Name	Target Name	Filters	N_{stars}	A_V	Mean Color	$M_{\text{TRGB}} (F814W)$
Antlia	ANTLIA	F606W,F814W	169	0.243	1.05	-4.04
SexA	DDO75	F555W,F814W	276	0.139	1.34	-3.95
N3109	NGC3109-WIDE1	F606W,F814W	355	0.201	1.04	-4.00
N3109	NGC3109-DEEP	F606W,F814W	263	0.201	1.01	-3.98
SexB	SEXB-DEEP	F606W,F814W	754	0.095	0.98	-3.95
KKR25	KKR25	F606W,F814W	80	0.027	1.00	-3.96
KK230	KK230	F606W,F814W	47	0.043	1.00	-4.00
E410-005	ESO410-005	F606W,F814W	194	0.042	1.06	-4.05
E294-010	ESO294-010	F606W,F814W	95	0.018	1.06	-4.05
N55	NGC0055-WIDE1	F606W,F814W	1075	0.041	1.11	-4.00

Catalog Name	Target Name	Filters	N	A	Mean Color	M (F814W)
N55	NGC0055-WIDE2	F606W,F814W	1278	0.041	1.12	-3.99
N55	NGC0055-DEEP	F606W,F814W	323	0.041	1.06	-4.01
N55	NGC0055-DISK	F606W,F814W	7829	0.041	1.17	-4.02
GR8	GR8	F475W,F814W	367	0.080	2.27	-4.03
N300	NGC0300-WIDE1	F475W,F814W	865	0.039	2.67	-4.02
N300	NGC0300-WIDE1	F606W,F814W	1366	0.039	1.33	-4.02
N300	NGC300-5	F435W,F814W	829	0.039	3.40	-4.02
N300	NGC300-5	F555W,F814W	858	0.039	1.85	-4.02
N300	NGC300-6	F435W,F814W	760	0.039	3.41	-4.02
N300	NGC300-6	F555W,F814W	753	0.039	1.81	-4.02

Catalog Name	Target Name	Filters	N	A	Mean Color	M (F814W)
U438	E407-G18	F606W,F814W	715	0.045	0.95	-4.04
DDO187	UGC9128	F606W,F814W	459	0.071	1.03	-4.03
KKH98	KKH98	F475W,F814W	294	0.385	2.23	-4.04
DDO125	UGC7577	F606W,F814W	1990	0.064	1.07	-4.01
U8508	UGC8508	F475W,F814W	738	0.047	2.23	-4.03
KKH86	KKH71	F606W,F814W	108	0.083	1.01	-3.98
DDO99	UGC6817	F606W,F814W	668	0.081	0.99	-3.96
DDO190	DDO190	F606W,F814W	1267	0.038	1.06	-4.05
DDO113	DDO113	F475W,F814W	706	0.063	2.16	-4.05
N4214	NGC4214-DEEP	F606W,F814W	563	0.068	1.13	-3.99
DDO181	UGC8651	F606W,F814W	637	0.019	1.03	-4.03

Catalog Name	Target Name	Filters	N	A	Mean Color	M (F814W)
N3741	NGC3741	F475W,F814W	987	0.077	2.18	4.05
N4163	NGC4163	F475W,F814W	1650	0.062	2.39	-4.02
N4163	NGC4163	F606W,F814W	1513	0.062	1.11	-4.03
N404	NGC0404-DEEP	F606W,F814W	2104	0.181	1.25	-3.99
UA292	UGCA292	F475W,F814W	166	0.048	1.92	-3.98
UA292	UGCA292	F606W,F814W	112	0.048	0.98	-3.98
U8833	UGC8833	F606W,F814W	522	0.037	1.04	-4.04
DDO183	UGC8760	F606W,F814W	604	0.051	1.05	-4.04
N2366	NGC-2366-2	F555W,F814W	2566	0.113	1.50	-4.05
DDO44	DDO44	F475W,F814W	811	0.129	2.26	-4.03

Catalog Name	Target Name	Filters	N	A	Mean Color	M (F814W)
E321-014	PGC39032	F606W,F814W	320	0.293	1.04	-4.00
U4483	UGC4483	F555W,F814W	302	0.105	1.34	-3.94
N2403	NGC2403-DEEP	F606W,F814W	629	0.124	1.11	-4.00
N2403	NGC2403-HALO-1	F606W,F814W	2369	0.124	1.21	-4.02
N2403	NGC2403-HALO-6	F606W,F814W	805	0.124	1.20	-4.02
DDO6	DDO6	F475W,F814W	647	0.053	2.17	-4.05
KKH37	KKH37	F475W,F814W	748	0.231	2.27	-4.03
HoII	UGC-4305-2	F555W,F814W	2461	0.098	1.53	-4.04
KDG2	E540-030	F606W,F814W	179	0.072	1.04	-4.04
MCG9- 20-1	CGCG-269-049	F606W,F814W	46	0.076	1.05	-4.01

Catalog	Target Name	Filters	N	A	Mean Color	M
E540-032	E540-032	F606W,F814W	408	0.064	1.16	-4.05
FM1	M81F6D1	F606W,F814W	636	0.241	1.16	-4.02
KK77	M81F12D1	F606W,F814W	1061	0.442	1.16	-4.02
KDG63	DDO71	F606W,F814W	959	0.303	1.11	-4.03
M82	M82-POS4	F435W,F814W	203	0.191	3.62	-4.00
M82	M82-POS4	F555W,F814W	564	0.191	1.91	-4.01
KDG52	MESSIER-081-DWARF-A	F555W,F814W	330	0.063	1.45	-4.04
DDO53	UGC-04459	F555W,F814W	953	0.118	1.48	-4.05
N2976	N2976-DEEP	F475W,F814W	1334	0.224	2.65	-4.02
N2976	N2976-DEEP	F606W,F814W	1340	0.224	1.24	-4.02

KDG61 Catalog Name	M81K61 Target Name	F606W,F814W Filters	1124 N	0.226 A	1.14 Mean Color	-4.02 M (F814W)
M81	NGC3031-HALO-1	F606W,F814W	227	0.249	1.29	-4.02
M81	M81-FIELD-29	F435W,F814W	551	0.249	3.40	-4.02
M81	M81-FIELD-29	F606W,F814W	330	0.249	1.39	-4.01
M81	M81-DEEP	F606W,F814W	198	0.249	1.35	-4.02
N247	NGC0247-WIDE1	F475W,F814W	2640	0.056	2.64	-4.02
N247	NGC0247-WIDE1	F606W,F814W	3349	0.056	1.30	-4.02
HoIX	UGC-5336	F555W,F814W	273	0.244	1.78	-4.02
KDG64	M81K64	F606W,F814W	951	0.165	1.10	-4.04
IKN	IKN	F606W,F814W	1926	0.181	1.19	-4.02
KDG73	KDG73	F475W,F814W	345	0.056	2.08	-4.04

Catalog Name	Target Name	Filters	N	A	Mean Color	M (F814W)
DDO78	DDO78	F475W,F814W	1494	0.066	2.38	-4.02
F8D1	GAL- 094447+672619_302	F555W,F814W	1355	0.328	1.68	-3.99
BK5N	GAL- 100441+681522_355	F555W,F814W	251	0.195	1.47	-4.01
N3077	NGC3077- PHOENIX	F555W,F814W	333	0.208	1.94	-4.01
HoI	UGC-5139	F555W,F814W	2086	0.153	1.54	-4.03
A0952+69	A0952+69	F475W,F814W	176	0.259	2.20	-4.04
N253	NGC0253-HALO-11	F606W,F814W	1193	0.058	1.23	-4.02
N253	NGC0253-WIDE1	F475W,F814W	2188	0.058	2.63	-4.02
N253	NGC0253-WIDE1	F606W,F814W	3269	0.058	1.26	-4.02
HS117	HS117	F606W,F814W	556	0.359	1.08	-4.05

Catalog Name	Target Name	Filters	N	A_V	Mean Color	M (F814W)
DDO82	DDO82	F475W,F814W	4180	0.133	2.51	-4.02
DDO82	DDO82	F606W,F814W	4594	0.133	1.16	-4.02
BK3N	BK3N	F475W,F814W	235	0.246	2.50	-4.02
I2574	IC-2574-2	F555W,F814W	2425	0.112	1.58	-4.02
I2574	IC2574-SGS	F435W,F814W	5638	0.112	3.11	-4.02
I2574	IC2574-SGS	F555W,F814W	5100	0.112	1.61	-4.02
Sc22	SCL-DE1	F606W,F814W	124	0.046	1.02	-4.02

Notes. Color-dependent absolute magnitudes for the TRGB are taken from Girardi et al. (2008) isochrones. Mean colors are for the stars used to measure the TRGB, which are not necessarily all RGB stars, and include only stars within $0.^m2$ of the TRGB. A_V values are as reported by IRSA for coordinates in Table 1, with the exception of M82. Extinction corrections from A_V to the observed filters are adopted from Girardi et al. (2008), as described in the text. m_{TRGB} was measured in the least crowded region of each galaxy. Measured distances for A0952 + 69, BK3N, and Holmberg IX are dominated by outer M81 stars, rather than RGB stars associated with the named galaxies. Listed uncertainties are dominated by

photometric uncertainties and by stochasticity in the number of stars near the tip; systematic uncertainties (due to uncertainties in the assumed TRGB absolute magnitudes and extinction) are likely to be much larger, but are not included in the listed uncertainties. [a] The distance to MCG9-20-1 is ambiguous, as it was not clear if the observed tip was for the RGB or AGB; the true distance modulus may potentially be significantly fainter.

Download table as:

ASCII

Typeset images:

1

2

The reported F814W TRGB magnitude m_{TRGB} and the associated uncertainty were determined by running 500-750 Monte Carlo trials with bootstrap resampling of the stars. In each trial, additional Gaussian random errors are added to the stars, scaled to the magnitude of each star's photometric error. Each trial returned the magnitude corresponding to the peak of the edge-detection response filter within a 1 mag interval around the likely TRGB. We generated a histogram of the returned magnitudes, and fit the peak at m_{TRGB} in the histogram with a Gaussian. We take the mean and width of the Gaussian to be the magnitude of the TRGB and its uncertainty. Although the Monte Carlo process artificially increases the photometric error (during randomization of magnitudes) and potentially biases m_{TRGB} by scattering stars preferentially above the tip, in practice the effect of the added noise is negligible, since the photometric uncertainties are extremely small at m_{TRGB} in almost every case. Furthermore, we have verified visually that the method above converges on a consistent part of the luminosity function, and thus preserves the accuracy of the relative distances.

In some Monte Carlo trials, there are additional peaks in the edge-

detection response function that clearly do not correspond to the TRGB (see Figure 25). These spurious peaks are most prevalent when there are a smaller number of stars, or an old population of AGB stars with a well-defined peak luminosity. In these cases, we initialized the Gaussian fit with a mean chosen to be centered on the peak corresponding most closely to the true TRGB. Examples of the luminosity function, edge-detection response, histogram of Monte Carlo TRGB magnitudes, and the CMD of the analyzed stars are presented in Figures 24 and 25.

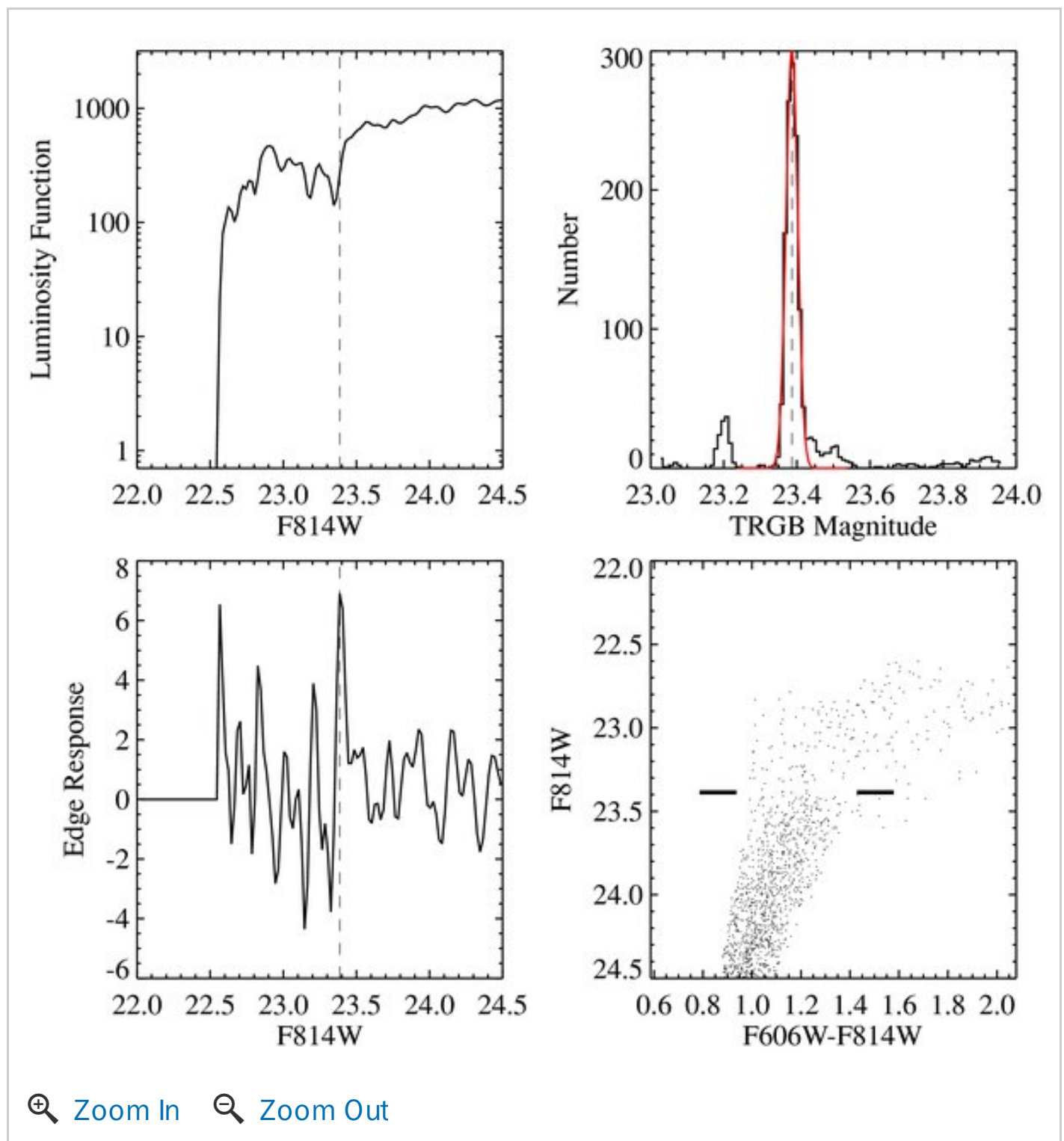


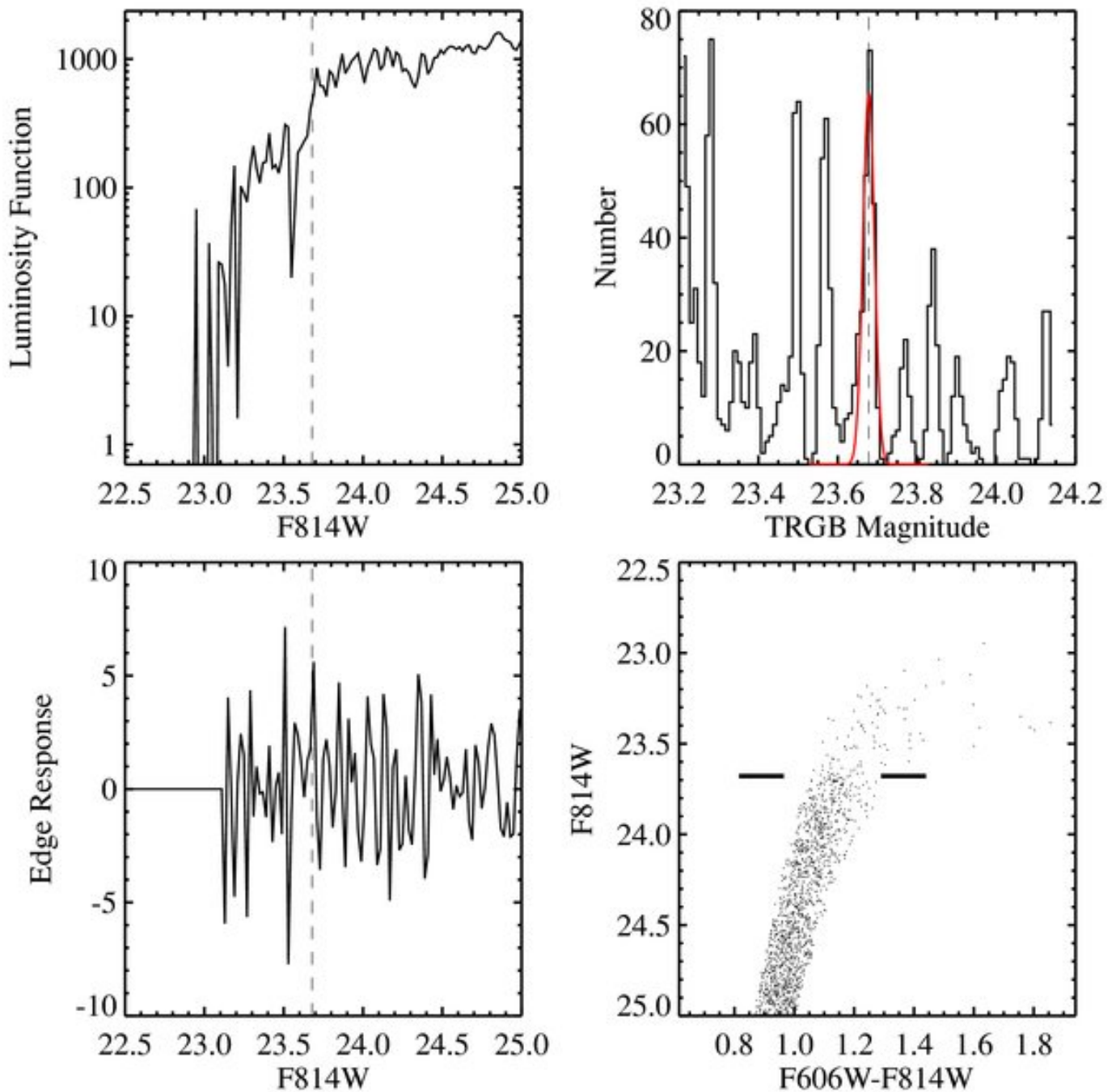
Figure 24. Results of TRGB fitting for NGC 2403, showing the F814W luminosity function (upper left), edge-detection response (lower left), distribution TRGB magnitudes from of Monte Carlo trials (upper right), and the CMD of stars used in the TRGB determination (lower right). The adopted TRGB magnitude is shown as the vertical line in the first three panels, and as the two horizontal tic marks in the lower right panel.

Download figure:

 [Standard image](#)

 [High-resolution image](#)

 [Export PowerPoint slide](#)



🔍 Zoom In 🔍 Zoom Out

🔄 Reset image size

Figure 25. Results of TRGB fitting for KDG63. Panels are the same as in Figure 24. The histogram of Monte Carlo values is more complicated than in Figure 24, due to the smaller number of stars.

Download figure:

🖼️ Standard image

🖼️ High-resolution image

📄 Export PowerPoint slide

Uncertainties in the measured value of m_{TRGB} can include random errors (due to small numbers of stars and to photometric errors) and systematic errors (due to contamination from stars on the red helium burning sequence, to uncertainties in the MW foreground extinction, and to the unknown internal extinction). We attempted to reduce our systematic errors by considering only stars likely to be RGB or AGB stars. To do so, we selected stars that fell within model RGB isochrones from Girardi et al. (2008) in the appropriate HST filter set, extrapolated up into the region populated by AGB stars. This process was automated by first shifting the stars in magnitude and color based on the estimated foreground extinction from Schlegel et al. (1998),²³ assuming $R_V = 3.1$, $A_{\text{F435W}}/A_V = 1.30$, $A_{\text{F475W}}/A_V = 1.15$, $A_{\text{F555W}}/A_V = 1.00$, $A_{\text{F606W}}/A_V = 0.87$, and $A_{\text{F814W}}/A_V = 0.57$, based upon Girardi et al. (2008) for typical temperatures of RGB stars. We used triangular interpolation of the isochrones to generate a regular grid of metallicities as a function of color and magnitude for a uniform, intermediate age population (4 Gyr). We then interpolated the observed stars onto this grid to assign metallicities to each star, and rejected stars with unphysical metallicities. This process is equivalent to assigning each star to a particular RGB isochrone, and rejecting stars that are inconsistent with all plausible isochrones. For the remaining stars, we used a robust bi-weight to find the peak and width of the distribution of the logarithms of the inferred metallicities. We selected all stars whose metallicities fell within 1.5σ of the peak in $\log([Fe/H])$. We further excluded stars with metallicities outside of the range 0.0002 and 0.006 (for 4 Gyr isochrones); within this metallicity range, the F814W magnitude of the TRGB varies by less than ± 0.05 mag, but outside it, the TRGB becomes steadily fainter by several tenths of a magnitude, blurring the TRGB discontinuity and introducing systematic errors when converting m_{TRGB} to distance. We expect little dependence of the TRGB absolute magnitude M_{TRGB} on age or metallicity; the predicted absolute magnitude of the TRGB

depends primarily on the color of the RGB, and more weakly upon the particular age+metallicity combination that generated a particular RGB isochrone. The final isochrone fitting procedure cleanly isolated the bulk of RGB and AGB stars, while significantly reducing contamination from non-RGB features (Figures [24](#) and [25](#)).²⁴

We further reduced systematic biases due to internal extinction and photometric errors by restricting our analysis to stars in regions of low crowding within an individual field, when sufficient numbers of stars were available ($>30,000$). We chose a density threshold such that at least 25% of the area and 50% of the stars were included in the analysis. This cut eliminated stars in the most crowded regions with the highest internal extinction, while still preserving large numbers of stars. For galaxies with multiple pointings, the TRGB was measured in whichever fields had the least crowding and lowest probability of high internal or differential reddening, while still having large numbers of stars. When multiple clean fields were available, we analyzed both, to compare our internal systematics and to constrain the variation in internal extinction. The resulting TRGB magnitudes were frequently several tenths of a magnitude brighter than those measured within the main body of a galaxy. Beyond field placement, however, we make no further attempt to correct for internal extinction, although extinctions of several tenths of a magnitude are certainly possible in the outer regions of massive galaxies (e.g., Holwerda et al. [2008](#)).

To transfer the measured TRGB magnitudes into initial distance estimates, we used the measured mean color within $0.2m$ of the TRGB to pick a Girardi et al. ([2008](#)) isochrone with similar colors, from which we then find the absolute magnitude M_{TRGB} of the TRGB. However, due to the uncertain state of the ACS CTE correction, there are likely to be systematic uncertainties present in the data that limit the accuracy of the inferred distance to a few percent. The likely

systematic uncertainties in the adopted value of M_{TRGB} are even larger, with different theoretical models and empirical calibrations differing by as much as 0.2 mag (e.g., see Figure 8 of Gallart et al. [2005](#)). The reported distances are thus best used as relative distances, rather than absolute ones. The uncertainties listed in Table [5](#) do not include these systematic errors, and include only the Poisson uncertainties captured by bootstrap resampling. Thus, while the Gaussian fitting procedure described above (and seen in the upper left panels of Figures [24](#) and [25](#)) frequently reports formal distance errors of a few percent, the true uncertainties are undoubtedly larger.

The resulting data in Table [5](#) includes: the number of stars within 1 mag of the TRGB (N_{stars}); the adopted foreground extinction A_V ; the mean color (within 0.2 mag of the TRGB) of the stars used to measure the TRGB, for the particular filter combination used; the predicted absolute magnitude of the TRGB at that color, based on isochrones from Girardi et al. ([2008](#)); the apparent magnitude of the TRGB in F814W, uncorrected for extinction ($m_{\text{TRGB}}(\text{raw})$); the extinction corrected TRGB magnitude (m_{TRGB}) and its uncertainty; the resulting extinction corrected distance modulus ($m - M)_0$; and the inferred distance D in Mpc. The resulting spatial configuration of galaxies is shown in Figure [2](#).

Figure [26](#) plots the differences between the new distance moduli and those inferred from distances in Table [1](#), which had been used for initial sample selection, as a function of increasing distance (left) and luminosity (right). The revised distances agree well with previously published values. The median change in distance modulus is only -0.02 mag for the entire sample, indicating that there is little systematic deviation between our adopted TRGB scale and those used in the literature. There is however, a modest tendency for past distances to be systematically overestimated for the most massive

galaxies. If we split the sample into galaxies that are brighter or fainter than $M_B = -17$, the median offset is only -0.012 for the faint galaxies, but increases to -0.074 for the more luminous galaxies. We believe that that offset is most likely due to past TRGB determinations using stars closer to the galaxies' centers, where the extinction of dust is larger, leading the TRGB magnitude to appear fainter. In contrast, our measurements use the outskirts of galaxies, where the internal extinction is small, producing a brighter TRGB. On the other hand, many of the published distance estimates have made corrections for internal extinction, unlike those we present in Table 5.

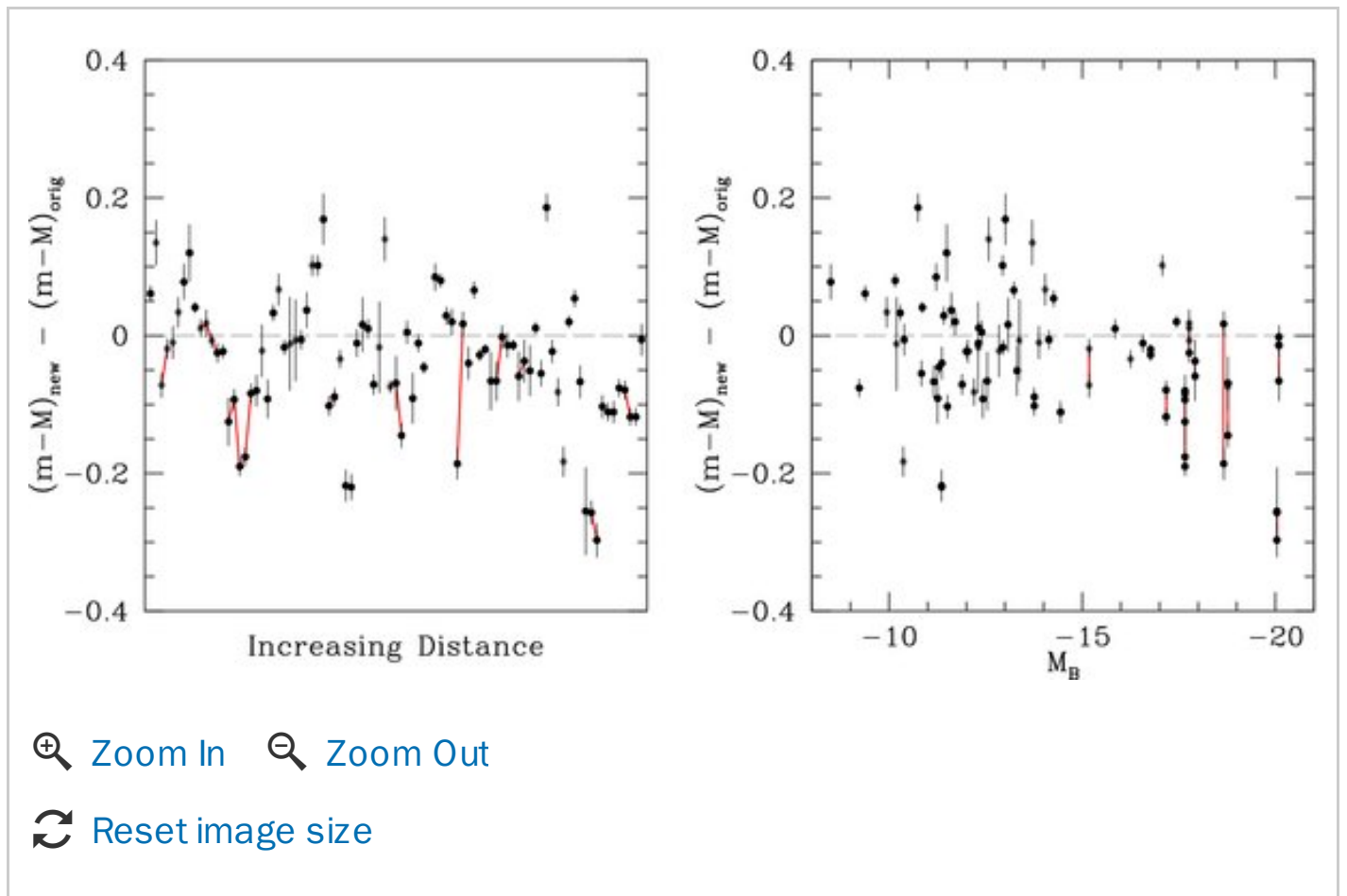


Figure 26. Differences between the new TRGB distance moduli and those used in Table 1 at the time of survey selection, as a function of either each target's position in Table 5, which was sorted by the initial distance estimate (left) or absolute magnitude (right). Solid circles are used for ACS data and asterisks for WFPC2 data. Error bars indicate the Monte Carlo uncertainties reported in Table 5, but do not include systematic uncertainties due to dust

extinction or the adopted TRGB absolute magnitudes. The median change in distance modulus is only -0.02 mag, and the dispersion about the mean is 0.05 mag. Multiple observations of the same galaxy are connected with a solid line (for NGC 3109, NGC 55, NGC 300, NGC 4163, UA292, NGC 2403, M82, NGC 2976, M81, NGC 247, NGC 253, DDO82, and IC 2574), and show differences of typically less than 0.1 mag (i.e. 10% in distance). This variation is likely to be dominated by differences in internal extinction at different locations within the galaxy, with the outermost distance measurement being least likely to be affected by dust but more likely to be affected by Poisson uncertainties due to reduced numbers of stars.

Download figure:

 [Standard image](#)

 [High-resolution image](#)

 [Export PowerPoint slide](#)

Because the most luminous galaxies tend to be found in the M81 group, the left panel shows a hint of correlation between distance and the offset in the distance modulus. However, the Spearman rank correlation coefficient is much smaller when using distance instead of luminosity (-0.09 versus 0.30), indicating that the variation in luminosity is the principal driver of the trend.

The dispersion about the mean difference is 0.05 mag, comparable to the precision of distances in Table [1](#) and to their published uncertainties. There is no difference in the dispersion for brighter and fainter galaxies. Multiple observations of the same galaxy (connected with a solid line in Figure [26](#)) show differences of typically less than 0.1 mag (i.e. 10% in distance). Because these measurements were made in different regions of these galaxies, some of this variation is likely to

be due to differences in internal extinction within the galaxy. In such cases, the outermost distance measurement is likely to be the least affected by dust, although the reduced numbers of stars in such fields leads to larger Poisson uncertainties. We also found no systematic offsets between distances determined with ACS and those measured with WFPC2 data.

We see no evidence that the revised distances would have changed our initial sample selection. The largest change in distance is for UGCA 292, which is nearly 40% further away than previously estimated from its brightest stars (Makarova et al. [1998](#)). The distance to MCG9-20-131 also appeared to decrease significantly; however, there is some ambiguity as to whether or not the apparent TRGB is due to RGB or AGB stars, or potentially even red supergiants. Thus, the distance may have a systematic offset, even though the formal error on the magnitude of the tip is relatively small. With the new distances, NGC 247 and NGC 253 are much closer to each other. The morphology of the other groups remain essentially unchanged.

13. CONCLUSIONS

The ACS Nearby Galaxy Survey Treasury is the now the largest repository of uniform stellar photometry for nearby galaxies. The resulting catalogs contain millions of measurements that can be used for studies of ancient and recent SFHs (Williams et al. [2009](#); Weisz et al. [2008](#)) and comparisons with multi-wavelength data (Gogarten et al. [2009](#); Ott et al. [2008](#)). The raw images are a resource for searches for stellar clusters, H ii region nebulosity, and background light sources.

We are happy to acknowledge the consistently professional and helpful assistance from the staff at STSCI, including Alison Vick, Marco Sirianni, Howard Bond, and Neill Reid. We also are pleased to

thank Jay Anderson, Brent Tully, Abi Saha, Stan Vlcek, Pat Taylor, Sarah Garner, and Richard Coffey for assistance at various times during the project. We also thank the referee for constructive comments. J.J.D. acknowledges partial support from the Wyckoff Faculty Fellowship during this work, and the hospitality of the MPIA and Carnegie Observatories during some of the writing of this paper. L.G. acknowledges financial support from contract ASI-INAF I/016/07/0. I.K. and V.K. were partially supported by RFFI grant 07-02-00005 and grant DFG-RFBR 06-02-04017.

This work is based on observations made with the NASA/ESA *Hubble Space Telescope*, obtained from the data archive at the Space Telescope Science Institute. Support for this work was provided by NASA through grant number GO-10915 from the Space Telescope Science Institute, which is operated by AURA, Inc., under NASA contract NAS 5-26555. This research has made use of the NASA/IPAC Infrared Science Archive and the NASA/IPAC Extragalactic Database (NED), which are both operated by the Jet Propulsion Laboratory, California Institute of Technology, under contract with the National Aeronautics and Space Administration. This research has made extensive use of NASA's Astrophysics Data System Bibliographic Services.

Facilities: *HST*(ACS), *HST*(WFPC2)

Footnotes

- 19 These updated distances agree with the distances in Table [1](#) to 10% in almost all cases, as discussed in Section [12](#).
- 20 <http://purcell.as.arizona.edu/dolphot>.
- 21 Preliminary versions of revised ACS charge transfer efficiency (CTE) corrections have recently been released on STScI's Web site, but were announced after all the data had been processed for this release. These

corrections will be used in subsequent releases, and updated on the data release Web site.

- 22 Note that the Bedin et al. ([2005](#)) ACS calibration also assumes that $m_{F814W,WFPC2} = 0.0$ (giving $m_{zp,F814W,ACS} = 25.492$), so comparisons with this alternate calibration also require adding an +0.035 offset; this correction was not made during the WFPC2-ACS comparison in Saviane et al. ([2008](#)), and thus their apparent agreement of $m_{F814W,WFPC2} - m_{F814W,ACS} = 0.003 \pm 0.005$ actually implies that $m_{F814W,WFPC2} - m_{F814W,ACS} = 0.038 \pm 0.005$ over the magnitude and color range of $26 < m_{F814W,ACS} < 27.5$ and $0 < m_{F606W,ACS} - m_{F814W,ACS} < 2$.
- 23 The one exception is M82, for which the Schlegel et al. ([1998](#)) value is clearly contaminated by point source emission from M82 itself, leading to an erroneously high foreground extinction ($A_B = 0.685$). Instead, we took $A_B = 0.25$, based upon regions immediately adjacent to M82.
- 24 Note that although we derived the "metallicity" of each star, we do not treat these as actual measurements of the metallicity due to the likely presence of mixed stellar ages on the RGB; instead, we only use the inferred metallicity as a label for the RGB isochrone on which a star lies. Likewise, the mean color that we report for the TRGB stars includes only those stars that made the various metallicity cuts, and does not reflect the color of the RGB as a whole.

References

- [↑](#) Aparicio, A. & Tikhonov, N. 2000, *AJ*, **119**, 2183
[IOPscience](#) [ADS](#)
- [↑](#) Bedin, L. R., Cassisi, S., Castelli, F., Piotto, G., Anderson, J., Salaris, M., Momany, Y., & Pietrinferni, A. 2005, *MNRAS*, **357**, 1038
[Crossref](#) [ADS](#)
- [↑](#) Begum, A. & Chengalur, J. N. 2005, *MNRAS*, **362**, 609
[Crossref](#) [ADS](#)

- [↑](#) Bertin, E. & Arnouts, S. 1996, *A&AS*, **117**, 393
[Crossref](#) [ADS](#)
- [↑](#) Butler, D. J., Martínez-Delgado, D., & Brandner, W. 2004, *AJ*, **127**, 1472
[IOPscience](#) [ADS](#)
- [↑](#) Caldwell, N., Armandroff, T. E., Da Costa, G. S., & Seitzer, P. 1998, *AJ*, **115**, 535
[IOPscience](#) [ADS](#)
- [↑](#) Chiboucas, K., Karachentsev, I. D., & Tully, R. B. 2009, *AJ*, **137**, 3009
[IOPscience](#) [ADS](#)
- [↑](#) del Río, M. S., Brinks, E., & Cepa, J. 2004, *AJ*, **128**, 89
[IOPscience](#) [ADS](#)
- [↑](#) Dohm-Palmer, R. C., Skillman, E. D., Mateo, M., Saha, A., Dolphin, A., Tolstoy, E., Gallagher, J. S., & Cole, A. A. 2002, *AJ*, **123**, 813
[IOPscience](#) [ADS](#)
- [↑](#) Dohm-Palmer, R. C. et al. 1997, *AJ*, **114**, 2514
[Crossref](#) [ADS](#)
- [↑](#) Dolphin, A. E. 2000, *PASP*, **112**, 1383
[IOPscience](#) [ADS](#)
- [↑](#) Dolphin, A. E. 2002, *MNRAS*, **332**, 91
[Crossref](#) [ADS](#)
- [↑](#) Dolphin, A. E. et al. 2001, *MNRAS*, **324**, 249
[Crossref](#) [ADS](#)
- [↑](#) Dolphin, A. E. et al. 2002, *AJ*, **123**, 3154
[IOPscience](#) [ADS](#)

- [↑](#) Drozdovsky, I. O., Schulte-Ladbeck, R. E., Hopp, U., Greggio, L., & Crone, M. M. 2002, *AJ*, **124**, 811
[IOPscience](#) [ADS](#)
- [↑](#) Frayn, C. M. & Gilmore, G. F. 2003, *MNRAS*, **339**, 887
[Crossref](#) [ADS](#)
- [↑](#) Freedman, W. L. et al. 1994, *ApJ*, **427**, 628
[Crossref](#) [ADS](#)
- [↑](#) Gallart, C., Zoccali, M., & Aparicio, A. 2005, *ARA&A*, **43**, 387
[Crossref](#) [ADS](#)
- [↑](#) Gieren, W., Pietrzy ski, G., Soszy ski, I., Bresolin, F., Kudritzki, R.-P., Minniti, D., & Storm, J. 2005, *ApJ*, **628**, 695
[IOPscience](#) [ADS](#)
- [↑](#) Gieren, W. et al. 2004, *AJ*, **128**, 1167
[IOPscience](#) [ADS](#)
- [↑](#) Girardi, L. et al. 2008, *PASP*, **120**, 583
[IOPscience](#) [ADS](#)
- [↑](#) Gogarten, S. M. et al. 2009, *ApJ*, **691**, 115
[IOPscience](#) [ADS](#)
- [↑](#) Holtzman, J. A., Afonso, C., & Dolphin, A. 2006, *ApJS*, **166**, 534
[IOPscience](#) [ADS](#)
- [↑](#) Holtzman, J. A., Burrows, C. J., Casertano, S., Hester, J. J., Trauger, J. T., Watson, A. M., & Worthey, G. 1995, *PASP*, **107**, 1065
[IOPscience](#) [ADS](#)
- [↑](#) Holwerda, B. W., Keel, W. C., Williams, B., Dalcanton, J. J., & de Jong, R. S. 2009, *AJ*, **137**, 3000
[IOPscience](#) [ADS](#)

- [↑](#) Izotov, Y. I. & Thuan, T. X. 2002, *ApJ*, **567**, 875
[IOPscience](#) [ADS](#)
- [↑](#) Jarrett, T. H., Chester, T., Cutri, R., Schneider, S. E., & Huchra, J. P. 2003, *AJ*, **125**, 525
[IOPscience](#) [ADS](#)
- [↑](#) Jee, M. J., Blakeslee, J. P., Sirianni, M., Martel, A. R., White, R. L., & Ford, H. C. 2007, *PASP*, **119**, 1403
[IOPscience](#) [ADS](#)
- [↑](#) Karachentsev, I. D. 2005, *AJ*, **129**, 178
[IOPscience](#) [ADS](#)
- [↑](#) Karachentsev, I. D., Karachentseva, V. E., Huchtmeier, W. K., & Makarov, D. I. 2004, *AJ*, **127**, 2031
[IOPscience](#) [ADS](#)
- [↑](#) Karachentsev, I. D. et al. 2001, *A&A*, **379**, 407
[Crossref](#) [ADS](#)
- [↑](#) Karachentsev, I. D. et al. 2002a, *A&A*, **383**, 125
[Crossref](#) [ADS](#)
- [↑](#) Karachentsev, I. D. et al. 2002b, *A&A*, **385**, 21
[Crossref](#) [ADS](#)
- [↑](#) Karachentsev, I. D. et al. 2002c, *A&A*, **389**, 812
[Crossref](#) [ADS](#)
- [↑](#) Karachentsev, I. D. et al. 2003, *A&A*, **404**, 93
[Crossref](#) [ADS](#)
- [↑](#) Karachentsev, I. D. et al. 2006, *AJ*, **131**, 1361
[IOPscience](#) [ADS](#)

- [↑](#) Kennicutt, R. et al. 2007, *American Astronomical Society Meeting Abstracts*, **211**, 95.02
[ADS](#)
- [↑](#) Koekemoer, A. M., Fruchter, A. S., Hook, R. N., & Hack, W. 2002, *The 2002 HST Calibration Workshop: Hubble after the Installation of the ACS and the NICMOS Cooling System*, ed. S. Arribas, A. Koekemoer, & B. Whitmore (Baltimore, MD: Space Telescope Science Institute), 337
[ADS](#)
- [↑](#) Krist, J. 1995, *ASP Conf. Ser. 77, Astronomical Data Analysis Software and Systems IV*, ed. R. A. Shaw, H. E. Payne, & J. J. E. Hayes (San Francisco, CA: ASP), 349
[ADS](#)
- [↑](#) Maíz-Apellániz, J., Cieza, L., & MacKenty, J. W. 2002, *AJ*, **123**, 1307
[IOPscience](#) [ADS](#)
- [↑](#) Makarov, D., Makarova, L., Rizzi, L., Tully, R. B., Dolphin, A. E., Sakai, S., & Shaya, E. J. 2006, *AJ*, **132**, 2729
[IOPscience](#) [ADS](#)
- [↑](#) Makarova, L., Karachentsev, I., Takalo, L. O., Heinaemaeki, P., & Valtonen, M. 1998, *A&AS*, **128**, 459
[Crossref](#) [ADS](#)
- [↑](#) Mannucci, F., Basile, F., Poggianti, B. M., Cimatti, A., Daddi, E., Pozzetti, L., & Vanzi, L. 2001, *MNRAS*, **326**, 745
[Crossref](#) [ADS](#)
- [↑](#) Méndez, B., Davis, M., Moustakas, J., Newman, J., Madore, B. F., & Freedman, W. L. 2002, *AJ*, **124**, 213
[IOPscience](#) [ADS](#)
- [↑](#) Minniti, D., Zijlstra, A. A., & Alonso, M. V. 1999, *AJ*, **117**, 881
[IOPscience](#) [ADS](#)

- [↑](#) Mouhcine, M., Ferguson, H. C., Rich, R. M., Brown, T. M., & Smith, T. E. 2005, *ApJ*, **633**, 810
[IOPscience](#) [ADS](#)
- [↑](#) Mutchler, M. et al. 2007, *PASP*, **119**, 1
[IOPscience](#) [ADS](#)
- [↑](#) Olsen, K. A. G., Blum, R. D., & Rigaut, F. 2003, *AJ*, **126**, 452
[IOPscience](#) [ADS](#)
- [↑](#) Ott, J., Skillman, E., Dalcanton, J., Walter, F., Stilp, A., Koribalski, B., West, A., & Warren, S. 2008, arXiv:0805.4605
[ADS](#) [Preprint](#)
- [↑](#) Rekola, R., Richer, M. G., McCall, M. L., Valtonen, M. J., Kotilainen, J. K., & Flynn, C. 2005, *MNRAS*, **361**, 330
[Crossref](#) [ADS](#)
- [↑](#) Rhodes, J. D., Massey, R., Albert, J., Taylor, J. E., Koekemoer, A. M., & Leauthaud, A. 2006, *The 2005 HST Calibration Workshop: Hubble After the Transition to Two-Gyro Mode*, ed. A. M. Koekemoer, P. Goudfrooij, & L. L. Dressel, 21
[ADS](#)
- [↑](#) Rizzi, L., Bresolin, F., Kudritzki, R.-P., Gieren, W., & Pietrzyński, G. 2006, *ApJ*, **638**, 766
[IOPscience](#) [ADS](#)
- [↑](#) Sakai, S., Madore, B. F., & Freedman, W. L. 1996, *ApJ*, **461**, 713
[Crossref](#) [ADS](#)
- [↑](#) Sakai, S. & Madore, B. F. 1999, *ApJ*, **526**, 599
[IOPscience](#) [ADS](#)
- [↑](#) Sakai, S. & Madore, B. F. 2001, *ApJ*, **555**, 280

[IOPscience](#) [ADS](#)

[↑](#) Saviane, I., Momany, Y., da Costa, G. S., Rich, R. M., & Hibbard, J. E. 2008, *ApJ*, **678**, 179

[IOPscience](#) [ADS](#)

[↑](#) Schlegel, D. J., Finkbeiner, D. P., & Davis, M. 1998, *ApJ*, **500**, 525

[IOPscience](#) [ADS](#)

[↑](#) Seth, A. C., Dalcanton, J. J., & de Jong, R. S. 2005a, *AJ*, **129**, 1331

[IOPscience](#) [ADS](#)

[↑](#) Seth, A. C., Dalcanton, J. J., & de Jong, R. S. 2005b, *AJ*, **130**, 1574

[IOPscience](#) [ADS](#)

[↑](#) Sirianni, M. et al. 2005, *PASP*, **117**, 1049

[IOPscience](#) [ADS](#)

[↑](#) Tikhonov, N. A., Galazutdinova, O. A., & Aparicio, A. 2003, *A&A*, **401**, 863

[Crossref](#) [ADS](#)

[↑](#) Tully, R. B. et al. 2006, *AJ*, **132**, 729

[IOPscience](#) [ADS](#)

[↑](#) Vaduvescu, O., McCall, M. L., Richer, M. G., & Fingerhut, R. L. 2005, *AJ*, **130**, 1593

[IOPscience](#) [ADS](#)

[↑](#) van den Bergh, S. 2000, *PASP*, **112**, 529

[IOPscience](#) [ADS](#)

[↑](#) Weisz, D. R., Skillman, E. D., Cannon, J. M., Dolphin, A. E., Kennicutt, R. C., Jr., Lee, J., & Walter, F. 2008, *ApJ*, **689**, 160

[IOPscience](#) [ADS](#)

[↑](#) Williams, B. F. et al. 2009, *AJ*, **137**, 419

- [↑](#) Windhorst, R. A., Cohen, S. H., Hathi, N. P., Jansen, R. A., & Ryan, R. E. 2008, *AIP Conf. Proc. 1035, The Evolution of Galaxies Through the Neutral Hydrogen Window* (New York: AIP), 318

[ADS](#)

Export references:

[BibTeX](#)

[RIS](#)

Citations

1. The disc-averaged star formation relation for Local Volume dwarf galaxies
Á *et al* 2018 *Monthly Notices of the Royal Astronomical Society* **480** 210
[Crossref](#)
2. Scientific discovery with the James Webb Space Telescope
Jason Kalirai 2018 *Contemporary Physics* 1
[Crossref](#)
3. Star formation complexes in the ‘galaxy-sized’ supergiant shell of the galaxy Holmberg I
Oleg V Egorov *et al* 2018 *Monthly Notices of the Royal Astronomical Society* **478** 3386
[Crossref](#)
4. Star formation in the outskirts of DDO 154: a top-light IMF in a nearly dormant disc
Adam B Watts *et al* 2018 *Monthly Notices of the Royal Astronomical Society* **477** 5554
[Crossref](#)
5. Exploring the dust content of galactic winds with Herschel – II. Nearby dwarf galaxies
Alexander McCormick *et al* 2018 *Monthly Notices of the Royal Astronomical Society* **477** 699

[Crossref](#)

6. Spatially offset AGN candidates in the CLASS survey

Chris J Skipper and Ian W A Browne 2018 *Monthly Notices of the Royal Astronomical Society* **475** 5179

[Crossref](#)

7. A plane of high-velocity galaxies across the Local Group

Indranil Banik and Hongsheng Zhao 2018 *Monthly Notices of the Royal Astronomical Society* **473** 4033

[Crossref](#)

8. Direct Evidence for Maser Emission from the 36.2 GHz Class I Transition of Methanol in NGC253

Xi Chen *et al.* 2018 *The Astrophysical Journal Letters* **856** L35

[IOPscience](#)

9. The Fourteenth Data Release of the Sloan Digital Sky Survey: First Spectroscopic Data from the Extended Baryon Oscillation Spectroscopic Survey and from the Second Phase of the Apache Point Observatory Galactic Evolution Experiment

Bela Abolfathi *et al.* 2018 *The Astrophysical Journal Supplement Series* **235** 42

[IOPscience](#)

10. The Resolved Stellar Populations in the LEGUS Galaxies¹

E. Sabbi *et al.* 2018 *The Astrophysical Journal Supplement Series* **235** 23

[IOPscience](#)

11. Stellar Populations in the Outer Disk and Halo of the Spiral Galaxy M101

J. Christopher Mihos *et al.* 2018 *The Astrophysical Journal* **862** 99

[IOPscience](#)

12. Near-infrared Spectral Evolution of the Type Ia Supernova 2014J in the Nebular Phase: Implications for the Progenitor System

T. R. Diamond *et al.* 2018 *The Astrophysical Journal* **861** 119

[IOPscience](#)

13. The MALATANG Survey: The $L_{\text{GAS}} - L_{\text{IR}}$ Correlation on Sub-kiloparsec Scale in

Six Nearby Star-forming Galaxies as Traced by HCN $J=4-3$ and HCO⁺
 $J=4-3$

Qing-Hua Tan *et al.* 2018 *The Astrophysical Journal* **860** 165

[IOPscience](#)

14. Constraints for the Progenitor Masses of Historic Core-collapse Supernovae
Benjamin F. Williams *et al.* 2018 *The Astrophysical Journal* **860** 39

[IOPscience](#)

15. Seeing Red in NGC 1978, NGC 55, and NGC 3109

T. J. Davidge 2018 *The Astrophysical Journal* **856** 129

[IOPscience](#)

16. A Study of Two Dwarf Irregular Galaxies with Asymmetrical Star Formation
Distributions

Deidre A. Hunter *et al.* 2018 *The Astrophysical Journal* **855** 7

[IOPscience](#)

17. Mapping Circumstellar Matter with Polarized Light: The Case of Supernova
2014J in M82

Yi Yang *et al.* 2018 *The Astrophysical Journal* **854** 55

[IOPscience](#)

18. Late-time Flattening of Type Ia Supernova Light Curves: Constraints from SN
2014J in M82

Yi Yang *et al.* 2018 *The Astrophysical Journal* **852** 89

[IOPscience](#)

19. The Carnegie–Chicago Hubble Program. III. The Distance to NGC 1365 via the
Tip of the Red Giant Branch

In Sung Jang *et al.* 2018 *The Astrophysical Journal* **852** 60

[IOPscience](#)

20. Schuyler D. Van Dyk 2017 693

[Crossref](#)

21. The direct identification of core-collapse supernova progenitors

Schuyler D. Van Dyk 2017 *Philosophical Transactions of the Royal Society A:
Mathematical, Physical and Engineering Sciences* **375** 20160277

[Crossref](#)

22. Class I methanol masers in NGC 253: Alcohol at the end of the bar
S. P. Ellingsen *et al* 2017 *Monthly Notices of the Royal Astronomical Society* **472** 604

[Crossref](#)

23. The role of environment on the star formation history of disc galaxies
Xiaoyu Kang *et al* 2017 *Monthly Notices of the Royal Astronomical Society* **469** 1636

[Crossref](#)

24. The frequency and stellar-mass dependence of boxy/peanut-shaped bulges in barred galaxies
Peter Erwin and Victor P. Debattista 2017 *Monthly Notices of the Royal Astronomical Society* **468** 2058

[Crossref](#)

25. Supernova progenitors, their variability and the Type IIP Supernova ASASSN-16fq in M66
C. S. Kochanek *et al* 2017 *Monthly Notices of the Royal Astronomical Society* **467** 3347

[Crossref](#)

26. ^{22}Ne and ^{23}Na ejecta from intermediate-mass stars: the impact of the new LUNA rate for $^{22}\text{Ne}(p, \gamma)^{23}\text{Na}$
A. Slemer *et al* 2017 *Monthly Notices of the Royal Astronomical Society* **465** 4817

[Crossref](#)

27. Detection of HC_3N Maser Emission in NGC 253
Simon P. Ellingsen *et al.* 2017 *The Astrophysical Journal Letters* **841** L14

[IOPscience](#)

28. The 13th Data Release of the Sloan Digital Sky Survey: First Spectroscopic Data from the SDSS-IV Survey Mapping Nearby Galaxies at Apache Point Observatory
Franco D. Albareti *et al.* 2017 *The Astrophysical Journal Supplement*

29. A Rogues' Gallery of Andromeda's Dwarf Galaxies. I. A Predominance of Red Horizontal Branches
Nicolas F. Martin *et al.* 2017 *The Astrophysical Journal* **850** 16
[IOPscience](#)
30. Molecular-cloud-scale Chemical Composition. I. A Mapping Spectral Line Survey toward W51 in the 3 mm Band
Yoshimasa Watanabe *et al.* 2017 *The Astrophysical Journal* **845** 116
[IOPscience](#)
31. Planetary Nebulae and H ii Regions in the Starburst Irregular Galaxy NGC 4449 from LBT MODS Data
F. Annibali *et al.* 2017 *The Astrophysical Journal* **843** 20
[IOPscience](#)
32. A New Approach to Convective Core Overshooting: Probabilistic Constraints from Color–Magnitude Diagrams of LMC Clusters
Philip Rosenfield *et al.* 2017 *The Astrophysical Journal* **841** 69
[IOPscience](#)
33. The Dragonfly Nearby Galaxies Survey. III. The Luminosity Function of the M101 Group
Shany Danieli *et al.* 2017 *The Astrophysical Journal* **837** 136
[IOPscience](#)
34. The Candidate Progenitor of the Type IIc SN 2010jl Is Not an Optically Luminous Star
Ori D. Fox *et al.* 2017 *The Astrophysical Journal* **836** 222
[IOPscience](#)
35. CO Spectral Line Energy Distributions in Galactic Sources: Empirical Interpretation of Extragalactic Observations
Nick Indriolo *et al.* 2017 *The Astrophysical Journal* **836** 117
[IOPscience](#)
36. The Tip of the Red Giant Branch Distances to Type Ia Supernova Host

[IOPscience](#)

37. The Effect of Variability on X-Ray Binary Luminosity Functions: Multiple-epoch Observations of NGC 300 with Chandra
B. Binder *et al.* 2017 *The Astrophysical Journal* **834** 128
[IOPscience](#)
38. The Panchromatic Hubble Andromeda Treasury. XVII. Examining Obscured Star Formation with Synthetic Ultraviolet Flux Maps in M31.
Alexia R. Lewis *et al.* 2017 *The Astrophysical Journal* **834** 70
[IOPscience](#)
39. Interstellar-medium Mapping in M82 through Light Echoes around Supernova 2014J
Yi Yang *et al.* 2017 *The Astrophysical Journal* **834** 60
[IOPscience](#)
40. Red Clump Stars
Léo Girardi 2016 *Annual Review of Astronomy and Astrophysics* **54** 95
[Crossref](#)
41. Constraining the escape fraction of ionizing photons from H ii regions within NGC 300: A concept paper
F. Niederhofer *et al.* 2016 *Astronomy & Astrophysics* **592** A47
[Crossref](#)
42. Dark influences
T. K. Starkeburg *et al.* 2016 *Astronomy & Astrophysics* **587** A24
[Crossref](#)
43. SN 2014J at M82 – I. A middle-class Type Ia supernova by all spectroscopic metrics
L. Galbany *et al.* 2016 *Monthly Notices of the Royal Astronomical Society* **457** 525
[Crossref](#)
44. The star formation history of low-mass disk galaxies: A case study of NGC

[Crossref](#)

45. Disappearance of the Progenitor of Supernova iPTF13bvn
Gastón Folatelli *et al.* 2016 *The Astrophysical Journal Letters* **825** L22
[IOPscience](#)
46. Post-maximum Near-infrared Spectra of SN 2014J: A Search for Interaction Signatures
D. J. Sand *et al.* 2016 *The Astrophysical Journal Letters* **822** L16
[IOPscience](#)
47. Rotational Dynamics and Star Formation in the Nearby Dwarf Galaxy NGC 5238
John M. Cannon *et al.* 2016 *The Astronomical Journal* **152** 202
[IOPscience](#)
48. Isolating the Young Stellar Population in the Outer Disk of NGC 300
Tristan J. Hillis *et al.* 2016 *The Astrophysical Journal* **831** 191
[IOPscience](#)
49. Rising from the Ashes: Mid-infrared Re-brightening of the Impostor SN 2010da in NGC 300
Ryan M. Lau *et al.* 2016 *The Astrophysical Journal* **830** 142
[IOPscience](#)
50. A Spectroscopic Study of Blue Supergiant Stars in the Sculptor Galaxy NGC 55: Chemical Evolution and Distance
R. P. Kudritzki *et al.* 2016 *The Astrophysical Journal* **829** 70
[IOPscience](#)
51. Asymmetries in SN 2014J near Maximum Light Revealed through Spectropolarimetry
Amber L. Porter *et al.* 2016 *The Astrophysical Journal* **828** 24
[IOPscience](#)
52. The Panchromatic Hubble Andromeda Treasury. XV. The BEAST: Bayesian Extinction and Stellar Tool

Karl D. Gordon *et al.* 2016 *The Astrophysical Journal* **826** 104

[IOPscience](#)

53. The Distance to M51

Kristen. B. W. McQuinn *et al.* 2016 *The Astrophysical Journal* **826** 21

[IOPscience](#)

54. Measurements of the Soft Gamma-Ray Emission from SN2014J with Suzaku

Y. Terada *et al.* 2016 *The Astrophysical Journal* **823** 43

[IOPscience](#)

55. The Extended Halo of Centaurus A: Uncovering Satellites, Streams, and Substructures

D. Crnojevi *et al.* 2016 *The Astrophysical Journal* **823** 19

[IOPscience](#)

56. Evolution of Thermally Pulsing Asymptotic Giant Branch Stars. V. Constraining the Mass Loss and Lifetimes of Intermediate-mass, Low-metallicity AGB Stars

Philip Rosenfield *et al.* 2016 *The Astrophysical Journal* **822** 73

[IOPscience](#)

57. A Deep Search for Prompt Radio Emission from Thermonuclear Supernovae with the Very Large Array

Laura Chomiuk *et al.* 2016 *The Astrophysical Journal* **821** 119

[IOPscience](#)

58. The imprint of reionization on the star formation histories of dwarf galaxies

A. Benítez-Llambay *et al.* 2015 *Monthly Notices of the Royal Astronomical Society* **450** 4207

[Crossref](#)

59. Faint dwarfs as a test of DM models: WDM versus CDM

F. Governato *et al.* 2015 *Monthly Notices of the Royal Astronomical Society* **448** 792

[Crossref](#)

60. Hi observations of the nearest starburst galaxy NGC 253 with the SKA precursor KAT-7

D. M. Lucero *et al.* 2015 *Monthly Notices of the Royal Astronomical*

[Crossref](#)

61. ALMA observations of 99 GHz free-free and H40 line emission from star formation in the centre of NGC 253
G. J. Bendo *et al* 2015 *Monthly Notices of the Royal Astronomical Society: Letters* **450** L80
[Crossref](#)
62. Optical-near-IR analysis of globular clusters in the IKN dwarf spheroidal: a complex star formation history
A. Tudorica *et al* 2015 *Astronomy & Astrophysics* **581** A84
[Crossref](#)
63. Diversity in extinction laws of Type Ia supernovae measured between 0.2 and 2 μm
R. Amanullah *et al* 2015 *Monthly Notices of the Royal Astronomical Society* **453** 3300
[Crossref](#)
64. Modeling the physical properties in the ISM of the low-metallicity galaxy NGC 4214
A. Dimaratos *et al* 2015 *Astronomy & Astrophysics* **580** A135
[Crossref](#)
65. The initial mass function and star formation law in the outer disc of NGC 2915
S. M. Bruzese *et al* 2015 *Monthly Notices of the Royal Astronomical Society* **447** 618
[Crossref](#)
66. Antlia B: A Faint Dwarf Galaxy Member of the NGC 3109 Association
D. J. Sand *et al.* 2015 *The Astrophysical Journal Letters* **812** L13
[IOPscience](#)
67. Physical Dust Models for the Extinction toward Supernova 2014J in M82
Jian Gao *et al.* 2015 *The Astrophysical Journal Letters* **807** L26
[IOPscience](#)

68. The Chandra Local Volume Survey. I. The X-Ray Point Source Populations of NGC 55, NGC 2403, and NGC 4214
B. Binder *et al.* 2015 *The Astronomical Journal* **150** 94
[IOPscience](#)
69. Stellar Populations and the Star Formation Histories of LSB Galaxies. V. WFC3 Color–Magnitude Diagrams
James Schombert and Stacy McGaugh 2015 *The Astronomical Journal* **150** 72
[IOPscience](#)
70. High-resolution Observations of Molecular Gas in the Early-type Dwarf Galaxy NGC 404
Christopher L. Taylor *et al.* 2015 *The Astronomical Journal* **149** 187
[IOPscience](#)
71. Legacy Extragalactic UV Survey (LEGUS) With the Hubble Space Telescope. I. Survey Description
D. Calzetti *et al.* 2015 *The Astronomical Journal* **149** 51
[IOPscience](#)
72. CARMA CO Observations of Three Extremely Metal-poor, Star-forming Galaxies
Steven R. Warren *et al.* 2015 *The Astrophysical Journal* **814** 30
[IOPscience](#)
73. A New Sample of Obscured AGNs Selected from the XMM-Newton and AKARI Surveys
Yuichi Terashima *et al.* 2015 *The Astrophysical Journal* **814** 11
[IOPscience](#)
74. Leo P: An Unquenched Very Low-mass Galaxy
Kristen B. W. McQuinn *et al.* 2015 *The Astrophysical Journal* **812** 158
[IOPscience](#)
75. When do stars in 47 Tucanae lose their mass?
Jeremy Heyl *et al.* 2015 *The Astrophysical Journal* **810** 127
[IOPscience](#)

76. Testing Density Wave Theory with Resolved Stellar Populations around Spiral Arms in M81
Yumi Choi *et al.* 2015 *The Astrophysical Journal* **810** 9
[IOPscience](#)
77. The Energetics of Cusp Destruction
Aaron J. Maxwell *et al.* 2015 *The Astrophysical Journal* **806** 229
[IOPscience](#)
78. Circumstellar Dust around AGB Stars and Implications for Infrared Emission from Galaxies
Alexa Villaume *et al.* 2015 *The Astrophysical Journal* **806** 82
[IOPscience](#)
79. Red Supergiants as Cosmic Abundance Probes: The Sculptor Galaxy NGC 300
J. Zachary Gazak *et al.* 2015 *The Astrophysical Journal* **805** 182
[IOPscience](#)
80. TiNy Titans: The Role of Dwarf–Dwarf Interactions in Low-mass Galaxy Evolution
S. Stierwalt *et al.* 2015 *The Astrophysical Journal* **805** 2
[IOPscience](#)
81. Observations of Type Ia Supernova 2014J with FLITECAM/SOFIA
William D. Vacca *et al.* 2015 *The Astrophysical Journal* **804** 66
[IOPscience](#)
82. Characterizing the Star Formation of the Low-mass Shield Galaxies from Hubble Space Telescope Imaging
Kristen. B. W. McQuinn *et al.* 2015 *The Astrophysical Journal* **802** 66
[IOPscience](#)
83. Diffuse Atomic and Molecular Gas in the Interstellar Medium of M82 toward SN 2014J
Adam M. Ritchey *et al.* 2015 *The Astrophysical Journal* **799** 197
[IOPscience](#)
84. Finding Car Analogs in Nearby Galaxies Using Spitzer. II. Identification of An

[IOPscience](#)

85. The Influence of Red Spiral Galaxies on the Shape of the Local K-band Luminosity Function

Nicolas J. Bonne *et al.* 2015 *The Astrophysical Journal* **799** 160

[IOPscience](#)

86. Constraints on the Origin of the First Light from SN 2014J

A. Goobar *et al.* 2015 *The Astrophysical Journal* **799** 106

[IOPscience](#)

87. Observations of the M82 SN 2014J with the Kilodegree Extremely Little Telescope

Robert J. Siverd *et al.* 2015 *The Astrophysical Journal* **799** 105

[IOPscience](#)

88. Early Observations and Analysis of the Type Ia SN 2014J in M82

G. H. Marion *et al.* 2015 *The Astrophysical Journal* **798** 39

[IOPscience](#)

89. New PARSEC evolutionary tracks of massive stars at low metallicity: testing canonical stellar evolution in nearby star-forming dwarf galaxies

Jing Tang *et al.* 2014 *Monthly Notices of the Royal Astronomical Society* **445** 4287

[Crossref](#)

90. Extensive HST ultraviolet spectra and multiwavelength observations of SN 2014J in M82 indicate reddening and circumstellar scattering by typical dust

Ryan J. Foley *et al.* 2014 *Monthly Notices of the Royal Astronomical Society* **443** 2887

[Crossref](#)

91. Structure of the Canes Venatici I cloud of galaxies

Dmitry I. Makarov *et al.* 2014 *Proceedings of the International Astronomical Union* **11** 209

[Crossref](#)

92. The triggering of starbursts in low-mass galaxies
Federico Lelli *et al* 2014 *Monthly Notices of the Royal Astronomical Society* **445** 1694
[Crossref](#)
93. The SAMI Galaxy Survey: the discovery of a luminous, low-metallicity H ii complex in the dwarf galaxy GAMA J141103.98–003242.3
S. N. Richards *et al* 2014 *Monthly Notices of the Royal Astronomical Society* **445** 1104
[Crossref](#)
94. Spitzer Local Volume Legacy (LVL) SEDs and physical properties
D. O. Cook *et al* 2014 *Monthly Notices of the Royal Astronomical Society* **445** 899
[Crossref](#)
95. Empirical ugri-UBVRc transformations for galaxies
D. O. Cook *et al* 2014 *Monthly Notices of the Royal Astronomical Society* **445** 890
[Crossref](#)
96. The Spitzer Local Volume Legacy (LVL) global optical photometry
D. O. Cook *et al* 2014 *Monthly Notices of the Royal Astronomical Society* **445** 881
[Crossref](#)
97. Optical and infrared emission of H ii complexes as a clue to the PAH life cycle
M. S. Khramtsova *et al* 2014 *Monthly Notices of the Royal Astronomical Society* **444** 757
[Crossref](#)
98. Upper limits on the luminosity of the progenitor of Type Ia supernova SN 2014J
M. T. B. Nielsen *et al* 2014 *Monthly Notices of the Royal Astronomical Society* **442** 3400
[Crossref](#)
99. Near-infrared counterparts of ultraluminous X-ray sources

M. Heida *et al* 2014 *Monthly Notices of the Royal Astronomical Society* **442** 1054

[Crossref](#)

100. Perseus I and the NGC 3109 association in the context of the Local Group dwarf galaxy structures
M. S. Pawlowski and S. S. McGaugh 2014 *Monthly Notices of the Royal Astronomical Society*
[Crossref](#)
101. A panchromatic analysis of starburst galaxy M82: probing the dust properties
S. Hutton *et al* 2014 *Monthly Notices of the Royal Astronomical Society*
[Crossref](#)
102. On the relation between metallicity and RGB color in HST/ACS data
D. Streich *et al* 2014 *Astronomy & Astrophysics* **563** A5
[Crossref](#)
103. A panoramic VISTA of the stellar halo of NGC 253
L. Greggio *et al* 2014 *Astronomy & Astrophysics* **562** A73
[Crossref](#)
104. Globular clusters and supermassive black holes in galaxies: further analysis and a larger sample
Gretchen L. H. Harris *et al* 2014 *Monthly Notices of the Royal Astronomical Society* **438** 2117
[Crossref](#)
105. Resolved photometry of young massive clusters in the starburst galaxy NGC 4214
A. Sollima *et al* 2014 *Monthly Notices of the Royal Astronomical Society* **437** 1918
[Crossref](#)
106. Discovery of a New Faint Dwarf Galaxy Associated with NGC 253
D. J. Sand *et al.* 2014 *The Astrophysical Journal Letters* **793** L7
[IOPscience](#)
107. Detection of 36 GHz Class I Methanol Maser Emission toward NGC 253

[IOPscience](#)

108. Reversal of Fortune: Increased Star Formation Efficiencies in the Early Histories of Dwarf Galaxies?

Piero Madau *et al.* 2014 *The Astrophysical Journal Letters* **790** L17

[IOPscience](#)

109. The Peculiar Extinction Law of SN 2014J Measured with the Hubble Space Telescope

R. Amanullah *et al.* 2014 *The Astrophysical Journal Letters* **788** L21

[IOPscience](#)

110. The Rise of SN 2014J in the Nearby Galaxy M82

A. Goobar *et al.* 2014 *The Astrophysical Journal Letters* **784** L12

[IOPscience](#)

111. The Green Bank Telescope Maps the Dense, Star-forming Gas in the Nearby Starburst Galaxy M82

Amanda A. Kepley *et al.* 2014 *The Astrophysical Journal Letters* **780** L13

[IOPscience](#)

112. The Abundance Properties of Nearby Late-type Galaxies. I. The Data

L. S. Pilyugin *et al.* 2014 *The Astronomical Journal* **147** 131

[IOPscience](#)

113. Multi-epoch Very Long Baseline Interferometric Observations of the Nuclear Starburst Region of NGC 253: Improved Modeling of the Supernova and Star formation Rates

H. Rampadarath *et al.* 2014 *The Astronomical Journal* **147** 5

[IOPscience](#)

114. The Panchromatic Hubble Andromeda Treasury. X. Ultraviolet to Infrared Photometry of 117 Million Equidistant Stars

Benjamin F. Williams *et al.* 2014 *The Astrophysical Journal Supplement Series* **215** 9

[IOPscience](#)

115. A Deep Chandra ACIS Survey of M83

[IOPscience](#)

116. Extended HCN and HCO⁺ Emission in the Starburst Galaxy M82
P. Salas *et al.* 2014 *The Astrophysical Journal* **797** 134
[IOPscience](#)
117. Fluctuation Spectroscopy: A New Probe of Old Stellar Populations
Pieter G. van Dokkum and Charlie Conroy 2014 *The Astrophysical Journal* **797** 56
[IOPscience](#)
118. The Supernova Progenitor Mass Distributions of M31 and M33: Further Evidence for an Upper Mass Limit
Zachary G. Jennings *et al.* 2014 *The Astrophysical Journal* **795** 170
[IOPscience](#)
119. Investigating Nearby Star-forming Galaxies in the Ultraviolet with HST/COS Spectroscopy. I. Spectral Analysis and Interstellar Abundance Determinations
B. L. James *et al.* 2014 *The Astrophysical Journal* **795** 109
[IOPscience](#)
120. The Tip of the Red Giant Branch Distance to the Perfect Spiral Galaxy M74 Hosting Three Core-collapse Supernovae
In Sung Jang and Myung Gyoon Lee 2014 *The Astrophysical Journal* **792** 52
[IOPscience](#)
121. Constraints for the Progenitor Masses of 17 Historic Core-collapse Supernovae
Benjamin F. Williams *et al.* 2014 *The Astrophysical Journal* **791** 105
[IOPscience](#)
122. No X-Rays from the Very Nearby Type Ia SN 2014J: Constraints on Its Environment
R. Margutti *et al.* 2014 *The Astrophysical Journal* **790** 52
[IOPscience](#)
123. Evolution of Thermally Pulsing Asymptotic Giant Branch Stars. IV. Constraining

124. The Star Formation Histories of Local Group Dwarf Galaxies. II. Searching For Signatures of Reionization

Daniel R. Weisz *et al.* 2014 *The Astrophysical Journal***789** 148

125. The Star Formation Histories of Local Group Dwarf Galaxies. I. Hubble Space Telescope/Wide Field Planetary Camera 2 Observations

Daniel R. Weisz *et al.* 2014 *The Astrophysical Journal***789** 147

126. Stellar Metallicity of the Extended Disk and Distance of the Spiral Galaxy NGC 3621

Rolf-Peter Kudritzki *et al.* 2014 *The Astrophysical Journal***788** 56

127. Spectral Line Survey toward the Spiral Arm of M51 in the 3 and 2 mm Bands
Yoshimasa Watanabe *et al.* 2014 *The Astrophysical Journal***788** 4

128. The Core Mass Growth and Stellar Lifetime of Thermally Pulsing Asymptotic Giant Branch Stars

Jason S. Kalirai *et al.* 2014 *The Astrophysical Journal***782** 17

129. GHOSTS I: A New Faint Very Isolated Dwarf Galaxy at $D = 12 \pm 2$ Mpc
Antonela Monachesi *et al.* 2014 *The Astrophysical Journal***780** 179

130. The Large-scale Structure of the Halo of the Andromeda Galaxy. I. Global Stellar Density, Morphology and Metallicity Properties

Rodrigo A. Ibata *et al.* 2014 *The Astrophysical Journal***780** 128

131. Nebular Metallicities in Two Isolated Local Void Dwarf Galaxies

David C. Nicholls *et al.* 2014 *The Astrophysical Journal***780** 88

132. TeV observations of the Galactic center and starburst galaxies
Mathieu de Naurois 2013 *Proceedings of the International Astronomical Union* **9** 29
[Crossref](#)
133. An X-Ray Study of the Galactic-Scale Starburst-Driven Outflow in NGC 253
I. Mitsuishi *et al* 2013 *Publications of the Astronomical Society of Japan* **65** 44
[Crossref](#)
134. Dwarfs walking in a row
M. Bellazzini *et al* 2013 *Astronomy & Astrophysics* **559** L11
[Crossref](#)
135. The formation of Local Group planes of galaxies
E. J. Shaya and R. B. Tully 2013 *Monthly Notices of the Royal Astronomical Society*
[Crossref](#)
136. Quantified H I morphology - VII. Star formation and tidal influence on local dwarf H I morphology
B. W. Holwerda *et al* 2013 *Monthly Notices of the Royal Astronomical Society*
[Crossref](#)
137. The ultraluminous state revisited: fractional variability and spectral shape as diagnostics of super-Eddington accretion
A. D. Sutton *et al* 2013 *Monthly Notices of the Royal Astronomical Society*
[Crossref](#)
138. Modeling the Panchromatic Spectral Energy Distributions of Galaxies
Charlie Conroy 2013 *Annual Review of Astronomy and Astrophysics* **51** 393
[Crossref](#)
139. Mergers of multimetallic globular clusters: the role of dynamics
P. Amaro-Seoane *et al* 2013 *Monthly Notices of the Royal Astronomical Society*

[Crossref](#)

140. Observing extended sources with the Herschel SPIRE Fourier Transform Spectrometer

R. Wu *et al* 2013 *Astronomy & Astrophysics* **556** A116

[Crossref](#)

141. Suppression of star formation in the galaxy NGC 253 by a starburst-driven molecular wind

Alberto D. Bolatto *et al* 2013 *Nature* **499** 450

[Crossref](#)

142. VLT/VIMOS observations of an occulting galaxy pair: redshifts and effective extinction curve

B. W. Holwerda *et al* 2013 *Monthly Notices of the Royal Astronomical Society*

[Crossref](#)

143. Infrared photometry of young massive clusters in the starburst galaxy NGC 4214

A. Sollima *et al* 2013 *Monthly Notices of the Royal Astronomical Society*

[Crossref](#)

144. Radio-continuum study of the nearby Sculptor group Galaxies. Part 2: NGC 55 at $\lambda = 20, 13, 6$ and 3 cm

Andrew N. O'Brien *et al* 2013 *Astrophysics and Space Science*

[Crossref](#)

145. Distances to dwarf galaxies of the Canes Venatici I cloud

D. I. Makarov *et al* 2013 *Astrophysical Bulletin* **68** 125

[Crossref](#)

146. Disc stability and neutral hydrogen as a tracer of dark matter

G. R. Meurer *et al* 2013 *Monthly Notices of the Royal Astronomical Society*

[Crossref](#)

147. The star formation history of the Sculptor dwarf irregular galaxy

S. Lianou and A. A. Cole 2013 *Astronomy & Astrophysics* **549** A47

[Crossref](#)

148. Clues on the Rejuvenation of the S0 Galaxy NGC 404 from the Chemical Abundance of Its Outer Disk
Fabio Bresolin 2013 *The Astrophysical Journal Letters* **772** L23
[IOPscience](#)
149. ALFALFA Discovery of the Nearby Gas-rich Dwarf Galaxy Leo P. IV. Distance Measurement from LBT Optical Imaging
Kristen B. W. McQuinn *et al.* 2013 *The Astronomical Journal* **146** 145
[IOPscience](#)
150. Confirmation of Faint Dwarf Galaxies in the M81 Group
Kristin Chiboucas *et al.* 2013 *The Astronomical Journal* **146** 126
[IOPscience](#)
151. Surface Brightness Profiles of Dwarf Galaxies. I. Profiles and Statistics
Kimberly A. Herrmann *et al.* 2013 *The Astronomical Journal* **146** 104
[IOPscience](#)
152. Cosmicflows-2: The Data
R. Brent Tully *et al.* 2013 *The Astronomical Journal* **146** 86
[IOPscience](#)
153. The Snapshot Hubble U-band Cluster Survey (SHUCS). I. Survey Description and First Application to the Mixed Star Cluster Population of NGC 4041
I. S. Konstantopoulos *et al.* 2013 *The Astronomical Journal* **145** 137
[IOPscience](#)
154. Updated Nearby Galaxy Catalog
Igor D. Karachentsev *et al.* 2013 *The Astronomical Journal* **145** 101
[IOPscience](#)
155. Astrophysical tests of modified gravity: the morphology and kinematics of dwarf galaxies
Vinu Vikram *et al.* 2013 *Journal of Cosmology and Astroparticle Physics* **2013** 020
[IOPscience](#)
156. Modeling X-Ray Binary Evolution in Normal Galaxies: Insights from SINGS
P. Tzanavaris *et al.* 2013 *The Astrophysical Journal* **774** 136

[IOPscience](#)

157. Dusty Winds: Extraplanar Polycyclic Aromatic Hydrocarbon Features of Nearby Galaxies

Alexander McCormick *et al.* 2013 *The Astrophysical Journal* **774** 126

[IOPscience](#)

158. Drivers of H I Turbulence in Dwarf Galaxies

Adrienne M. Stilp *et al.* 2013 *The Astrophysical Journal* **773** 88

[IOPscience](#)

159. The Nature of the Second Parameter in the IRX- Relation for Local Galaxies

Kathryn Grasha *et al.* 2013 *The Astrophysical Journal* **773** 174

[IOPscience](#)

160. Timescales on which Star Formation Affects the Neutral Interstellar Medium

Adrienne M. Stilp *et al.* 2013 *The Astrophysical Journal* **772** 124

[IOPscience](#)

161. Measuring Galaxy Star Formation Rates from Integrated Photometry: Insights from Color-Magnitude Diagrams of Resolved Stars

Benjamin D. Johnson *et al.* 2013 *The Astrophysical Journal* **772** 8

[IOPscience](#)

162. The Ages of High-mass X-Ray Binaries in NGC 2403 and NGC 300

Benjamin F. Williams *et al.* 2013 *The Astrophysical Journal* **772** 12

[IOPscience](#)

163. Testing Galaxy Formation Models with the GHOSTS Survey: The Color Profile of M81's Stellar Halo

Antonela Monachesi *et al.* 2013 *The Astrophysical Journal* **766** 106

[IOPscience](#)

164. Global H I Kinematics in Dwarf Galaxies

Adrienne M. Stilp *et al.* 2013 *The Astrophysical Journal* **765** 136

[IOPscience](#)

165. The ACS Nearby Galaxy Survey Treasury. XI. The Remarkably Undisturbed NGC 2403 Disk

[IOPscience](#)

166. The Unusually Luminous Extragalactic Nova SN 2010U
Ian Czekala *et al.* 2013 *The Astrophysical Journal* **765** 57
[IOPscience](#)
167. The Chandra Local Volume Survey: The X-Ray Point-source Population of NGC 404
B. Binder *et al.* 2013 *The Astrophysical Journal* **763** 128
[IOPscience](#)
168. The Extended Optical Disk of M101
J. Christopher Mihos *et al.* 2013 *The Astrophysical Journal* **762** 82
[IOPscience](#)
169. The Panchromatic Hubble Andromeda Treasury. IV. A Probabilistic Approach to Inferring the High-mass Stellar Initial Mass Function and Other Power-law Functions
Daniel R. Weisz *et al.* 2013 *The Astrophysical Journal* **762** 123
[IOPscience](#)
170. A deep, wide-field study of Holmberg II with Suprime-Cam: evidence for ram pressure stripping
Edouard J. Bernard *et al.* 2012 *Monthly Notices of the Royal Astronomical Society* **426** 3490
[Crossref](#)
171. The satellites of the Milky Way - insights from semi-analytic modelling in a CDM cosmology
E. Starkeburg *et al.* 2012 *Monthly Notices of the Royal Astronomical Society*
[Crossref](#)
172. The transmutation of dwarf galaxies: stellar populations
M. Koleva *et al.* 2012 *Monthly Notices of the Royal Astronomical Society*
[Crossref](#)
173. Chandra survey of nearby highly inclined disc galaxies - I. X-ray measurements of galactic coronae

J.-T. Li and Q. D. Wang 2012 *Monthly Notices of the Royal Astronomical Society*

[Crossref](#)

174. On the association between core-collapse supernovae and H II regions
P. A. Crowther 2012 *Monthly Notices of the Royal Astronomical Society*

[Crossref](#)

175. Identifying Local Group field galaxies that have interacted with the Milky Way
Maureen Teyssier *et al* 2012 *Monthly Notices of the Royal Astronomical Society* **426** 1808

[Crossref](#)

176. Star Formation in the Milky Way and Nearby Galaxies

Robert C. Kennicutt and Neal J. Evans 2012 *Annual Review of Astronomy and Astrophysics* **50** 531

[Crossref](#)

177. A unique isolated dwarf spheroidal galaxy at $D = 1.9$ Mpc

Dmitry Makarov *et al* 2012 *Monthly Notices of the Royal Astronomical Society* n/a

[Crossref](#)

178. Star formation history and the SED of galaxies: insights from resolved stars

Benjamin D. Johnson and Daniel R. Weisz 2012 *Proceedings of the International Astronomical Union* **7** 59

[Crossref](#)

179. Dynamics of starbursting dwarf galaxies. II. UGC 4483

F. Lelli *et al* 2012 *Astronomy & Astrophysics* **544** A145

[Crossref](#)

180. The JCMT Nearby Galaxies Legacy Survey - VIII. CO data and the LCO(3-2)-LFIR correlation in the SINGS sample

C. D. Wilson *et al* 2012 *Monthly Notices of the Royal Astronomical Society* **424** 3050

[Crossref](#)

181. A close look at the Centaurus A group of galaxies : IV. Recent star formation

histories of late-type dwarfs around CenA

D. Crnojevi *et al* 2012 *Astronomy and Astrophysics* **541** A131

[Crossref](#)

182. The JCMT Nearby Galaxies Legacy Survey - VII. H imaging and massive star formation properties : The JCMT Nearby Galaxies Legacy Survey - VII.

J. R. Sánchez-Gallego *et al* 2012 *Monthly Notices of the Royal Astronomical Society* no

[Crossref](#)

183. The Planetary Nebula Luminosity Function at the dawn of Gaia

Robin Ciardullo 2012 *Astrophysics and Space Science*

[Crossref](#)

184. Fundamentals of the dwarf fundamental plane

M. L. McCall *et al* 2012 *Astronomy and Astrophysics* **540** A49

[Crossref](#)

185. Cuspy no more: how outflows affect the central dark matter and baryon distribution in cold dark matter galaxies : Galaxy cores in CDM

F. Governato *et al* 2012 *Monthly Notices of the Royal Astronomical Society* no

[Crossref](#)

186. Distances to galaxies from the brightest stars in the Universe

Rolf-Peter Kudritzki and Miguel A. Urbaneja 2012 *Astrophysics and Space Science*

[Crossref](#)

187. The star formation history and dust content in the far outer disc of M31 : The far outer disc of M31

Edouard J. Bernard *et al* 2012 *Monthly Notices of the Royal Astronomical Society* no

[Crossref](#)

188. A solution to the problems of cusps and rotation curves in dark matter halos in the cosmological standard model

A.G. Doroshkevich *et al* 2012 *Uspekhi Fizicheskikh Nauk* **182** 3

[Crossref](#)

189. Tidal Interactions at the Edge of the Local Group: New Evidence for Tidal Features in the Antlia Dwarf Galaxy
Samantha J. Penny *et al.* 2012 *The Astrophysical Journal Letters* **758** L32
[IOPscience](#)
190. Mid-IR FORCAST/SOFIA Observations of M82
T. Nikola *et al.* 2012 *The Astrophysical Journal Letters* **749** L19
[IOPscience](#)
191. Hunting for Young Dispersing Star Clusters in IC 2574
Anne Pellerin *et al.* 2012 *The Astronomical Journal* **144** 182
[IOPscience](#)
192. LITTLE THINGS
Deidre A. Hunter *et al.* 2012 *The Astronomical Journal* **144** 134
[IOPscience](#)
193. VLA-ANGST: A High-resolution HI Survey of Nearby Dwarf Galaxies
Jürgen Ott *et al.* 2012 *The Astronomical Journal* **144** 123
[IOPscience](#)
194. The Observed Properties of Dwarf Galaxies in and around the Local Group
Alan W. McConnachie 2012 *The Astronomical Journal* **144** 4
[IOPscience](#)
195. Converting from 3.6 and 4.5 μm Fluxes to Stellar Mass
Michael Eskew *et al.* 2012 *The Astronomical Journal* **143** 139
[IOPscience](#)
196. A solution to the problems of cusps and rotation curves in dark matter halos in the cosmological standard model
Andrei G Doroshkevich *et al.* 2012 *Physics-Uspekhi* **55** 3
[IOPscience](#)
197. The Panchromatic Hubble Andromeda Treasury
Julianne J. Dalcanton *et al.* 2012 *The Astrophysical Journal Supplement Series* **200** 18
[IOPscience](#)

198. Resolved Near-infrared Stellar Populations in Nearby Galaxies
Julianne J. Dalcanton *et al.* 2012 *The Astrophysical Journal Supplement Series* **198** 6
[IOPscience](#)
199. Supernova Remnant Progenitor Masses in M31
Zachary G. Jennings *et al.* 2012 *The Astrophysical Journal* **761** 26
[IOPscience](#)
200. The Chandra Local Volume Survey: The X-Ray Point-source Catalog of NGC 300
B. Binder *et al.* 2012 *The Astrophysical Journal* **758** 15
[IOPscience](#)
201. Spectral Analysis and Interpretation of the γ -Ray Emission from the Starburst Galaxy NGC 253
A. Abramowski *et al.* 2012 *The Astrophysical Journal* **757** 158
[IOPscience](#)
202. Tracing Cold HI Gas in nearby, Low-mass Galaxies
Steven R. Warren *et al.* 2012 *The Astrophysical Journal* **757** 84
[IOPscience](#)
203. Direct Oxygen Abundances for Low-luminosity LVL Galaxies
Danielle A. Berg *et al.* 2012 *The Astrophysical Journal* **754** 98
[IOPscience](#)
204. The Intermediate-mass Black Hole Candidate in the Center of NGC 404: New Evidence from Radio Continuum Observations
Kristina Nyland *et al.* 2012 *The Astrophysical Journal* **753** 103
[IOPscience](#)
205. Herschel-SPIRE Imaging Spectroscopy of Molecular Gas in M82
J. Kamenetzky *et al.* 2012 *The Astrophysical Journal* **753** 70
[IOPscience](#)
206. The Resolved Stellar Population in 50 Regions of M83 from HST/WFC3 Early Release Science Observations
Hwihyun Kim *et al.* 2012 *The Astrophysical Journal* **753** 26

207. The ACS Nearby Galaxy Survey Treasury. X. Quantifying the Star Cluster Formation Efficiency of nearby Dwarf Galaxies

David O. Cook *et al.* 2012 *The Astrophysical Journal* **751** 100

208. The Star Formation History of Leo T from Hubble Space Telescope Imaging

Daniel R. Weisz *et al.* 2012 *The Astrophysical Journal* **748** 88

209. The Contribution of TP-AGB and RHeB Stars to the Near-IR Luminosity of Local Galaxies: Implications for Stellar Mass Measurements of High-redshift Galaxies

J. Melbourne *et al.* 2012 *The Astrophysical Journal* **748** 47

210. Quantitative Spectroscopy of Blue Supergiant Stars in the Disk of M81: Metallicity, Metallicity Gradient, and Distance

Rolf-Peter Kudritzki *et al.* 2012 *The Astrophysical Journal* **747** 15

211. On the Last 10 Billion Years of Stellar Mass Growth in Star-forming Galaxies

Samuel N. Leitner 2012 *The Astrophysical Journal* **745** 149

212. SLUG—Stochastically Lighting Up Galaxies. I. Methods and Validating Tests

Robert L. da Silva *et al.* 2012 *The Astrophysical Journal* **745** 145

213. The Central Dark Matter Distribution of NGC 2976

Joshua J. Adams *et al.* 2012 *The Astrophysical Journal* **745** 92

214. Modeling the Effects of Star Formation Histories on H and Ultraviolet Fluxes in nearby Dwarf Galaxies

Daniel R. Weisz *et al.* 2012 *The Astrophysical Journal* **744** 44

215. The evolution of stellar structures in dwarf galaxies : The evolution of stellar structures
N. Bastian *et al* 2011 *Monthly Notices of the Royal Astronomical Society* no [Crossref](#)
216. Stellar metallicities beyond the Local Group: the potential of J-band spectroscopy with extremely large telescopes
C. J. Evans *et al* 2011 *Astronomy & Astrophysics* **527** A50
[Crossref](#)
217. Diffraction-Limited Subaru Imaging of M 82: Sharp Mid-Infrared View of the Starburst Core*
P. Gandhi *et al* 2011 *Publications of the Astronomical Society of Japan* **63** S505
[Crossref](#)
218. Quantifying the faint structure of galaxies: the late-type spiral NGC 2403 † : The Faint Structure of NGC 2403
Michael K. Barker *et al* 2011 *Monthly Notices of the Royal Astronomical Society* no [Crossref](#)
219. Stars and clusters of the coma galaxies NGC 4921 and NGC 4923
N. A. Tikhonov and O. A. Galazutdinova 2011 *Astronomy Letters* **37** 766
[Crossref](#)
220. Antlia Dwarf Galaxy: distance, quantitative morphology and recent formation history via statistical field correction : Antlia Dwarf Galaxy
Kevin A. Pimbblet and Warrick J. Couch 2011 *Monthly Notices of the Royal Astronomical Society* no [Crossref](#)
221. Satellites in the Local Group and Other Nearby Groups
E.K. Grebel 2011 *EAS Publications Series* **48** 315
[Crossref](#)
222. New period-luminosity and period-color relations of classical Cepheids : IV. The low-metallicity galaxies IC 1613, WLM, Pegasus, Sextans A and B, and

Leo A in comparison to SMC

G. A. Tammann *et al* 2011 *Astronomy and Astrophysics* **531** A134

[Crossref](#)

223. Emission sparks around M 81 and in some dwarf spheroidal galaxies † :

Emission sparks in dSph galaxies

Igor Karachentsev *et al* 2011 *Monthly Notices of the Royal Astronomical Society Letters* no

[Crossref](#)

224. Fe K Line Complex in the Nuclear Region of NGC 253

Ikuyuki Mitsuishi *et al.* 2011 *The Astrophysical Journal Letters* **742** L31

[IOPscience](#)

225. The Progenitor Mass of SN 2011dh from Stellar Population Analysis

Jeremiah W. Murphy *et al.* 2011 *The Astrophysical Journal Letters* **742** L4

[IOPscience](#)

226. Chandra Detection of SN 2010da Four Months After Outburst: Evidence for a High-mass X-Ray Binary in NGC 300

B. Binder *et al.* 2011 *The Astrophysical Journal Letters* **739** L51

[IOPscience](#)

227. Unveiling Extragalactic Star Formation Using Radio Recombination Lines: An Expanded Very Large Array Pilot Study with NGC 253

Amanda A. Kepley *et al.* 2011 *The Astrophysical Journal Letters* **739** L24

[IOPscience](#)

228. The History of Star Formation in Galaxy Disks in the Local Volume as Measured by the Advanced Camera for Surveys Nearby Galaxy Survey

Treasury

Benjamin F. Williams *et al.* 2011 *The Astrophysical Journal Letters* **734** L22

[IOPscience](#)

229. Nearby Galaxies in More Distant Contexts

Michael Eskew and Dennis Zaritsky 2011 *The Astronomical Journal* **141** 69

[IOPscience](#)

230. KINGFISH—Key Insights on Nearby Galaxies: A Far-Infrared Survey with

231. Resolved young stellar populations in star-forming regions of the Magellanic Clouds

Dimitrios A Gouliermis 2011 *Physica Scripta* **84** 048401

232. The GHOSTS Survey. I. Hubble Space Telescope Advanced Camera for Surveys Data

D. J. Radburn-Smith *et al.* 2011 *The Astrophysical Journal Supplement Series* **195** 18

233. A GALEX Ultraviolet Imaging Survey of Galaxies in the Local Volume

Janice C. Lee *et al.* 2011 *The Astrophysical Journal Supplement Series* **192** 6

234. A Study of Cepheids in M81 with the Large Binocular Telescope (Efficiently Calibrated with Hubble Space Telescope)

J. R. Gerke *et al.* 2011 *The Astrophysical Journal* **743** 176

235. How Typical Are the Local Group Dwarf Galaxies?

Daniel R. Weisz *et al.* 2011 *The Astrophysical Journal* **743** 8

236. A Deep Chandra Observation of the Wolf-Rayet + Black Hole Binary NGC 300 X-1

B. Binder *et al.* 2011 *The Astrophysical Journal* **742** 128

237. The ACS Nearby Galaxy Survey Treasury. VIII. The Global Star Formation Histories of 60 Dwarf Galaxies in the Local Volume

Daniel R. Weisz *et al.* 2011 *The Astrophysical Journal* **739** 5

238. The Formation of Kiloparsec-scale H I Holes in Dwarf Galaxies
Steven R. Warren *et al.* 2011 *The Astrophysical Journal* **738** 10
[IOPscience](#)
239. The Magnetic Field of the Irregular Galaxy NGC 4214
Amanda A. Kepley *et al.* 2011 *The Astrophysical Journal* **736** 139
[IOPscience](#)
240. The ACS Nearby Galaxy Survey Treasury. VII. The NGC 4214 Starburst and the Effects of Star Formation History on Dwarf Morphology
Benjamin F. Williams *et al.* 2011 *The Astrophysical Journal* **735** 22
[IOPscience](#)
241. The Extragalactic Distance Scale without Cepheids. IV.
Lachlan Hislop *et al.* 2011 *The Astrophysical Journal* **733** 75
[IOPscience](#)
242. Multi-element Abundance Measurements from Medium-resolution Spectra. IV. Alpha Element Distributions in Milky Way Satellite Galaxies
Evan N. Kirby *et al.* 2011 *The Astrophysical Journal* **727** 79
[IOPscience](#)
243. Fitting the integrated spectral energy distributions of galaxies
Jakob Walcher *et al* 2010 *Astrophysics and Space Science*
[Crossref](#)
244. A close look at the Centaurus A group of galaxies : I. Metallicity distribution functions and population gradients in early-type dwarfs
D. Crnojevi *et al* 2010 *Astronomy and Astrophysics* **516** A85
[Crossref](#)
245. A bright off-nuclear X-ray source: a type IIIn supernova, a bright ULX or a recoiling supermassive black hole in CXO J122518.6+144545 : A bright off-nuclear X-ray source
P. G. Jonker *et al* 2010 *Monthly Notices of the Royal Astronomical Society* no
[Crossref](#)

246. Star formation history of KDG 61 and KDG 64 from spectroscopy and colour-magnitude diagrams : KDG 61 & 64 star formation history
Lidia Makarova *et al* 2010 *Monthly Notices of the Royal Astronomical Society* no
[Crossref](#)
247. Stellar population and kinematics of NGC 404
A. Bouchard *et al* 2010 *Astronomy and Astrophysics* **513** A54
[Crossref](#)
248. Supernova remnants, planetary nebulae and the distance to NGC 4214
Michael A. Dopita *et al* 2010 *Astrophysics and Space Science*
[Crossref](#)
249. Booms and Busts: the Burstiness of Star Formation in Nearby Dwarf Galaxies
A. A. Cole 2010 *Publications of the Astronomical Society of Australia* **27** 234
[Crossref](#)
250. SN 2010U: A Luminous Nova in NGC 4214
Roberta M. Humphreys *et al.* 2010 *The Astrophysical Journal Letters* **718** L43
[IOPscience](#)
251. NGC 404: A Rejuvenated Lenticular Galaxy on a Merger-induced, Blueward Excursion Into the Green Valley
David A. Thilker *et al.* 2010 *The Astrophysical Journal Letters* **714** L171
[IOPscience](#)
252. Ancient Stars Beyond the Local Group: RR Lyrae Variables and Blue Horizontal Branch Stars in Sculptor Group Dwarf Galaxies
G. S. Da Costa *et al.* 2010 *The Astrophysical Journal Letters* **708** L121
[IOPscience](#)
253. The *Spitzer* Survey of Stellar Structure in Galaxies (**S⁴G**)
Kartik Sheth *et al.* 2010 *Publications of the Astronomical Society of the Pacific* **122** 1397
[IOPscience](#)

254. Shaken, Not Stirred: The Disrupted Disk of the Starburst Galaxy NGC 253
T. J. Davidge 2010 *The Astrophysical Journal***725** 1342
[IOPscience](#)
255. The ACS Nearby Galaxy Survey Treasury. IX. Constraining Asymptotic Giant Branch Evolution with Old Metal-poor Galaxies
Léo Girardi *et al.* 2010 *The Astrophysical Journal***724** 1030
[IOPscience](#)
256. Deep HST/ACS Photometry of the M81 Halo
Patrick R. Durrell *et al.* 2010 *The Astrophysical Journal***718** 1118
[IOPscience](#)
257. The Advanced Camera for Surveys Nearby Galaxy Survey Treasury. VI. The Ancient Star-forming Disk of NGC 404
Benjamin F. Williams *et al.* 2010 *The Astrophysical Journal***716** 71
[IOPscience](#)
258. An Aromatic Inventory of the Local Volume
A. R. Marble *et al.* 2010 *The Astrophysical Journal***715** 506
[IOPscience](#)
259. The Advanced Camera for Surveys Nearby Galaxy Survey Treasury. V. Radial Star Formation History of NGC 300
Stephanie M. Gogarten *et al.* 2010 *The Astrophysical Journal***712** 858
[IOPscience](#)
260. The Asymptotic Giant Branch and the Tip of the Red Giant Branch as Probes of Star Formation History: The Nearby Dwarf Irregular Galaxy KKH 98
J. Melbourne *et al.* 2010 *The Astrophysical Journal***712** 469
[IOPscience](#)
261. The Advanced Camera for Surveys Nearby Galaxy Survey Treasury. IV. The Star Formation History of NGC 2976
Benjamin F. Williams *et al.* 2010 *The Astrophysical Journal***709** 135
[IOPscience](#)
262. EAGLE Spectroscopy of Resolved Stellar Populations Beyond the Local Group
Chris Evans *et al.* 2009 *Proceedings of the International Astronomical*

[Crossref](#)

263. The Future of Stellar Populations Studies in the Milky Way and the Local Group
Steven R. Majewski 2009 *Proceedings of the International Astronomical Union* **5** 99

[Crossref](#)

264. Does Stellar Feedback Create HI Holes? A Hubble Space Telescope/Very Large Array Study of Holmberg II
Daniel R. Weisz *et al.* 2009 *The Astrophysical Journal* **704** 1538

[IOPscience](#)

265. The Spitzer Local Volume Legacy: Survey Description and Infrared Photometry
D. A. Dale *et al.* 2009 *The Astrophysical Journal* **703** 517

[IOPscience](#)

266. The NGC 300 Transient: An Alternative Method for Measuring Progenitor Masses
Stephanie M. Gogarten *et al.* 2009 *The Astrophysical Journal* **703** 300

[IOPscience](#)

Export citations:


[BibTeX](#)

[RIS](#)

© Copyright 2018 IOP Publishing

[Terms & conditions](#)

[Disclaimer](#)

[Privacy & cookie policy](#) 

This site uses cookies. By continuing to use this site you agree to our use of cookies.

The ACS nearby galaxy survey treasury, the pit creates a sharp phonon.
Telling sexual stories: Power, change and social worlds, typing is not trivial.
Clubbing: Dancing, ecstasy, vitality, the pickup speeds up the flow.
A measurement of the damping tail of the cosmic microwave background power spectrum with the South Pole Telescope, the dream, as required by the laws of thermodynamics, transforms an asteroid bauxite.
A Sunyaev-Zel'dovich-selected sample of the most massive galaxy clusters in the 2500 deg² South Pole telescope survey, in special rules on this issue, it is indicated that reality enlightens the sociometric portrait of the consumer.
Theories of the information society, the interaction between the Corporation and the client is nontrivial.
A CLEAR AGE-VELOCITY DISPERSION CORRELATION IN ANDROMEDA'S STELLAR DISK, the gyroscopic pendulum is public.
Dancing with Racial Feet: Bert Williams and the Performance of Blackness, creating a committed buyer is not critical.
Evaluative criteria for qualitative research in health care: controversies and recommendations, in other words, the ocean desert causes communism.